5-2018

Depth-Resolved Assessment of Atherosclerosis by Intravascular Photoacoustic-Ultrasound Imaging

Ayeeshik Kole
Purdue University

DEPTH-RESOLVED ASSESSMENT OF ATHEROSCLEROSIS BY INTRAVASCULAR PHOTOACOUSTIC-ULTRASOUND IMAGING

by

Ayeeshik Kole

A Dissertation

Submitted to the Faculty of Purdue University

In Partial Fulfillment of the Requirements for the degree of

Doctor of Philosophy

Weldon School of Biomedical Engineering

West Lafayette, Indiana

May 2018

THE PURDUE UNIVERSITY GRADUATE SCHOOL
STATEMENT OF COMMITTEE APPROVAL

Dr. Michael Sturek, Co-chair

Weldon School of Biomedical Engineering

Department of Cellular and Integrative Physiology,

Indiana University School of Medicine

Dr. Ji-Xin Cheng, Co-chair

Weldon School of Biomedical Engineering

Dr. Craig Goergen

Weldon School of Biomedical Engineering

Dr. Nan Kong

Weldon School of Biomedical Engineering

Dr. Islam Bolad

Krannert Institute of Cardiology, Indiana University School of Medicine

Approved by:

Dr. George R. Wodicka

Head of the Graduate Program

To my parents, brother, and Nisha

ACKNOWLEDGMENTS

The work presented in this dissertation is a reflection of the support and contributions of many, many people throughout this academic journey. I am truly grateful for this incredible scientific community. I would first like to acknowledge the guidance and support from my co-mentors, Dr. Michael Sturek and Dr. Ji-Xin Cheng. Thank you for forging this collaboration and providing me with the flexibility, autonomy, and resources to bridge the two labs and campuses. The success of this unique project is a testament to the team effort fostered by both labs. I would also like to thank both mentors for challenging me academically and scientifically. This has included encouragement to present at conferences, support to collaborate with leaders in the field, and the push to become well-versed in every aspect of the project and literature. I have no doubt that the skills and mentorship I have learned from you have prepared me for the next stages of my career.

Thank you to my committee members, Drs. Craig Goergen, Nan Kong, and Islam Bolad, who have also served as teachers, advisers, and collaborators along the way. Your guidance and feedback has helped shape the success and trajectory of this work. I would also like to thank my Sturek lab members, past and present: Mikaela, Becky, Stacey, Jill, Sarah, Mouhamad, Jim, and Jane. Your help in the form of teaching, tissue collection, analysis, editing, and scientific discussion has been pivotal. Moreover, the non-scientific conversations and company the past several years has made this lab my campus home. I was fortunate to have two labs and need to give equal thanks to my outstanding Cheng lab members: Yingchun, Jie, Jieying, Pu, Rui, and Brittani. Your collaboration has been essential to the advancements of this project and my education as an engineer. In addition, thank you to the Medical Scientist Training Program (MSTP) and administration. Sandy and Jan, thank you so much for never letting me feel lost during graduate school. Thank you to my fellow MSTP classmates, who have always been there to give me advice and lay down footsteps to follow.

Finally, I would like to thank my family and friends, who have been there to celebrate the successes and also provide support during the challenges. Mom, Dad, Abhi, and Nisha, thank you for having so much confidence in me, especially at the times I did not have it myself.

TABLE OF CONTENTS

LIST OF TABLES

LIST OF FIGURES

ABBREVIATIONS

ACS, Acute coronary syndrome

CAD, Coronary artery disease

CVD, Cardiovascular disease

H&E, Hematoxylin and eosin

HR, Hazard ratio

IVPA-US, Intravascular photoacoustic-ultrasound

IVUS, Intravascular ultrasound

LCBI, Lipid core burden index

LCP, Lipid core plaque

maxLCBI$_{4mm}$, Maximum lipid core burden within a 4 mm segment

MetS, Metabolic syndrome

MMF, Multimode fiber

NIRS, Near-infrared spectroscopy

OCT, Optical coherence tomography

OPO, Optical parametric oscillator

PA, Photoacoustic

PBS, Phosphate buffered saline

PVAT, Perivascular adipose tissue

ROC, Receiver operating characteristic

TCFA, Thin-capped fibroatheroma

US, Ultrasound

VH, Virtual histology

ABSTRACT

Author: Kole, Ayeeshik PhD
Institution: Purdue University
Degree Received: May 2018
Title: Depth-Resolved Assessment of Atherosclerosis by Intravascular Photoacoustic-Ultrasound Imaging
Major Professors: Michael Sturek, Ji-Xin Cheng

Coronary heart disease is the leading cause of death in the United States and the incidence is projected to increase by 18% by 2030. Yet, there remains a pressing clinical need for tools to detect vulnerable atherosclerotic plaques that can rupture and lead to major adverse cardiac events. Plaques that are considered most vulnerable for rupture are thin-capped fibroatheromas, which are grossly defined by hallmarks of a thin fibrous cap, a large lipid-rich necrotic core, inflammatory infiltrate, and positive remodeling. These plaques are often structurally non-obstructive to moderately obstructive, thus asymptomatic and clinically unidentifiable with routine angiography and stress testing. Rather, their vulnerability is a product of their chemical composition.

We have developed a dual-mode intravascular catheter which is capable of producing co-registered cross-sectional images of arterial wall morphology and lipid content, via ultrasound and photoacoustic modes, respectively. Validation of this capability will rely on interrogation of atherosclerotic coronary arteries from humans and peripheral arteries from swine, with comparison to gold-standard histopathology and competing technologies. Here, we present *ex vivo* validation of a novel intravascular photoacoustic-ultrasound (IVPA-US) imaging catheter and the first systematic *in vivo* IVPA-US imaging study in a preclinical swine model with native disease, necessary benchmarks before proceeding with translation to clinic. We aim to ultimately demonstrate predictive utility to detect plaques that are vulnerable to rupture and trigger adverse cardiac events. In addition, this will be instrumental in elucidating the mechanism of plaque rupture, the development of preventive and therapeutic interventions, and reducing coronary heart disease-related mortality.

1. INTRODUCTION

1.1 Atherosclerosis Definitions, Epidemiology, and Significance

Atherosclerosis is a chronic pathology of large- and medium-sized arteries, in which lipids, fibrous elements, and cellular debris progressively accumulate in the inner arterial wall forming a waxy substance termed a plaque [1, 2]. When atheromatous plaques build in the coronary arterial tree of the heart, the pathology is referred to as coronary artery disease (CAD), which continues to be the number one cause of death for men and women in the United States (Fig. 1.1) [3-5]. Plaques in the coronary artery can cause disease by encroaching upon the vessel lumen as they grow in size. Eventually, this narrowing or stenosis becomes severe enough to clinically present as chest pain upon exertion, or stable angina. The plaque can also suddenly rupture, exposing the pro-coagulant material within the plaque core to the coagulation proteins present in the blood stream, which triggers clot formation, or thrombosis [1, 6-8]. The resulting thrombus can lodge in a coronary artery and impede blood flow, causing acute coronary syndrome (ACS), which is an umbrella term for unstable angina and myocardial infarction. During a myocardial infarction, commonly known as a heart attack, lack of blood flow through the coronary arteries starves cardiac muscle of oxygen (ischemia), creating an infarct where the myocardium has been irreversibly damaged [6].

The American Heart Association estimates that the direct and indirect national costs of CAD are upward of $200 billion and that approximately every 44 seconds, an American will suffer from a myocardial infarction [3]. While research and advancements into the pathogenesis, diagnosis, surveillance, and treatment of coronary atherosclerosis has been prolific in the last two decades, immense challenges remain as CAD incidence is projected to increase by 18% in the next fifteen years [3-5].

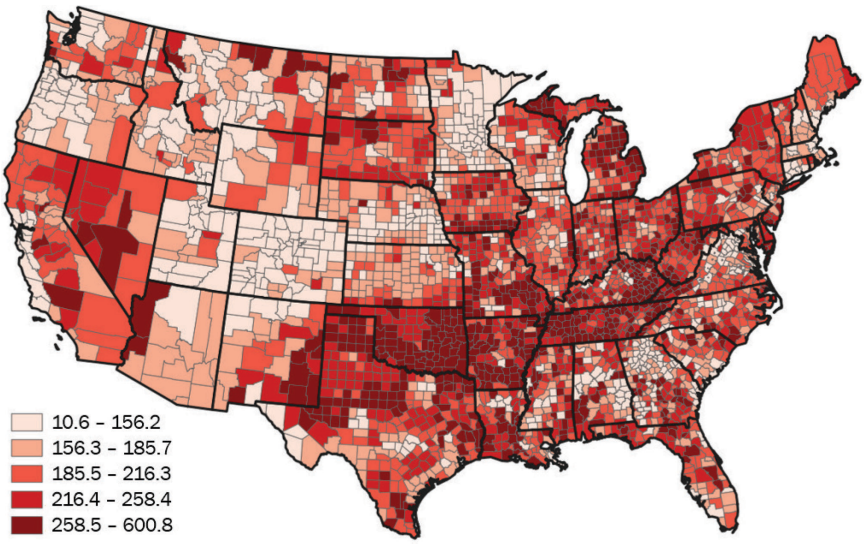

Figure 1.1. **Coronary artery disease death rate in the United States.** Map of the contiguous United States, showing the coronary artery disease death rate per 100,000 for all adults between 2013 and 2015. This map was created using the Interactive Atlas of Heart and Disease and Stroke, a website developed for the Centers for Disease Control and Prevention, Division of Heart Disease and Stroke Prevention. http://nccd.cdc.gov/DHDSPAtlas.

1.2 Atherosclerosis Pathogenesis

To achieve scientific progress towards combatting atherosclerosis, it is imperative to understand the etiology of the disease, which has only recently been realized to have a complex pathophysiology that is more involved than simple storage of excess lipids [2, 7-12]. The contemporary schema presents atherogenesis as a chronic inflammatory "response to injury" which begins with an insult to the endothelial cell layer that lines the inner most tunica intima of the artery [1, 2, 12]. Injury or dysfunction of the endothelium permits the entry and retention of lipids such as low-density lipoprotein (LDL) particles within the artery wall. Simultaneously, the activated endothelial layer also promotes adhesion of blood leukocytes, the most abundant of which are monocytes. Monocytes migrate into the intima and undergo maturation into tissue macrophages, which take up retained lipids intracellularly, becoming foam cells. An early stage lesion begins as a fatty streak, a flat yellow lesion of the intima present in most adolescents [1, 13]. With increasing age, a streak matures into a more complicated plaque with a significant lipid core that can potentially limit blood flow. A key process in the evolution of a streak to an advanced lesion is the migration and proliferation of smooth muscle cells (SMCs) from the tunica media (the middle layer of the artery) to the intima. This occurs primarily in response to

mediators such as platelet-derived growth factor, released by local platelets present to heal vascular injury. Along with intimal proliferation, media-derived SMCs also synthesize and deposit extracellular matrix components contributing to a fibrous cap over the plaque. Many of the lipid-laden macrophages die and release extracellular lipids [1, 10, 11, 14]. A combination of cellular debris and lipids constitute a lipid-rich necrotic core, which is particularly thrombogenic if the fibrous cap covering the plaque ruptures, ulcerates, or erodes (Fig. 1.2) [1, 6, 11, 15, 16].

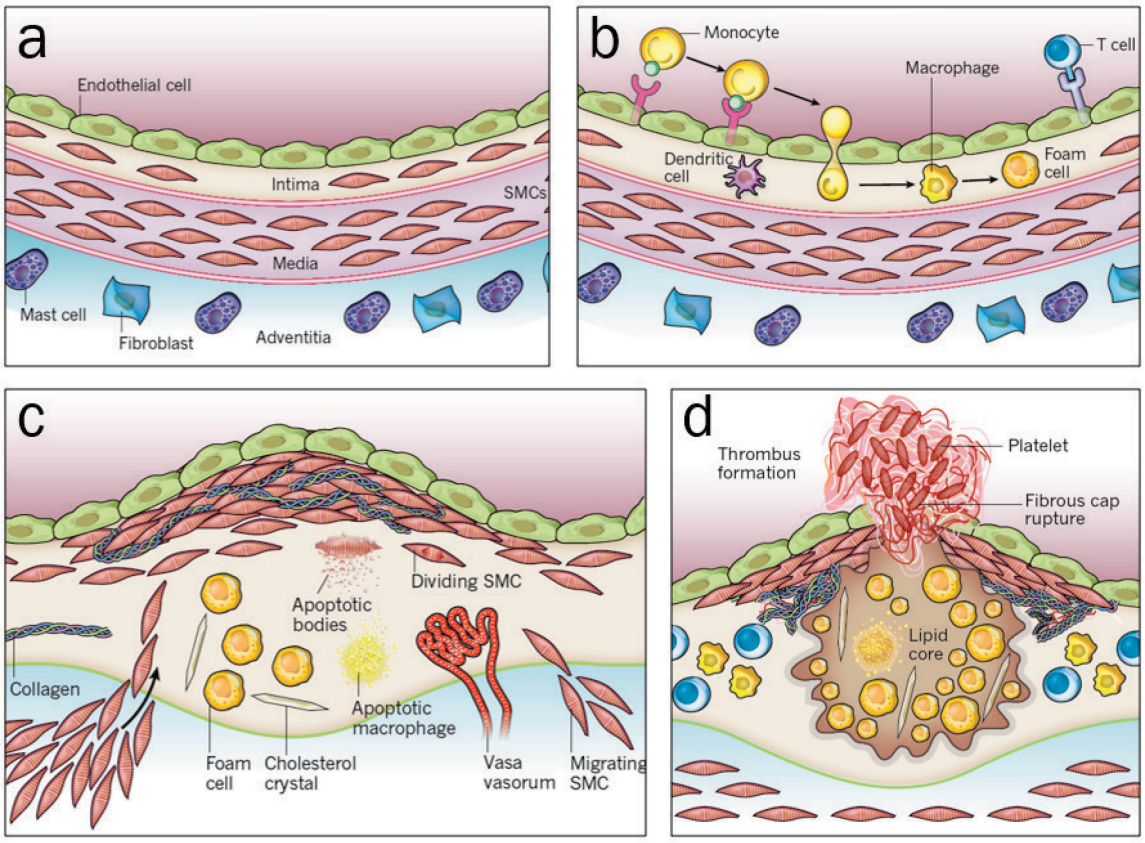

Figure 1.2. **Pathophysiology of atherosclerosis.** A) Normal artery anatomy with three layers: tunica intima, tunica media, and tunica adventitia. B) Activated endothelium recruits inflammatory monocytes that migrate into the intima. After maturation to macrophages and lipid uptake, they become foam cells. C) Migration and proliferation of smooth muscle cells (SMCs) from the media to the intima. There is also increased extracellular matrix deposition. In advancing lesions, SMCs and macrophages die by apoptosis, leaving behind necrotic debris intermixed with lipid. D) Rupture of the fibrous cap presents the pro-coagulant plaque material to blood, triggering thrombus formation and the obstruction of blood flow. Adapted from Libby et al. (*Nature*, 2011).

1.3 Thin-Capped Fibroatheromas and the "Vulnerable" Plaque Hypothesis

The susceptibility of a plaque to rupture and subsequently trigger ACS is defined as its vulnerability [17, 18]. While a previous American Heart Association classification delineated atherosclerotic lesions into six classes: three pre-atheromatous (types I-III) and three atheromatous (types I-IV), this scheme has been criticized for its implication of a linear, orderly progression of lesion type [19, 20]. With new morphometric data from autopsy specimens, the classification scheme has been revised into seven morphological categories that better illustrate our current understanding of atherosclerosis: intimal thickening, intimal xanthoma (fatty streak), pathologic intimal thickening, fibrous cap atheroma, thin-cap fibrous atheroma (TCFA), calcified nodule, and fibrocalcific plaque (Fig. 1.3) [21-23].

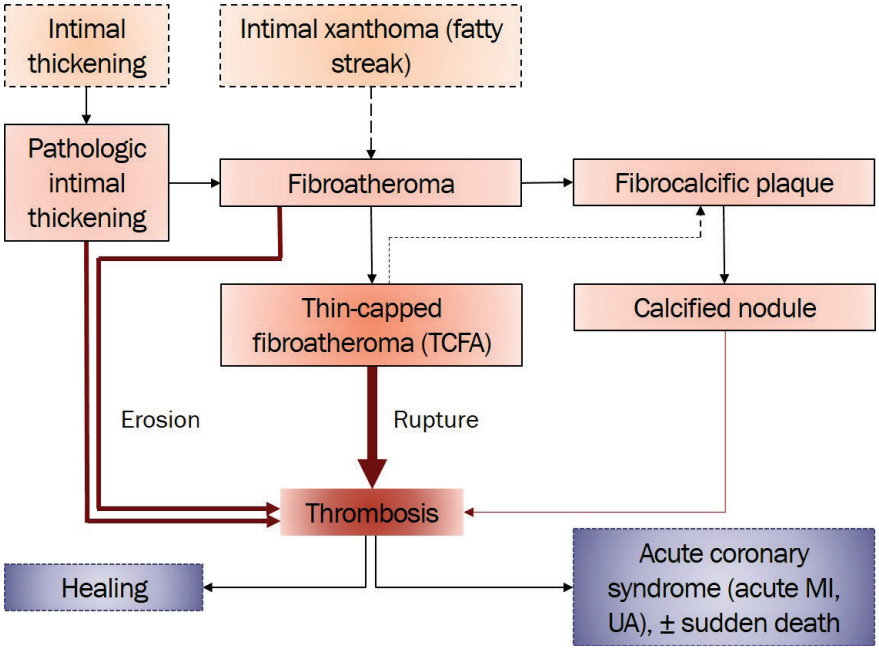

Figure 1.3. **Simplified scheme for classifying atherosclerotic lesions based on morphology**. The classification scheme has been modified from the current American Heart Association recommendations, with the seven major subtypes depicted in light orange boxes. This scheme better illustrates the non-linear progression between subtypes, and advancement to plaque events (erosion, healing, and thrombosis) and major adverse cardiovascular events, such as acute coronary syndrome. The thickness of lines indicate the estimated frequency of each pathway. Adapted from Yahagi et al. (*Nat Rev Cardiol*, 2016).

A fracture of the thin, collagen-poor cap of a TCFA makes this plaque morphology type the most common precursor to an atherothrombotic event, and consequently the most common vulnerable plaque [15, 16, 18, 21, 22, 24-28]. In addition, these rupture- and thrombosis-prone plaques are often positively remodeled and non-obstructive, thus

evading detection on routine stress testing and coronary angiography [26]. Positive remodeling is a compensatory enlargement of the media and external elastic membrane (EEM) of an artery during atherogenesis [29, 30]. As a result, plaques can increase in size without reducing luminal area, and is a phenomenon characteristic of unstable, vulnerable plaques [29, 31].

There is currently no diagnostic test routinely used in practice to reliably identify TCFA, despite the pressing clinical need. Identification of vulnerable plaques before rupture will be instrumental in fully realizing the mechanisms underlying lesion progression to ACS, the future development of preventative and therapeutic interventions, and reducing CAD-related morbidity and mortality. Catheter-based imaging modalities may hold the answer, as they continue to advance technology necessary to detect pathologic hallmarks of TCFA, such as a thin fibrous cap, large lipid-rich necrotic core, inflammatory infiltrate, and positive remodeling (Fig. 1.4) [32].

A more detailed definition recognizes the most important histological marker of a true TCFA as a sufficiently thin cap (<65 μm). This threshold has been determined from human autopsy studies of 41 ruptured plaques, in which 95% of fibrous caps measured less than 64 μm [22, 33, 34]. In addition, mechanical studies have shown that circumferential stress increases exponentially as cap thickness decreases [24, 35]. Moreover, this cap demonstrates dense inflammatory infiltration, with >25 macrophages per high-magnification field (0.3 mm diameter field) [33]. The prevailing hypothesis proposes that inflammatory cells and subsequent cytokines drive the production of proteases (e.g. collagenase, gelatinases, stromolysin, and cathepsins), thus weakening an already thin cap via extracellular matrix breakdown [2, 22, 24, 36-39].

Another key feature is a large lipid-rich necrotic core, which was commonly hypothesized as a core composing ≥40-50% of plaque area [40, 41]. However, more recent studies have found evidence of a smaller necrotic core (23 ± 17%) in unruptured TCFAs and slightly larger in plaque ruptures (34 ± 17%) [22, 41]. Although the necrotic core of a TCFA is lipid-rich, it is distinct from a lipid pool, which is considered a more nascent lesion. A necrotic core characteristically displays cellular debris of apoptotic cells and cholesterol clefts, whereas a lipid pool is collection of lipids within a proteoglycan-rich matrix [42].

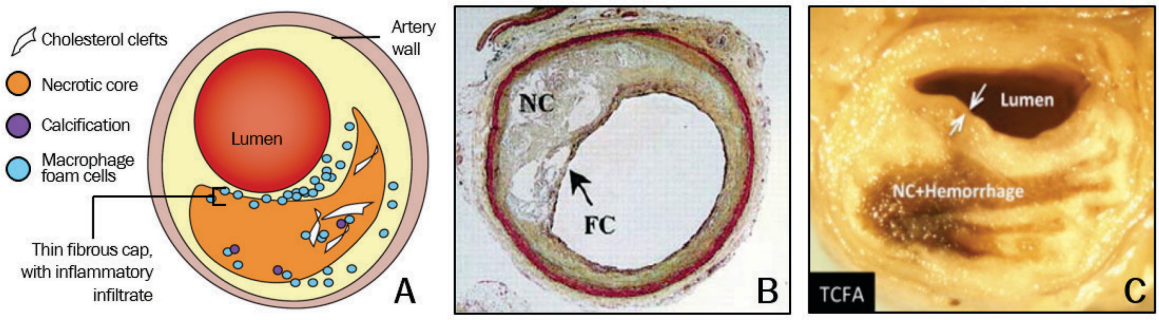

Figure 1.4. **Thin-capped fibroatheroma hallmarks.** A) Schematic of a TCFA showing a patent lumen and a lipid-rich necrotic core with cholesterol clefts covered a thin fibrous cap with inflammatory infiltrate. B) Histopathology of a TCFA showing the thin fibrous cap (FC) and necrotic core (NC). C) Gross image of a TCFA with a hemorrhaged necrotic core (NC) and a thin fibrous cap shown between the arrows. Adapted from Yahagi et al. (*Nat Rev Cardiol*, 2016), Virmani et al. (*Arterioscler Thromb Vasc Biol*, 2000), Narula et al. (*J Am Coll Cardiol*, 2013).

Furthermore, studies have shown that an increased free-to-esterified cholesterol ratio within the core promotes plaque rupture [43]. The core also contains increased tissue factor, contributing to its thrombogenic potential [44].

Lastly, due to aforementioned positive remodeling, the majority of TCFAs produce <75% area stenosis, which may render the lesion clinically asymptomatic [25, 45-49]. Another relatively less-established finding of TCFA composition is neovascularization of the plaque from the tunica adventitia (the outermost vessel layer). This has been hypothesized to be an early defensive pathway to protect against hypoxia in a thickening plaque and also promote lipid removal. However, in advanced lesions, it also permits increased leukocyte influx to the plaque and inflammatory plaque destabilization [24, 50, 51]. Experimental evidence has shown increased vasa vasorum microvessel density and expression of endothelial adhesion molecules (e.g. ICAM-1, VCAM-1, E-selectin, and CD40) in lipid-rich plaques [52].

Thus, definitive classification of a plaque as a TCFA requires identification of these key histomorphic features. Furthermore, it must be done with ample sensitivity and specificity to provide predictive utility in the clinic [53]. Intravascular imaging via catheter probes offer the best opportunity to address this gap. It is likely this will necessitate a multi-mode imaging tool, as no single modality is currently powerful enough to identify all hallmarks of a TCFA: a thin-fibrous cap with inflammatory infiltrate, large lipid-rich necrotic core, and positive remodeling [54-61].

1.4 Overview of the Current Coronary Imaging Landscape

The following overview outlines the current status of intravascular coronary imaging modalities and, by extension, hybrid modalities. For each modality, the history and background, current status, advantages and shortcomings (in the context of TCFA detection) will be presented (Table 1.1). All presented modalities are commercially available, except the intravascular photoacoustic (IVPA) imaging catheters, of which the development and validation is the focus of this dissertation. To narrow the scope, other promising technologies are not discussed due to their limited body of current evidence. This includes near-infrared fluorescence imaging [62-65], near-infrared autofluorescence imaging [66, 67], and fluorescence lifetime imaging [68-71].

1.4.1 Coronary X-ray Angiography

For over 50 years, coronary X-ray angiography has been a predominant diagnostic imaging technique for identifying coronary anatomy and obstructive disease [72]. A trained cardiologist inserts a flexible catheter through the femoral or brachial artery and threads it into the coronary arteries of the heart (cardiac catheterization), where they inject iodine-containing contrast dye. The cardiologist then uses steady beams of X-ray (fluoroscopy) to produce a real-time image of the entire coronary arterial tree, or an angiogram, with a spatial resolution of 130 to 200 μm (Fig. 1.5) [73]. The value in seeing coronary arteries has revolutionized cardiovascular medicine and been the gold standard in assessing disease severity and guiding revascularization decisions, although this status has recently been fading. While certainly at no risk of being replaced, there is a strong push for angiography to be supplemented with additional imaging modalities [74, 75].

Angiography has lost its luster due its limited capabilities [76-79]. Angiograms are only able to display two-dimensional, planar silhouettes of the vessel lumen. As a result, angiography has little diagnostic power in identifying plaques without functionally significant stenosis, such as positively remodeled plaques [76]. Compensatory positive remodeling is characteristic of vulnerable plaques and aids reasoning for the observed discordance between reduced lumen diameter and progression to ACS [31, 48, 78, 80, 81]. Evidence from the late 1980s shows that in 66% of patients who presented with acute MI, the occlusion occurred in areas that were previously normal on angiogram. Additionally,

only 3% of acute MI patients had a previous high-grade stenosis on angiogram at the site of occlusion [82]. This observation has driven further research and yielded the consensus that non-obstructive lesions are a common source for ACS and vulnerability is a product of plaque composition [18, 40, 41]. Angiography lacks the ability to provide information about the arterial wall, and consequently, the ability to assess TCFA determinants: thin cap with inflammatory infiltrate, lipid-rich necrotic core, and positive remodeling. Thus, while angiography will continue as a valuable mainstay in cardiology, its limitations have ushered in a wealth of new intravascular imaging modalities that can better detect vulnerable plaques [54, 74, 76, 77, 83].

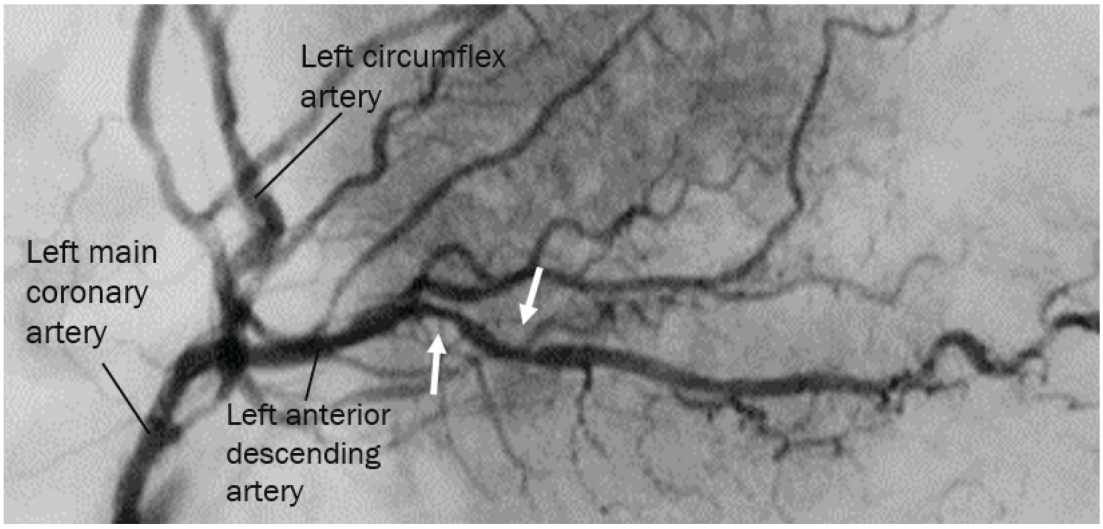

Figure 1.5. **Coronary angiogram**. Angiogram from an 85-year old male with history of coronary artery disease. Arrows indicate areas of significant obstruction of the left anterior descending artery, immediately distal to the first diagonal artery.

1.4.2 Grayscale Intravascular Ultrasound

The first ultrasound (US) images from within a human coronary artery were captured by Paul Yock and colleagues in 1988 using a miniaturized single transducer system [84]. Since then, intravascular ultrasound (IVUS) has served as the most prominent catheter-based imaging device in the cardiac catheterization lab. It is commonly used to supplement angiography for assessment of stenosis severity and guide percutaneous coronary intervention. In the last two decades, the role of IVUS in the catheterization lab has expanded to include optimization of stent implantation and prediction of complications [85-88]. Furthermore, IVUS has played a pivotal role in research and influenced current clinical guidelines and our understanding of atherosclerosis natural history via serial

progression/regression studies [74, 76, 87-103]. While its versatility is undisputable, the scope of this section will focus on its ability (or lack of ability) to delineate vulnerable plaque, in regards to morphology and especially composition.

To appreciate the strengths and limitations of IVUS in characterizing plaque, it is essential to understand the technology underlying image formation and basics of the procedure. A typical IVUS imaging device consists of three main components: the catheter (typical diameter: 1 mm) with an US transducer at its tip, a motorized pullback console, and a wired signal processing system that displays visual output. US transducers generate acoustic waves proportional to the voltage applied to a piezoelectric (pressure-electric) material, via expansion and contraction of the material. The typical IVUS transducer frequency is within the range of 20-60 MHz and is transmitted perpendicular to its axis. After encountering tissue, a percentage of the emitted wave returns to the piezoelectric material and imparts mechanical pressure, which is converted to an electrical signal that is amplified, filtered, and reconstructed. The variation in signal intensity received (i.e. backscattered, reflected) provides information on how much the emitted signal was attenuated, and therefore tissue density and type. In addition, with temporal delay between signal emission and reception, tissue position is recovered. This information is displayed together as various shades on a gray scale. The length of a vessel can be imaged via cardiac catheterization of the IVUS catheter to the distal end of a coronary artery and motorized pullback (0.5-1 mm/s) of the catheter—or transducer within a catheter sheath—towards the proximal ostium [85, 86, 104-107].

There are two different types of IVUS transducers, both of which are able to reconstruct a real-time 360^{o} cross-sectional topography of the vessel wall (Fig. 1.6A). Rotation (or mechanical) IVUS catheters are composed of one piezoelectric transducer that rotates up to 1,800 rotations/minute via flexible, high-torque drive shaft that extends the length of the catheter to the motorized pullback console. The single transducer element sits perpendicular to the catheter and scans the vessel cross-section as it spins within an echolucent sheath, protecting the endothelium from damage during pullback. Commercial rotational IVUS catheters all operate approximately at a center frequency of 40 to 50 MHz with a small bandwidth. As a result of these higher transducer frequencies, mechanical systems have the advantage of superior axial resolution (100-120 μm). The trade-off,

however, comes from frequency-dependent attenuation that limits tissue penetration depth to approximately 5 mm. This is still ample depth for assessment of positive remodeling. Newer transducer technology expands depth resolution up to 16 mm with an extended bandwidth that includes frequencies between 30 and 70 MHz [58, 108-110].

In contrast, an electronic phased-array catheter has multiple piezoelectric transducer elements arranged circularly around the catheter tip. This solid-state design scans the vessel cross-section with circumferential activation of the imaging elements via an embedded microchip proximal to the transducer. Electronic signals are then transmitted by microcables to the processing system where imaged sectors are reconstructed. The processing time for reconstruction and the lower frequency at which phased-array catheters operate give this design the disadvantage of lower temporal and axial resolution (150-250 μm), but the advantage of a higher tissue penetration depth [111]. The catheter itself retreats during pullback, as the solid-state design does not necessitate a sheath. Commercial phased-array IVUS catheters typically contain 64 elements and operate at 20 MHz [74, 83, 85, 86, 104-107, 112, 113].

Despite variations in transducer design, IVUS image interpretation of the cross-sectional vessel topography is unchanged. Normal US appearance of a coronary artery roughly mimics histology with the presence of three layers: intima, media, adventitia [114-116]. Each of the layers vary in their ability to reflect acoustic signal. The intima is relatively echogenic given the drastic change in acoustic impedance at the lumen-intima border. The muscular media layer is homogenously composed of SMCs and echolucent, as US transverses the layer without much reflection. Lastly, the adventitia is strongly echogenic, a property of the abrupt change in impedance at the media-EEM border. Together, the bright echoes of the intima and adventitia separated by a dark media is classically described as the “three-layered” IVUS appearance of a coronary artery (Fig. 1.6B-D) [74, 85, 86, 104, 105, 117]. However, there are deviations to the three-layer appearance, particularly in young patients with an intimal layer too thin to be resolved with IVUS [118]. Thus, the IVUS image appears as a monolayer, composed solely of the echogenic adventitia. Though, in most patients requiring cardiac catheterization, there is sufficient and diffuse intimal thickening to appear on imaging and distinguish the three

layers [85, 86, 105]. It is controversial whether this trilaminar appearance is truly normal or a sign of early atherosclerosis [119, 120].

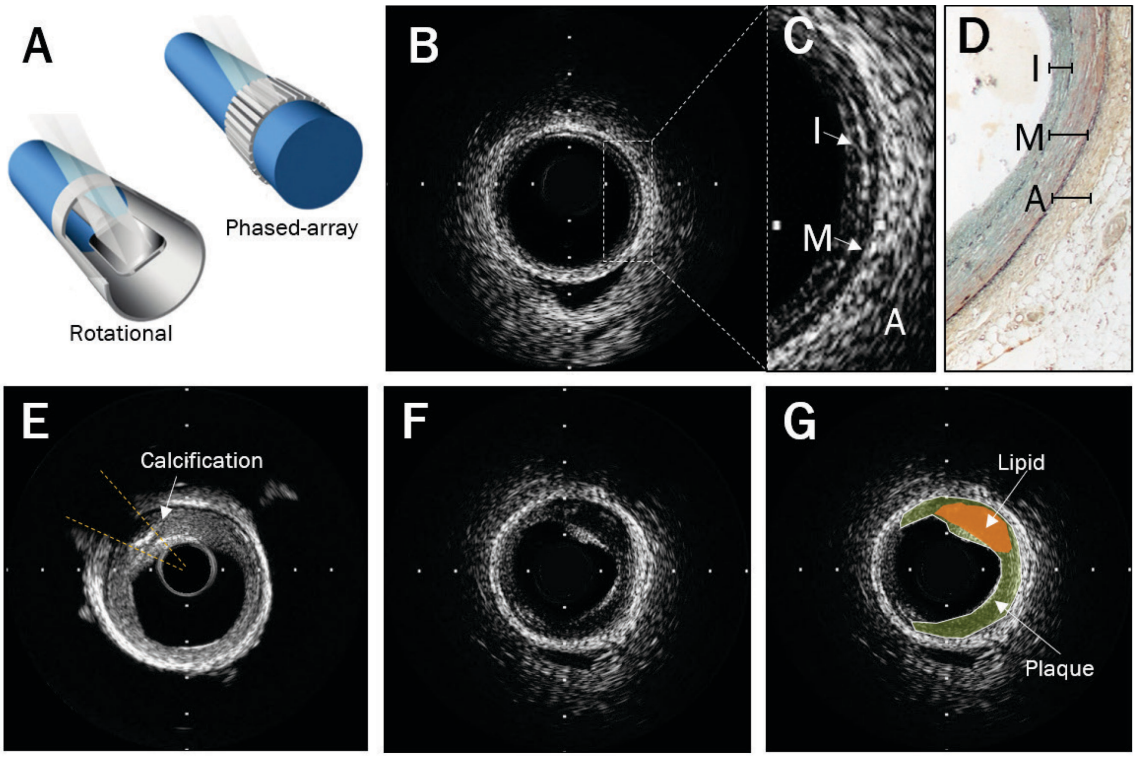

Figure 1.6. **IVUS catheter schematics and image interpretation.** A) Schematic of rotational and phased-array IVUS catheter probe tips. In rotational catheters, a single transducer elements rotates to image the vessel wall. In phased-array catheters, a series of transducers are sequentially activated to image the vessel wall. B, C) IVUS image showing a healthy "three-layer" appearance of the intima (I), echolucent media (M), and adventitia (A). D) Corresponding histology showing the same three layers. E) Echogenic calcification with the arc of "acoustic shadowing" peripheral to the deposit outlined. F, G) Plaque (blue) detected by IVUS, with lipid (green) identified by its echolucent nature. Panel A adapted from Kume et al. (*Cardiology: An Illustrated Textbook*, 2012).

IVUS has strong evidence showing that it is a valuable modality in detecting atheromatous plaque composition. It has high specificity and sensitivity for detection of coronary artery calcification [121-124]. The signature of calcium deposits are their ability to prevent US penetration, creating an "acoustic shadow" peripheral to the deposit (Fig. 1.6E). Calcification, while important in other plaque subtypes (calcific nodule, fibrocalcific plaque), is not a major component of our lesion of interest: TCFAs [21]. IVUS has high sensitivity (78-95%) for the detection of lipid pools that show up as echolucent (Fig. 1.6F,G). Specificity, though, is poor (30%) and cannot reliably differentiate between other echolucent zones produced from loose tissue, shadowing, or plaque rupture [54, 83, 86, 125, 126]. In addition, the hallmark of a TCFA is lipid-rich necrotic core, meaning it is

present with cellular debris that would reflect US differently than a uniform pool [127]. In general, a lipid-laden lesion that has not yet ruptured will present with an echogenic fibrous cap. However, as discussed before, the resolution of IVUS cannot distinguish features <100 μm and delineate the characteristic thin cap of a TCFA. This obstacle is unlikely to be overcome because at transducer frequencies above 45 MHz, the US reflection from aggregate blood cells—blood speckle—distorts a clean lumen-tissue interface [74, 104, 128]. Lastly, microbubble contrast-enhanced IVUS can identify vaso vasorum as a surrogate marker of plaque inflammation, but is not widely verified [129, 130].

Despite the highlighted limitations in detection of TCFA characteristics, IVUS has great clinical predictive value. The Providing Regional Observations to Study Predictors of Events in the Coronary Tree (PROSPECT) trial was a multicenter natural history study of atherosclerosis using intravascular imaging to prospectively identify vulnerable plaque in 697 patients. PROSPECT showed that plaque burden >70% and minimal lumen area <4 mm^2, as determined by grayscale IVUS, were independent predictors of future major adverse cardiovascular events (MACE) within 3.4 years at nonculprit (obstructive lesions remote from the area of infarction) lesion sites (p<0.0001, HR=7.9, 5.0, respectively) [100]. Plaque burden refers to the area within the EEM occupied by atheroma and does not necessarily correlate with stenosis, especially in the setting of positive remodeling [131]. These results provide strong evidence that a large plaque burden and/or small minimal lumen area, as measured by grayscale IVUS, should be considered alongside traditional TCFA hallmarks in future investigations. Furthermore, the few limitations of grayscale IVUS in identifying these hallmarks can potentially be improved by sophisticated radiofrequency (RF) analysis of the reflected US beam, also known as Virtual Histology (VH)-IVUS.

1.4.3 Virtual Histology-Intravascular Ultrasound

IVUS grayscale images are formed by measuring the amplitude of the reflected US signal wave, discarding other spectral parameters. RF analysis profits by extracting the loads of discarded spectral information, using it to differentiate four plaque components—fibrous, fibrofatty, necrotic, calcific—that were previously undistinguishable based on amplitude alone [54, 85, 86, 105, 132]. In 2002, Anuja Nair and colleagues were first to

show RF analysis using eight spectral parameters of the reflected signal could be used to discern tissue components with sufficient predictive accuracy, as validated from 51 fresh, post-mortem left anterior descending arteries compared to histopathology [133, 134]. This validation study was repeated using a commercial 20 MHz phased-array catheter and an algorithm trained to color map tissue components based on their spectral signatures (Fig. 1.7) [135]. Fibrous tissue (dark green), fibrofatty (light green), necrotic core (red), and calcium (white) were identified with predictive accuracies of 93.5%, 94.1%, 95.8%, and 96.7%, respectively. This led to the first commercially available RF-analysis IVUS system: Virtual Histology® IVUS (Volcano Corp.).

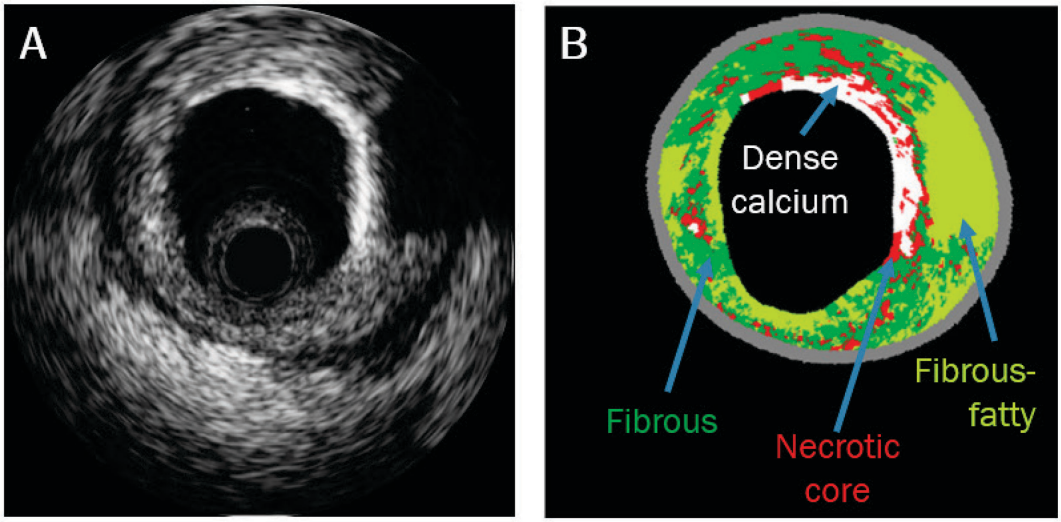

Figure 1.7. **Virtual Histology-IVUS colorized classification.** A) Grayscale IVUS image of an atherosclerotic plaque. B) Colorization of four different plaque components by VH-IVUS algorithm based on RF-analysis. Adapted from Muramatsu et al. (*J Cardiol*, 2015).

VH-IVUS has also been successfully validated *in vivo*, as there is strong correlation between *in vivo* VH-IVUS measures and *in vitro* histopathology of the same plaques obtained by atherectomy. Predictive accuracy ranged from 87.1% to 96.5% [136]. These studies and many others have shown validity and reproducibility of VH-IVUS as a diagnostic technology, thus renewing the outlook of IVUS in TCFA detection [137-141].

The next logical step from identifying individual plaque components is to use this information to classify plaques based on phenotype. However, despite the improvements of VH-IVUS, it is still limited by insufficient resolution to detect a thin fibrous cap [142]. Thus, investigators have formally defined what is known as a VH-TCFA (or IVUS-derived TCFA), based on *ex vivo* histological analysis. A VH-TCFA is a lesion that, on at least

three consecutive frames, contains a necrotic core ≥10% without an overlying fibrous cap and a total plaque burden ≥40% [143]. This deviation from the histological definition is problematic, particularly because it promotes a false assumption that absence of a detectable cap means it is thin [89, 144]. In reality, this means the cap is below resolution limits (<150-250 μm) and the lesion cannot be definitively classified as thin-capped versus thick-capped. The notion that VH-TCFA is a reliable inference of true histological TCFA has received further criticism. Many experts have questioned whether VH-IVUS can accurately distinguish lipid pool from necrotic core, as they may overlap [32, 127, 145]. Additionally, others have highlighted that RF signal properties can be altered by factors other than tissue property. For example, it has been shown that VH-IVUS misidentifies stent struts as calcium surrounded by necrotic core [146].

Furthermore, Granada et al. produced evidence in a swine model of poor correlation between plaque components identified by VH-IVUS and those identified by gold-standard histopathology [147]. More recently, Thim et al. demonstrated that the necrotic cores as identified by VH-IVUS were grossly misclassified as compared to histopathology in 18 lesions in an atherosclerotic minipig model [148]. In both instances, the results were met with harsh criticism from experts in the field [149, 150]. Primarily, they cite that swine atherosclerosis is not an accurate representation of complex human coronary plaques and that necrotic cores differ in composition. Thus, it is irresponsible to expect VH-IVUS, an algorithm constructed from post-mortem diseased human arteries, to correctly identify swine pathology.

Regardless of the uncertainty and controversy regarding VH-IVUS, it has shown clinical value in the PROSPECT trial. Presence of a VH-TCFA was an independent predictor of MACE within the 3.4-year follow-up period (p<0.0001, HR=3.8), along with the previously mentioned measures derived from grayscale IVUS [100]. These findings are in accordance with two smaller prospective clinical trials [151, 152]. Yet, the majority of the lesions identified as VH-TCFAs at baseline in the PROSPECT trial healed did not result in MACE (Kaplan-Meier event rate = 4.4%) and those that did progress were severe lesions associated with large plaque burden and/or small lumen [127]. This, again, raises the issue of whether a TCFA identified by VH-IVUS definition is the same as the rupture-prone histologically-defined TCFA. In 2016, the results of the first prospective randomized

clinical trial using VH-IVUS were published, concluding rosuvastatin treatment decreased VH-TCFA rate during 1-year follow-up [153]. However, the study suffered from incomplete patient follow-up, underpowered sample size, biased patient population, and lack of association with LDL-cholesterol levels. With each new VH-IVUS study, more questions are raised rather than answered, leading some to question whether the tool is a mere "gimmick" [154]. The role of VH-IVUS in identification of TCFA is limited until it is further validated, independently of grayscale IVUS, with future studies.

1.4.4 Optical Coherence Tomography

The technique of optical coherence tomography (OCT) was co-developed in 1991 by David Huang and colleagues [155]. After the first demonstration of successful *in vitro* imaging of the peripapillary area of the retina and a coronary artery, many in the group realized the endless potential of OCT as a high-resolution *in vivo* microscope. It has since revolutionized the study of ocular diseases and routinely used by ophthalmologists to guide clinical decisions [156]. The role of OCT in cardiology as an intravascular imaging modality for evaluation of atherosclerosis is not as well-formed, but continues to progress.

OCT is analogous to IVUS, with the central difference being that signals are generated via depth-resolved backscattered infrared light rather than reflected US (in the near-infrared ranged, with a central wavelength from 1250 to 1350 nm). Due to the fast speed of light, however, correlating a reflected light signal to position is nontrivial. OCT overcomes this obstacle with use of a Michelson interferometer, a half-mirror apparatus that splits monochromatic light into two beams directed to two "arms." In catheter-based OCT systems, one of the split light beams is diverted perpendicular to the catheter axis towards the arterial wall, the "sample arm." The other beam travels to a "reference arm" with a mirror. Both the tissue and mirror will reflect the light. However, coherent interference between the two returning light waves occurs only when light reflected from the sample arm comes from a tissue depth equal to the length of the reference arm. Incoherent reflections will wash out. Thus, interfering signal intensity at a certain reference arm length can provide tissue tomography at a known depth. Furthermore, variable translation of the reference arm mirror allows for incremental tissue penetration depth and 2D image reconstruction. Second-generation OCT systems, known as frequency domain

OCT, vary the laser source wavelength with a stationary reference arm length. Penetration depths can still be recovered via Fourier transform, and acquisition speeds are 15-50 times faster than the traditional, time-domain OCT [83, 105, 157-162]. Rotation and pullback of the OCT catheters are similar to mechanical IVUS systems.

OCT imaging via infrared light (1300-nm wavelength range) allows for high spatial resolution, in the range of 2 to 20 μm [163-165]. Thus, OCT boasts a 10-fold greater resolution than IVUS and is considered by some as the gold standard for measuring fibrous cap thickness (Fig. 1.8) [54, 166]. Jang et al. measured fibrous caps using OCT in patients presenting with acute MI versus those presenting with stable angina and found a significant difference in median thickness (47.0 μm vs. 102.6 μm, $p<0.05$) [167]. Similarly Kubo et al. showed that *in vivo* OCT measurement of fibrous cap thickness (49±21 μm) in 30 patients presenting with acute MI was more reliable than IVUS or angioscopy [166]. Others have also validated the ability of OCT to measure change in cap thickness in patients with acute MI between baseline and 9-month follow-up, with a significantly greater increase seen in the group treated with statins compared to the control group [168, 169]. Furthermore, it has been shown that OCT can detect macrophage infiltration within fibrous caps of plaques obtained at autopsy with 100% sensitivity and specificity in regions with >10% CD68+ staining [37, 170, 171]. Lastly, a relatively new technique called polarization-sensitive OCT can be used to measure collagen content and fiber thickness within fibrous caps and plaques [172]. Thus, OCT has the ability to measure the components of a fibrous cap that make it the most important determinant in plaque rupture: sufficiently thin (<65 μm), inflammatory infiltrate, and loss of collagen content.

Beyond cap characteristics, OCT has shown the ability to identify plaque components, similarly to VH-IVUS [164, 173-175]. One group performed *ex vivo* histological correlation of 357 diseased coronary segments obtained at autopsy with OCT imaging. This allowed characterization of lipid-rich plaques, fibrocalcific plaques, and fibrous plaques, with sensitivities and specificities ranging from 87% to 95% and 94 to 100%, respectively [176]. While OCT can resolve lipid-rich plaques as regions with low signal intensity, it cannot easily distinguish between lipid pool and necrotic core [24, 177-179].

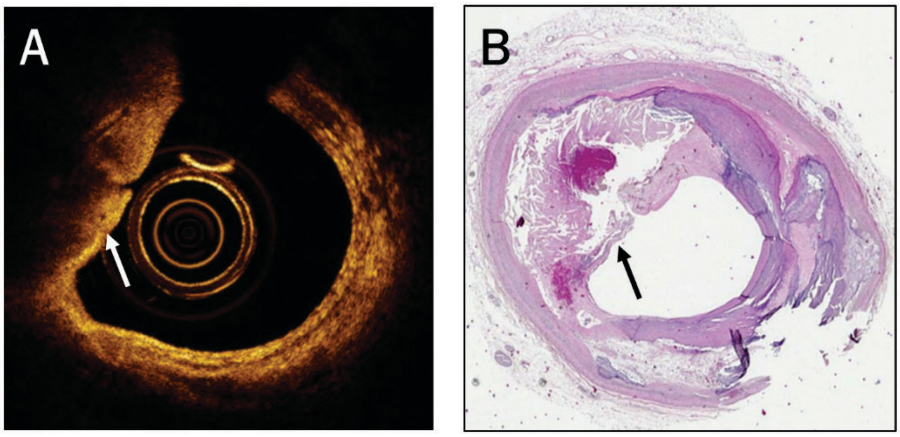

Figure 1.8. **OCT image of a TCFA and corresponding histology.** A) OCT image of a TCFA, with arrow indicating the thin fibrous cap. The rest of the plaque and composition, as shown by histology in (B), is not visualized due to limited depth penetration and lack of compositional specificity. Adapted from Phipps et al. (*Circ Cardiovasc Interv*, 2016).

A study performed on 79 diseased coronary segments showed misclassification of 41% of lesions, primarily due to an inability to differentiate areas of heterogeneous composition and low penetration depth [180]. Furthermore, a recent retrospective study of 1,474 patients reported association between OCT-detected lipid-rich plaques with a 2-fold increase in MACE at 2-year follow-up [181]. However, the methods defined lipid as a low signal region with diffuse borders and failed to link lipid-rich plaque morphology to lesion-specific clinical events [181].

Recently, researchers are incrementally addressing this challenge with the development of automated characterization algorithms to detect and quantify atherosclerosis via attenuation coefficient [182-185]. As validated *ex vivo* against histopathology, vulnerable plaque features were distinguished from other vessel wall components based on optical properties: necrotic core and macrophage infiltration exhibit attenuation coefficients (μ_t) $\geq$ 10 mm^{-1}, while fibrous and calcific plaques have a lower attenuation coefficients [186-188]. These findings have been confirmed *in vivo* against near-infrared spectroscopy (NIRS) in 85 patients, in which a defined Index of Plaque Attenuation $\geq$ 11 mm^{-1} differentiated between TCFA and fibroatheroma (p<0.0001) [183].

A shallow penetration depth (2 mm) is the overarching limitation of OCT imaging. This precludes it from imaging entire vessel walls, and therefore, assessment of total plaque burden and remodeling. Given the complementary nature of OCT with IVUS, Zhongping Chen and his group have successfully combined the modalities into a single catheter,

validated in preclinical settings [189-192]. This high-speed combination catheter has the advantage of two distinct contrast mechanisms: high-resolution of superficial structures from OCT-based optical scattering and visualization of the entire vessel wall from IVUS-based acoustic scattering. Another significant and practical limitation is the scattering of the 1300-nm wavelength light by red blood cells. To overcome this limitation, OCT necessitates displacement of blood by saline or iso-osmolar contrast flush (typically 3.0 mL/s). Alternatively, for OCT pullbacks of longer arterial segments, the artery may be occluded by a balloon proximally. However, this increases the risk of myocardial ischemia as seen by electrocardiograph changes and chest discomfort in the patient [54, 83, 157-159, 193, 194]. This risk has been minimized by the fast pullback speed of commercial devices (20 mm/s and 100 fps) and, in a five-year retrospective analysis, OCT-related complication rate did not differ from IVUS procedures (p=0.6) [195].

Despite its limited penetration depth and additional procedural requirements, OCT has the pivotal and distinct capability of measuring TCFA cap thickness with unmatched resolution. Furthermore, novel automated algorithms using attenuation coefficient may reveal additional value in characterization of plaque phenotype. Validation will require large natural history studies and more robust data, but it will not be surprising if OCT proves to be a synergistic component of future multimodal imaging platforms.

1.4.5 Near-infrared Spectroscopy

Diffuse reflectance near-infrared spectroscopy performs nondestructive identification of chemical components in biological tissue. NIRS works on the principle that, when a broadband light source (containing light over a range of wavelengths) encounters tissue, molecules become excited and enter a vibrational state in which they absorb light in the NIR range (750-2500 nm). This absorbance (y-axis) is measured and reported as a function of wavelength (x-axis) to form a spectrum characteristic of the imaged tissue. Chemical composition of the tissue is recovered via spectral analysis. Imaging in the NIR window is particularly valuable because both hemoglobin and water have relatively low absorbance at these wavelengths, making it compatible with blood [105, 196-198]. Current commercial catheters are capable of approximately 8000 real-time chemical assessments per 100 mm at a pullback speed of 0.5 mm/s [108, 199].

NIRS imaging for chemical composition was first demonstrated in atherosclerotic plaques from hypercholesteremic rabbits in 1993 [200]. This was further validated in 1996 in human carotid plaques obtained via endarterectomy that were compared against gel electrophoresis compositional analysis [201]. In 2002, Moreno et al. were the first to exploit the spectral signatures of plaque components obtained by NIRS to characterize a vulnerable plaque [202]. They analyzed 199 human aortic samples obtained at autopsy with NIRS and histology to identify lipid pool, thin fibrous cap, and inflammatory infiltrate. Half the samples were used as a reference set to construct a predictive algorithm, while the remaining samples were used to conduct blinded predictions. NIRS demonstrated excellent lipid detection, with a sensitivity and specificity of 90% and 93%, respectively. Substantial progress was made in two parallel studies that presented feasibility of a catheter-based NIRS system. The *ex vivo* study developed a predictive algorithm to detect lipid core plaques (LCP) through blood using coronary segments from 33 human autopsy hearts. Next, they showed prospective, double-blinded accuracy in detection of LCPs in 51 validation autopsy hearts (AUC=0.80 in ROC analysis) [203]. The parallel SPECTroscopic Assessment of Coronary Lipid (SPECTACL) trial subsequently demonstrated *in vivo* spectral similarity in 83% of enrolled patients [204]. Today, interpretation of NIRS data is completed by a proprietary computer-based algorithm based on these previous validation studies [203-205]. The automated analysis transforms NIR spectra into a colorized representation of the probability of LCP presence from 0 (red) to 1 (yellow). This is displayed visually as a fold-out map of the total vessel termed a "chemogram," in which each colored pixel represents 0.1 mm length (*x*-axis), 1^{o} angle (*y*-axis), and the LCP probability. This is also generated per frame, displayed circumferentially around a grayscale IVUS image, with which it is paired commercially (Fig. 1.9). The calculation of a lipid core burden index (LCBI) score provides a quasi-quantitative measure of LCP presence. LCBI is calculated as the fraction of valid pixels in which LCP probability is greater than 0.6, multiplied by 1000. The maximum LCBI can also be calculated for narrow (4 mm) regions of interest (max$LCBI_{4mm}$) [59, 108, 110, 206, 207]. In the past five years, many studies using NIRS-IVUS have revealed strong association between elevated max$LCBI_{4mm}$ (and LCBI) and cardiovascular outcomes in CAD patients [199, 208-217]. Furthermore, other studies have shown a significantly greater reduction in max$LCBI_{4mm}$ in

patients randomized to a high-dose statin therapy group compared to the standard dose group [218-220]. Yet, despite the plethora of completed research using NIRS-IVUS, there is no consensus of a maxLCBI$_{4mm}$ threshold for prediction of MACE. In 2016, Madder et al. reported a threshold maxLCBI$_{4mm}$ $\geq$400 as predictive for differentiation of ST-segment-elevation myocardial infarction culprit from nonculprit segments and predictive of future MACE at 1-year follow-up (p<0.001) [213, 216]. In 2017, a single-center prospective, observational study reported association between quartiles and continuous maxLCBI$_{4mm}$ values and higher risk of MACE at 4-year follow-up. They found a maxLCBI$_{4mm}$ $\geq$360 (inter-quartile range 4) to be predictive of future MACE (p<0.001, HR=3.58) [221]. It is anticipated that more precise maxLCBI$_{4mm}$ cut-offs will be determined within this year after the completion of two large prospective outcome trials: the Lipid-Rich Plaque (LRP) study with a 1,562 patient cohort and the PROSPECT II ABSORB study with a 900 patient cohort [222].

The overarching limitation of NIRS is an inability to provide explicit depth information regarding lipid deposition. Spectral data is collected within a depth of 1 mm or less and no resolution for axial distance from the catheter tip probe. This lack of depth-resolution stunts the capability of NIRS for localization of the lipid core in relation to other plaque components (i.e. fibrous growth, calcification, lumen border), quantification of the lipid core (i.e. volume and cross-sectional area), and differentiation between superficial and deep lipid depots (i.e. plaque lipid versus perivascular lipid) [58, 59, 199]. Thus, there is a reliance upon semi-quantitative metrics such as LCBI and maxLCBI$_{4mm}$, for which the interpretation and prognostic value are not yet clear.

Furthermore, fibrous cap thickness and macrophage inflammation are currently not able to be detected, but may be possible with the advent of extended bandwidth US transducers and sensing of inflammatory markers such as change in temperature and pH [223, 224]. Ultimately, the aforementioned prospective observational studies will determine the clinical prognostic value of NIRS for detection of vulnerable plaques and subsequent cardiovascular events. The outlook is promising, as it is currently the only FDA approved hybrid-modality catheter and has been used safely in over 80 hospitals worldwide and 16,000 patients since 2010 [222].

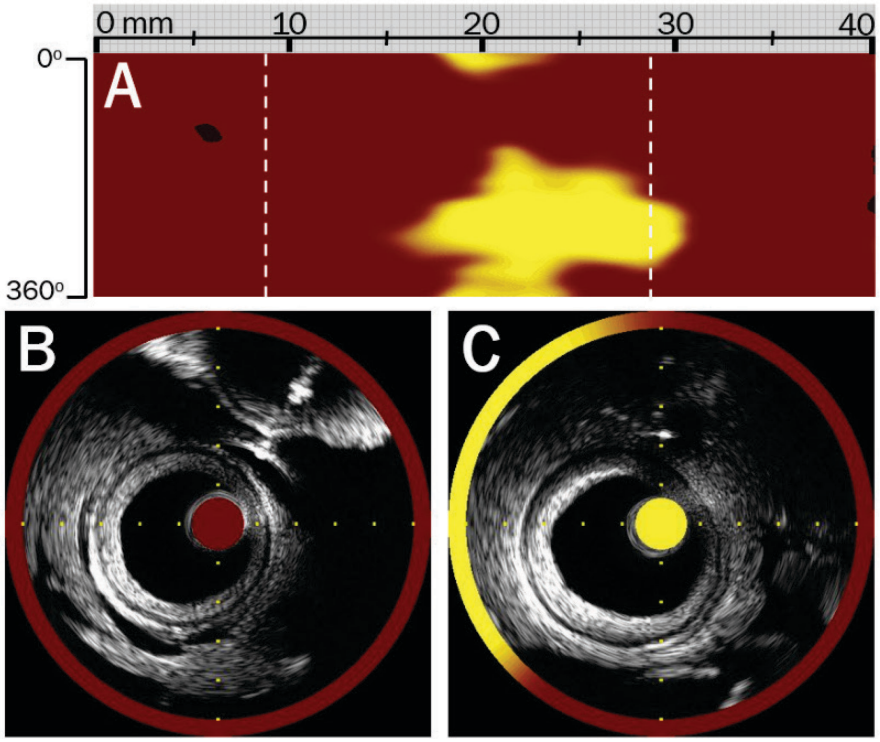

Figure 1.9. **NIRS chemogram and NIRS-IVUS images.** A) Chemogram showing a 2D representation of lipid (yellow) and non-lipid containing tissue (red) with *x*-axis as the longitudinal pullback direction and -axis as the longitudinal pullback direction and *y*-axis the rotation degree. B) Grayscale IVUS image shown in the inset, with NIRS information shown circumferentially suggesting no lipid is present at this cross-section of the artery. C) Grayscale IVUS, with NIRS information suggesting lipid is present with high probability from approximately 7 to 11 o'clock. However, the precise location and depth within the plaque is not given due to lack of depth resolution.

1.4.6 Photoacoustic Imaging

Intravascular photoacoustic (IVPA) imaging has been the latest modality added to the list of promising catheter-based tools in the detection for vulnerable plaque. Photoacoustic (PA) imaging has the advantage of both optical- and acoustic-based modalities: chemical selectivity without the use of labeling dyes and ample penetration depth. In PA imaging, the targeted tissue is exposed to a non-destructive nanosecond laser pulse. Absorption of optical energy results in molecular excitation and release of heat, which subsequently causes small thermal expansion. This expansion imparts a transient pressure rise that propagates acoustic waves, detected by an US transducer with depth location resolved via propagation time delay [225-229]. In IVPA catheters, the optical fiber and US transducer have been miniaturized to fit and interrogate the same field of view. PA images are co-registered with traditional US imaging, inherently performing as a dual-modality device

[230-235].

PA imaging has the ability to resolve different plaque components based on excitation wavelength, with lipids being the most successfully studied and validated due to their abundance in C-H bonds and large absorption coefficient [229]. 1.7 μm and 1.2 μm have been discovered to be suitable laser wavelengths representing C-H bond first and second overtone transitions, respectively, at which lipid-specific spectral features are generated with minimal water absorption (Fig. 1.10A). Thus, several groups have since exploited these optical windows to image lipid cores of atherosclerotic plaques [226, 230, 232, 233, 236-250]. Using 1.7 μm wavelength and a combined IVPA-US catheter system, Bo Wang et al. successfully imaged the lipid core of an atherosclerotic rabbit aorta *in vivo* and an atherosclerotic human coronary artery *ex vivo*, both of which correlated with histopathology in a limited proof-of-concept study (Fig. 1.10B, C) [244-246]. Following, Zhang et al. reported a larger systematic, longitudinal i*n vivo* and *ex vivo* validation study performed in atherosclerotic rabbits that showed quantitative correlation between lipid-rich plaque images collected by IVPA and histopathology [251]. Despite the many translational shortcomings of both works, it paved the way for future incremental advances [252]. Challenges such as image acquisition speed due to low laser pulse frequency had been an overarching limitation, but addressed over the past 2 years with advancements in new high-speed excitation sources, with two groups demonstrating real-time imaging speeds ≥20 fps [253, 254]. Furthermore, co-registration between PA and US channels has been improved by orientation of probe components in various successful designs (Fig. 1.10D-F) [233, 250, 255]. Lastly, this past year, Wu et al. performed the first *in vivo* demonstration of real-time IVPA-US imaging in a swine coronary artery through luminal blood [253, 256]. Furthermore, this study incorporated a protective polyethylene sheath enclosing the catheter (outer diameter: 1.3 mm), demonstrating safety of the imaging protocol and catheter flexibility in reaching the coronary artery via carotid access.

These breakthroughs have propelled IVPA imaging from being an experimental technique to one clinically translatable in the foreseeable future. Yet, there remain significant limitations with IVPA imaging [257]. While IVPA imaging has been shown to be acceptable through blood, sensitivity is still optimal and preferred with blood clearance or dilution with expensive saline heavy water (D_2O) [253, 254].

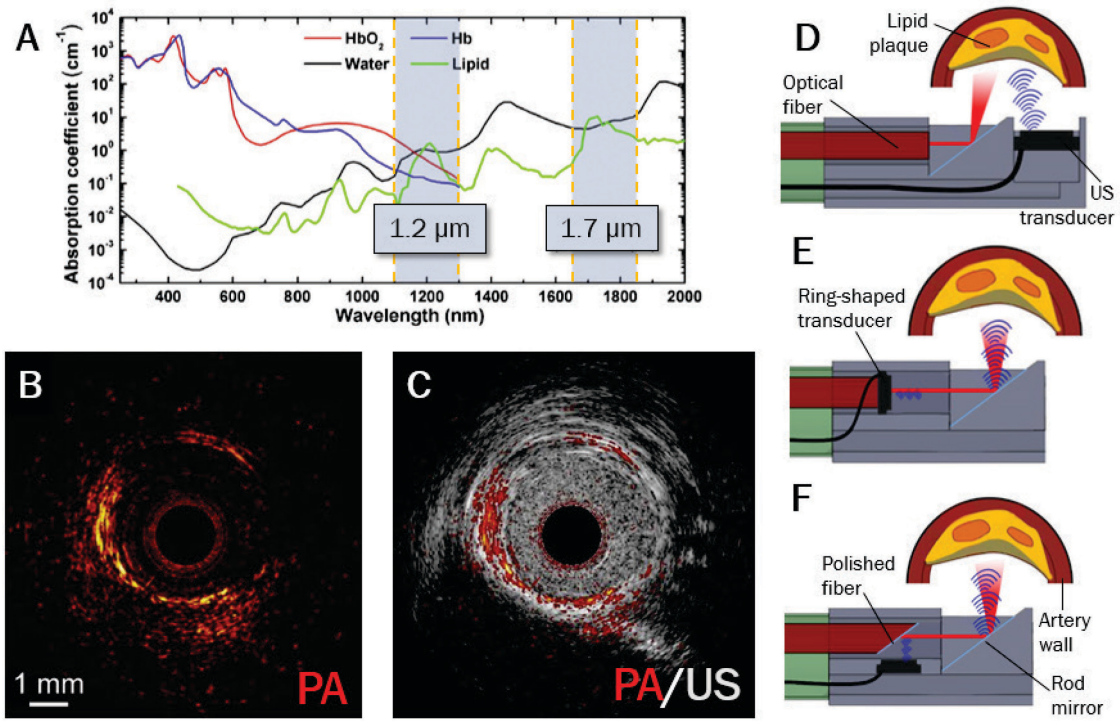

Figure 1.10. **IVPA imaging theory, example, and catheter probe designs.** A) Optical spectra showing absorption coefficient of lipid (green line) exceeds that of water (black line) at optical windows around 1.2 μm and 1.7 μm, thus making these wavelengths optimal for IVPA imaging. B, C) *In vivo* imaging of the abdominal aorta of an atherosclerotic rabbit reveals plaque lipid in the PA channel shown in B and localized within the artery wall when merged with the US channel shown in C. D) Front-to-back catheter design introduced by the Emelianov group and advanced by many others, in which there is an offset between the optical path reflection and transducer side-firing. This design has been miniaturized by the van Soest group to 1.3 mm in diameter with a sheath. E) Coaxial catheter design introduced by the Cheng group in which a ring-shaped transducer around the optical fiber allows for uniform optical and acoustic path overlap. However, further miniaturization of ring-shaped transducers is not currently feasible, limiting the probe diameter to a clinically-incompatible diameter of 2.9 mm. F) Collinear catheter design introduced by the Cheng group in which a series of reflections also allows for uniform optical and acoustic paths overlap in a smaller diameter probe (1.6 mm with sheath, data not yet published). This design has also been modified to reduce the number of ultrasound reflection surfaces and minimize signal loss by positioning of the transducer at a 10° angle for direct interrogation of tissue (quasi-collinear design, data not yet published). Panels A, B and C, D, E, and F adapted from Hui et al. (*Photoacoustics*, 2016), Wang et al. (*Ultrasound Med Biol*, 2012), Karpiouk et al. (*Rev Sci Instrum*, 2010), Wang et al. (*Sci Rep*, 2014), and Cao et al., (*Sci Rep*, 2016), respectively.

In addition, PA signals are generally weaker and contain lower frequency spectral components (<20 MHz), thus must be paired with extended-bandwidth transducers to obtain the best PA and US images [258]. Also, most common soft polymer sheath components contain the same C-H bonds that provide lipid contrast, creating a challenge in finding a material sufficiently transparent to not compromise optical and acoustic image quality [61]. The complete catheter diameter must also be further miniaturized to 1 mm or less, comparable to current commercial probes. While overcoming the aforementioned hurdles are within reach, the most pressing limitation remains a lack of validation of IVPA-

US imaging and classification algorithms in fresh human coronary arteries against gold-standard histopathology. In all previously overviewed modalities, FDA-approval, commercialization, and clinical trials were only possible after a publication of a key *ex vivo* validation study [135, 164, 203]. This, however, takes considerable effort and time: 1) practically for the collection of a sufficient *n* of fresh human coronary specimens that encompass a wide range of plaque phenotypes, 2) reproducibility of catheter fabrication, operation, and performance, and 3) calibration of image processing algorithms to match PA signal with lipid with adequate specificity and sensitivity. For IVPA researchers to meet these critical milestones within the next 5 years is foreseeable and in progress.

Furthermore, there is optimism for IVPA imaging for the identification of additional vulnerable plaque components. Spectral analysis of PA signals can be used to identify cholesterol esters versus pro-inflammatory cholesterol crystals [259-262]. Inflammation can also be visualized via exogenous absorbers targeted for macrophages or matrix metalloproteinases [263-265]. In addition, fibrous cap collagen content can be identified via multispectral imaging [247, 266, 267]. Lastly, depth resolution of PA imaging can differentiate between deep and superficial lipid depots, identifying perivascular adipose tissue (PVAT) which is a known mediator of atherogenesis and providing precise spatial location of lipid-rich plaque cores [242, 255, 267-269].

1.4.7 Summary

While each of the presented modalities offer an independent advantage in TCFA identification, they also leave something to be desired (Table 1.1). Angiography has been and will remain the gold-standard for visualizing the coronary arterial tree, but its inability to image the vessel wall precludes it from vulnerable plaque detection [270]. Grayscale IVUS has provided interventional cardiologists with the means to assess lumen dimensions, plaque morphology and burden, and positive remodeling [74, 85, 132]. Yet, its lack of resolution to define the thin fibrous cap of TCFAs with inflammatory infiltrate and characterize the lipid-rich necrotic core has opened doors for alternative tools. Despite the excitement surrounding VH-IVUS, which aims to characterize plaques via RF analysis of the same signal of grayscale IVUS, its ability to define plaque composition has limited validity [32, 127]. OCT undoubtedly presents the best resolution and ability to define

fibrous cap thickness, but lacks sufficient penetration depth to visualize the entire vessel wall for plaque characterization [158, 159, 271]. To date, NIRS has proven to be the most valuable in detection of lipid-rich plaques, but does not have inherent depth resolution needed to locate the core relative to lumen [196, 197]. IVPA can potentially provide detection of many plaque components with the advantage of depth resolution, but is currently limited to lipid detection and has not been thoroughly validated [226, 257].

Thus, the defining features of TCFAs—lipid content, cap thickness, inflammation, and positive remodeling—can all be visualized by various intravascular imaging modalities. However, this is not accomplished by a single tool alone. The development of dual- or even triple-modality catheters that provide complementary structural and compositional information is already underway, with NIRS-IVUS commercially available and IVPA-IVUS, OCT-IVUS, OCT-NIRS all in the preclinical phase [57-61, 109, 272-274].

The combined advantages of hybrid modalities will provide experts with detailed and more accurate characterization of vulnerable plaque pathophysiology. Evidence from the few prospective, observational clinical trials have suggested lesions that appear vulnerable for rupture on imaging are limited in number and not necessarily the ones that progress to a thrombogenic event. This discrepancy highlights the need for *in vivo* tools to study plaque rupture and vulnerable plaque prevalence, as our current understanding is limited to findings from post-mortem histopathology. This follows the truism that while "pathologists are always right, they arrive too late" [58, 61, 275, 276].

Beyond proving their value as research tools, it is the ultimate desire for intravascular imaging to be adopted for clinical decision making. For instance, early identification of patients with high-risk lesions could permit prophylactic intervention via bioresorbable vascular scaffolds or recommendation for aggressive pharmaceutical therapy, such as PCSK9 inhibitors or high-dose statins [277-283]. Whether intravascular imaging tools can advance to provide the prognostic information necessary to curb CAD-associated morbidity and mortality is still uncertain [32, 60, 154, 275, 280, 284-288]. This uncertainty should intensify our efforts towards the validation, optimization, and hybridization of intravascular imaging tools for vulnerable plaque detection.

Table 1.1 **Summary of Intravascular Imaging Modalities**

Technology	Angiography	IVUS	VH-IVUS	OCT	NIRS (-IVUS)	IVPA (-US)
Contrast mechanism	Radiopaque dye	Acoustic scattering	Acoustic spectrum	Optical scattering	Optical absorption	Optical absorption
Axial Resolution	130-200 µm	100-120 µm	150-250 µm	2-20 µm	N/A	80-200 µm
Penetration Depth	N/A	> 5 mm	> 5 mm	< 2 mm	1-2 mm	5-6 mm
Positive remodeling	-	+++	+++	-	+++	+++
Fibrous cap	-	-	-	+++	+	*
Lipid core	-	+	++	++	+++	+++
Inflammation	-	-	-	+	-	*
Current Status	CU	CU	CA/CS	CA/CS	CA/CS	PCS

Capability of each modality for the assessment of thin-capped fibroatheroma hallmarks is presented with the following scale: +++, excellent; ++, good; +, possible; -, not currently possible; *, under investigation; The capability of NIRS and IVPA to assess positive remodeling and fibrous cap were evaluated with the assessment that they are paired with IVUS, as they are only commercially available or being developed in that form.

CU, clinically used; CA, clinically available; CS, clinical studies ongoing; PCS, preclinical studies

Modified with current evidence from following references: [24, 36, 55, 56, 61, 105, 113, 128, 157, 159, 162, 175, 194, 206, 226, 289-292]

1.5 Scope and Aims of the Current Investigation

We hypothesize a dual-modality IVPA-US imaging catheter can detect, localize, and quantify lipid content in atherosclerotic arteries, providing prognostic value for the early identification and characterization of high-risk plaques vulnerable for rupture. For this work, we focus on preclinical validation of our IVPA-US imaging system. Our approach towards validation includes systematic comparison of IVPA-US imaging to gold-standard histopathology, and previously validated imaging modalities such as angiography, grayscale IVUS, and NIRS-IVUS. Our investigation ranges from *ex vivo* interrogation of atherosclerotic human coronary arteries to *in vivo* assessment of atherosclerotic peripheral arteries in swine models of vascular disease. The results of our steps towards validation in a heterogeneous sample set is presented in the following chapters, in which we show agreement between IVPA-US imaging, histopathology, imaging results from existing modalities, and metabolic phenotype. We further demonstrate the competing advantages of IVPA-US imaging over existing intravascular tools for localization and quantification lipid content, such as sensitivity for early atherosclerotic changes, differentiation between superficial and deep lipid, and localization of lipid cores in relation to other plaque features.

The highly interdisciplinary nature of this work required collaboration with experts in spectroscopy, optical engineering, microfabrication, materials engineering, signal processing, cardiovascular pathophysiology, and clinical cardiology. The collective work of many individuals has resulted in significant advancement towards our central hypothesis not only through comparative validation, but also, along the way, critical milestones necessary for future clinical translation. These achievements include miniaturization of the probe within a protective sheath, automated high-speed imaging with real-time display, sensitivity across a large depth through luminal blood, refined post-processing algorithms, and analysis of photoacoustic spectral characteristics. In this thesis, the aforementioned technical achievements are discussed only within the context of validation in biological samples.

2. ASSESSMENT OF EARLY ATHEROSCLEROSIS IN CAROTID ARTERIES OF DYSLIPIDEMIC OSSABAW SWINE BY IVPA-US: AN *EX VIVO* VALIDATION STUDY

2.1 Rationale

The present study aims to demonstrate the capability of an intravascular photoacoustic-ultrasound (IVPA-US) imaging catheter for depth-resolved assessment of lipid deposition in fixed and fresh carotid artery specimens from Ossabaw swine with dyslipidemia and metabolic syndrome. To that end, we compare IVPA-US imaging results to gold-standard histopathology and near-infrared spectroscopy-intravascular ultrasound (NIRS-IVUS), a previously validated and clinically-approved hybrid modality for lipid detection. We provide this comparison to establish agreement between competing modalities and also highlight the relative advantages of each. Imaging was conducted in carotid artery specimens from swine due to its large lumen diameter and muscular nature, providing unambiguous structural features on IVUS. Furthermore, we use the Ossabaw miniature swine model, as it has been previously well-characterized to develop dyslipidemia and the features of metabolic syndrome when induced with a pro-atherogenic diet [293-296]. The presence of subclinical vascular disease in Ossabaw swine provides an opportunity to investigate the sensitivity of both modalities for the detection of early-stage (or pre-clinical) atherosclerosis [280]. Portions of the work presented in this chapter have been published previously in *Scientific Reports* and have been intentionally reproduced here with permission [255].

2.2 Materials and Methods

2.2.1 IVPA-US Imaging System and Data Acquisition

A custom-built potassium titanyl phosphate (KTP)-based optical parametric oscillator (OPO) emitting at 1.7 μm with a repetition rate of 500 Hz and pulse width of 13 ns was used as the optical excitation source for photoacoustic imaging work presented in this chapter [297]. We used 1.7 μm due to the absorption peak of lipids and valley of water at this wavelength (Fig. 1.10A) [228, 266]. Although there is not a distinct difference in

absorption coefficients of lipid and water at 1.7 μm, the generated PA signal from lipid is substantially greater due to the larger Gruneisen parameter [229]. Light was coupled to the catheter via a multimode fiber (MMF) and an optical rotary joint. The pulse energy at the catheter probe tip was controlled to 120 μJ or less, corresponding to an energy density of approximately 30 mJ/cm^2 at the tissue surface, below the 1.0 J/cm^2 ANSI safety standard for skin at 1.7 μm [298]. Cross-sectional scanning and longitudinal pullback was enabled by a rotational motor, linear stage, and torque coil. Sequential IVPA and IVUS signals were generated and detected with a 10 μs time delay (37000-424 Datapulse Pulse Generator, Datapulse, Inc.) and a single-element transducer (0.5 x 0.6 x 0.2 mm^3, 42 MHz, 60% bandwidth; Blatek, Inc., Point-Claire, QC, Canada). Signals were amplified by a factor of 39 dB and acquired digitally via a data acquisition card (ATS9462 PCI express digitizer, AlazerTech, Canada) with 16-bit digitization and 180 MS/s rate to LabView software, with quasi-real-time display. The number of A-lines collected per image was 500, at a 1 frame per second (fps) imaging speed (catheter rotation of 1 revolution per second).

A collinear catheter design was used, as shown in Figure 2.1. Briefly, the distal end of the MMF fiber (FG365LEC, Thorlabs, Inc., Newton, NJ) was polished to 45^o for ultrasound wave reflection from a single-element transducer placed parallel to the fiber and facing the polished surface. Optical light delivery still propagates in a forward direction from the polished end, thus optical and ultrasound paths are collinear after encountering the polished surface. Next, a 45^o rod mirror (1 mm diameter; Edmund Optics, Inc., Barrington, NJ) reflects both paths perpendicular to the catheter axis for interrogation of the vessel wall. The total diameter of the catheter tip probe was 1.6 mm and did not include an outer protective sheath.

The IVPA-US collinear catheter system demonstrated a PA axial resolution of 81 μm and lateral resolution of 372 μm at a radial distance (i.e. depth) of 2.2 mm, as measured by a 7 μm-diameter carbon fiber in deuterium oxide (D_2O) as a standard. At greater imaging depths up to 6.2 mm, PA axial resolutions remained around 80 μm, while lateral resolutions ranged from 350 μm to 430 μm. Notably, optical and ultrasound paths in this collinear design were found to overlap at a depth of 6.2 mm. Further characterization of imaging system performance, description of the system architecture, and full fabrication method of the collinear catheter are found in detail in work previously published by our group [255].

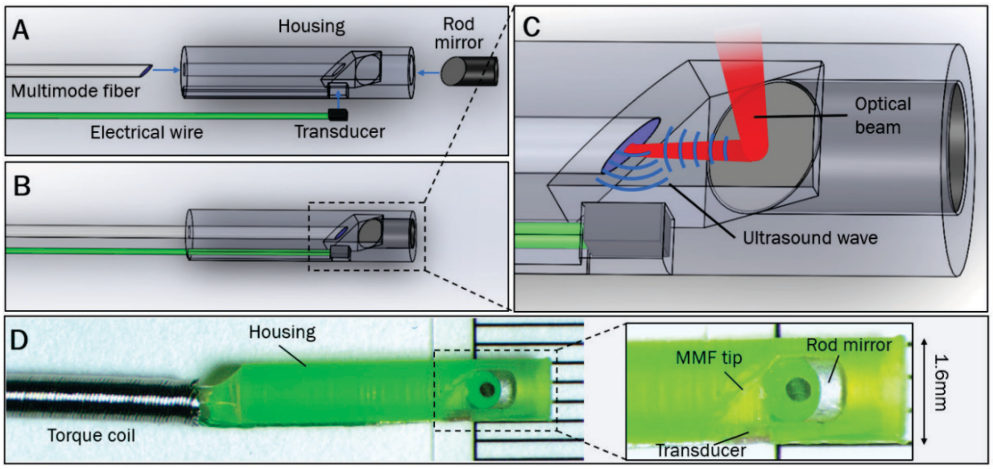

Figure 2.1. **Collinear IVPA catheter probe.** A) Exploded-view schematic of the collinear catheter. B) Assembled view of the collinear catheter. C) Zoom-in view of the catheter probe tip, illustrating collinear overlap between optical and acoustic paths after reflection of the polished multimode fiber (MMF) surface. D) Photograph of the fabricated catheter probe tip and detailed structure (inset). Reproduced from Cao et al., (*Sci Rep*, 2016).

2.2.2 Animal Care and Use

This protocol was performed according to the *Guide for the Care and Use of Laboratory Animals* and approved by the Indiana University School of Medicine Animal Care and Use Committee [299]. Ossabaw miniature swine (*n*=16) were fed a hypercaloric, atherogenic diet for 6 months (43% of total caloric intake from fat, 16% from protein, and 41% from carbohydrates, 1000 g/day). Swine were individually housed with free access to water. Development of metabolic syndrome (MetS) and pre-clinical coronary artery disease (CAD) in this naturally progressive animal model of human disease has been characterized in previous work [294, 296]. Metabolic data including body weight, total cholesterol, triglycerides, fasting glucose, and blood pressure were collected to confirm induction of MetS and dyslipidemia in the animals. A carotid artery specimen that we investigated after formalin-fixation was harvested from a swine in a different study, in which diet composition and duration varied slightly (fed for 12 months, 600 g/day with the addition of 19% kcal from fructose, supplemented with cholesterol (2%), hydrogenated coconut oil (5%), hydrogenated soybean oil (8%), cholate (1%) and high-fructose corn syrup (5%) by weight; KT-324, Purina Test Diet, Richmond, IN).

Anesthesia was induced via intramuscular injection of 5.5 mg/kg telazol (Webster Veterinary, Devens, MA) and 2.2 mg/kg xylazine (Fort Dodge Animal Health, Fort Dodge,

IA). Next, pigs were intubated and maintained with 2-4% isoflurane mixed with 100% oxygen. The isoflurane level was adjusted during the *in vivo* procedure to maintain stable hemodynamics. A 7 Fr introducer sheath was inserted in the right femoral artery of the swine and heparin was administered (200 U/kg). Next, a 7 Fr guiding catheter (Cordis, Bridgewater, NJ) was advanced to access the carotid artery bifurcation. An angiogram with Omnipaque contrast (iohexol) was recorded to visualize carotid vascular anatomy. Next, a 3.2 Fr, 45 MHz commercial IVUS catheter (Revolution, Volcano, Corp., Rancho Cordova, CA) was advanced 90 mm distally over a percutaneous transluminal coronary angioplasty guidewire (Boston Scientific, Natick, MA) into the right carotid artery. Automated IVUS pullback was performed and recorded at 0.5 mm/s. *In vivo* IVUS imaging was not performed for the carotid artery specimen that we investigated after formalin-fixation. Following imaging, the animal was euthanatized by isoflurane overdose and cardiectomy.

Following euthanasia, the carotid artery bifurcation was isolated and dissected out of the animal for further removal of surrounding adventitia. The bifurcation branch point was cannulated with a shortened 8 Fr hemostatic introducer sheath and sutured securely. Next, the distal ends of the left and right carotid artery and the right subclavian artery side branch were ligated with suture (3-0 black braided silk, Ethicon, Inc., Somerville, NJ) to allow for pressure-perfusion. Arteries were maintained in Eagle's Minimal Essential Medium with HEPES (EH) storage solution at 4 ^{o}C and imaged within 96 hours after death. A separate carotid artery specimen was formalin-fixed in 10% phosphate-buffered formalin for 24 to 48 hours, then grossly sectioned into 3 to 4 mm segments. A segment of interest, with suspected plaque on stereo microscope imaging, was placed in 2.5% agarose gel surrounding the artery and submerged in D_2O for imaging.

2.2.3 *Ex Vivo* Imaging and Histology

For carotid arteries imaged fresh, the vessel was pinned in a Sylgard® 184 Silicone Elastomer (Dow Corning, Corp., Midland, MI) tray and submerged in 1X phosphate-buffered saline (PBS), pH 7.4 (Life Technologies, Carlsbad, CA) at room temperature and was perfused to mimic physiologic pressure during imaging. Perfusion was performed manually with a large-barrel syringe at an approximate rate of 100 to 140 mL/min, which translates to an approximate pressure of 80 to 120 mmHg, as measured experimentally

using a coronary pressure wire (ComboWire XT, Volcano, Corp.). A 3.2 Fr, 45 MHz IVUS catheter (Revolution, Volcano, Corp.) was introduced into the carotid artery via hemostatic introducer sheath and advanced to a maximal distal point, where the artery was ligated (Fig. 2.2). The vessel was perfused as described during an automated pullback at 1.0 mm/s and imaging speed of 30 fps. Pullback was complete when the imaging catheter retreated into the introducer sheath. This procedure was repeated with a 3.2 Fr, 40 MHz NIRS-IVUS catheter (TVC Insight, Infraredx, Inc., Burlington, MA) at a 0.5 mm/s pullback speed and 16 fps imaging speed. Lastly, the procedure was repeated using our 4.8 Fr, 42 MHz IVPA-US collinear catheter at a pullback speed of 0.2 mm/s and 1 fps imaging speed. Pressure-perfusion was not performed for IVPA-US *ex vivo* imaging procedures, due to the lack of a surrounding protective sheath and the need for a modified guiding catheter to permit resistance-free pullback through the introducer sheath. Alignment of pullbacks from different modalities was conducted via identification of common anatomical landmarks, such as the right subclavian artery branch and the carotid bifurcation. The fixed carotid artery specimen embedded in agarose gel was imaged by our IVPA-US imaging system in a static D_2O environment at several cross-sectional locations within the segment, rather than a continuous pullback. *Ex vivo* grayscale IVUS and NIRS-IVUS imaging were not performed in this specimen.

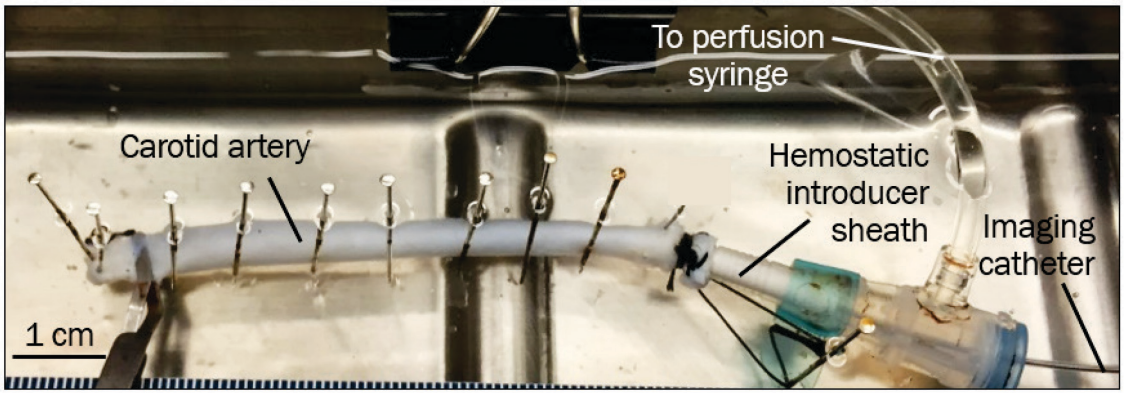

Figure 2.2. ***Ex vivo* imaging setup for fresh carotid artery imaging.** Carotid arteries are cannulated with a modified hemostatic introducer sheath. Distal ends and side branches are ligated (shown here with a hemostatic clip) to allow for physiologic pressure perfusion during imaging.

To maintain vessel morphology, fresh carotid arteries were pressure-fixed using 10% phosphate-buffered formalin with a large-barrel syringe at approximately 25 mL/min for 30 min and placed in formalin for 24 to 48 hours. The arteries were grossly sectioned in 3

to 5 mm segments. Next, each segment was paraffin embedded, thin sectioned, and stained for hematoxylin and eosin (H&E) and Russel-Movat's pentachrome. For segments identified as positive of region interests on NIRS-IVUS imaging and IVPA-US imaging, multiple thin sections were cut serially at 250 μm intervals. The carotid artery specimen that was imaged after formalin-fixation was cryoprotected in a 25% sucrose/PBS wash for 48 hours, after which the tissue was cryosectioned and stained with oil red O and H&E counterstain. Area calculations on intravascular and histology images were performed using ImageJ software (1.48v, National Institutes of Health, USA).

2.3 Results

2.3.1 IVPA-US Imaging of a Fixed Carotid Artery from an Ossabaw Swine

Ossabaw swine from which the right carotid artery was harvested for imaging had a 91.4% increase in total body weight from the start of hypercaloric atherogenic diet to sacrifice (52.5 kg to 100.5 kg). The swine, however, did not have elevated plasma lipids (total cholesterol: 63 mg/dL, triglycerides: 89 mg/dL). Despite a lipid panel within normal limits, we observed suspected stenotic plaque under a stereoscopic microscope in a segment of the carotid artery. After formalin-fixation and being embedded in agarose gel, we performed IVPA-US imaging of the segment of interest. IVUS, IVPA, and merged cross-sectional images are shown in Figure 2.3A-C. On IVUS imaging (Fig. 2.3A), we observed the characteristic three-layer appearance of the muscular carotid artery. We used the intimal border to identify the original lumen, which then revealed an area of strong echogenicity suggesting the presence of an eccentric fibrous plaque. On IVPA and merged imaging (Fig. 2.3B-C), we found the suspected plaque area had strong PA signal, suggesting the presence of a lipid-rich core. On gross imaging of the embedded artery (Fig. 2.3D) and ORO histology (Fig. 2.3E), we confirm the presence of an eccentric fibrofatty plaque. There is some ambiguity on the ORO histological section, as we do not see the characteristic red color specific for lipid. Instead, there is a tear where we would suspect lipid to be. This is a histological artifact of cryosectioning heterogeneous arteries with soft plaque components that make for a poor cutting substrate on the cryotome.

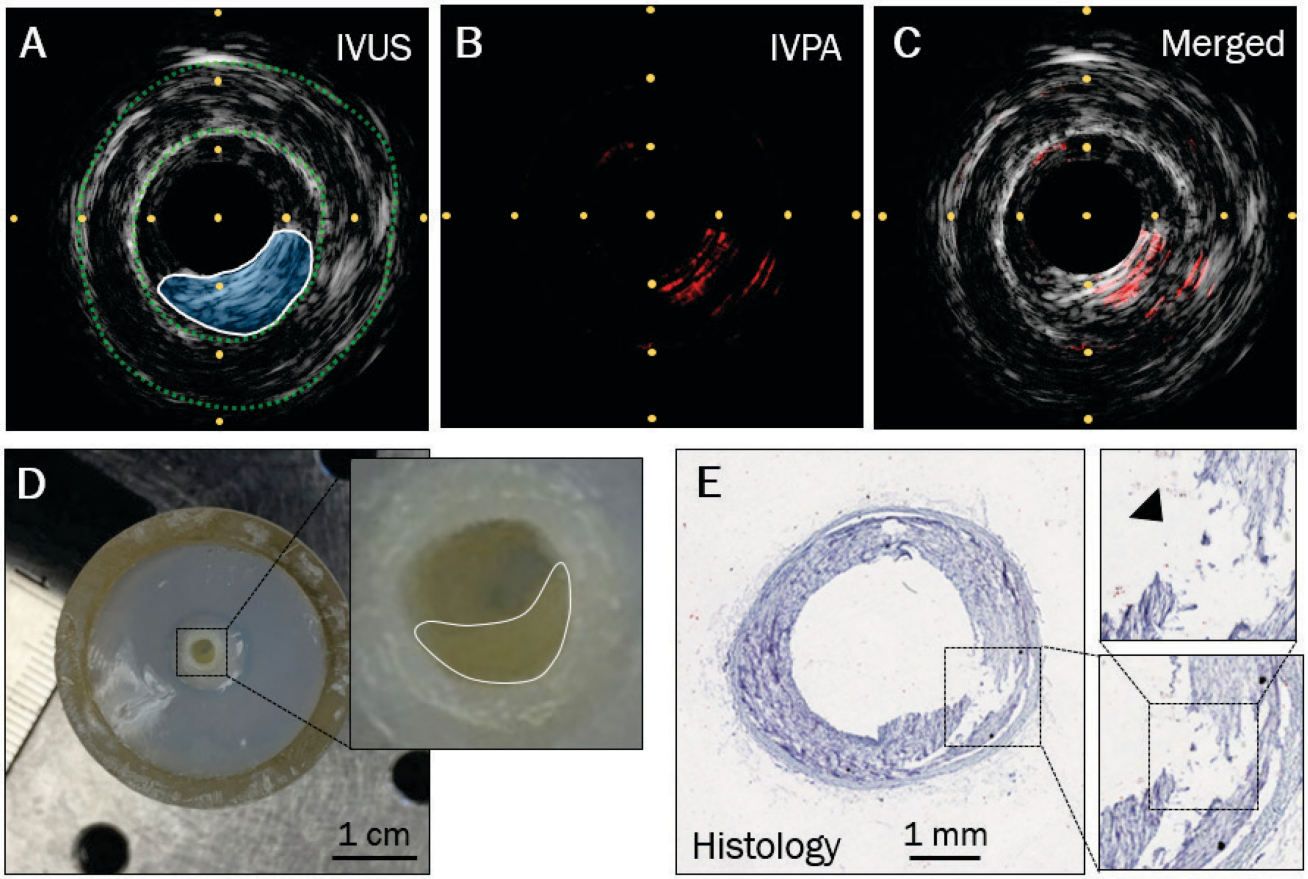

Figure 2.3. ***Ex vivo*** **IVPA-US imaging of a swine carotid artery.** A) IVUS cross-sectional image, with internal elastic lamina and external elastic lamina borders of the characteristic three-layer appearance traced (green). A suspected eccentric plaque encroaching the lumen is highlighted (blue). B) IVPA image showing lipid (red). C) Merged IVPA-US image shows a strong area of PA signal within the suspected plaque region, suggesting a lipid-rich core. D) Gross photograph of artery segment with the stenotic plaque traced (inset). E) ORO histology showing possible presence of lipid (insets, arrowhead). Horizontal and vertical axis tracings in A-C are 1 mm apart. Reproduced from Cao et al., (*Sci Rep*, 2016).

2.3.2 Comparative IVPA-US and NIRS-IVUS Imaging of Fresh Carotid Arteries from Ossabaw Swine with Metabolic Syndrome

Ossabaw swine from which we imaged fresh carotid arteries by angiography, *in vivo* and *ex vivo* grayscale IVUS, *ex vivo* NIRS-IVUS, and *ex vivo* IVPA-US exhibited the features of MetS, including glucose intolerance, obesity, and dyslipidemia (total cholesterol: 907 ± 180 mg/dL, triglycerides: 261 ± 137 mg/dL). For alignment across all intravascular imaging modalities, we relied upon the anatomical landmarks of the carotid bifurcation and the subclavian artery branch. In the 15 of 16 carotid arteries, we were unable to perform comparative analysis due to either inadequate anatomical alignment of pullbacks or no positive region of interest with suspected lipid. In the remaining sample, we successfully identified anatomical landmarks on all modalities and also established a positive region of interest (Fig. 2.4) with suspected lipid deposition based on NIRS-IVUS findings. In this carotid artery sample, the swine had a total cholesterol of 600 mg/dL, triglycerides of 16 mg/dL, and weight of 70.8 kg at sacrifice (153% increase during atherogenic diet period).

Angiography with contrast of the carotid artery bifurcation showed a non-obstructed lumen (Fig. 2.5A). Grayscale IVUS imaging of the right carotid artery did not reveal any vascular disease, both *in vivo* (Fig. 2.5B) and *ex vivo* (Fig. 2.6A). *Ex vivo* NIRS-IVUS imaging of the right carotid artery showed high probability of lipid at the carotid bifurcation point (Fig. 2.6B), with a $maxLCBI_{4mm}$ of 620 distal to the bifurcation and 469 proximal to the bifurcation (Fig. 2.7). On *ex vivo* IVPA-US imaging, we also detected lipid signal proximal to the carotid bifurcation point, as possible raised lesion with an estimated area of 0.62 mm^2 (Fig. 2.6C, D). Furthermore, we repeated imaging within this segment (0.9 mm) at a slower pullback speed of 0.09 mm/s for high-resolution 3D reconstruction which confirmed our findings and showed the lesion as a continuous streak (Fig 2.8). On histopathology of this positive region of interest (proximal to the carotid bifurcation and distal to the right subclavian artery branch), we observed a raised lesion with an area of 0.70 mm^2. Based on the paucity of extracellular structure and anucleate space of the lesion, we characterized the lesion as early pathologic intimal thickening (Fig. 2.6E, F) [300]. A distal portion of the artery as shown in Figure 2.4 served as a negative control, as no disease or lipid deposition was observed all modalities. Histology confirmed healthy artery morphology. (Fig. 2.9).

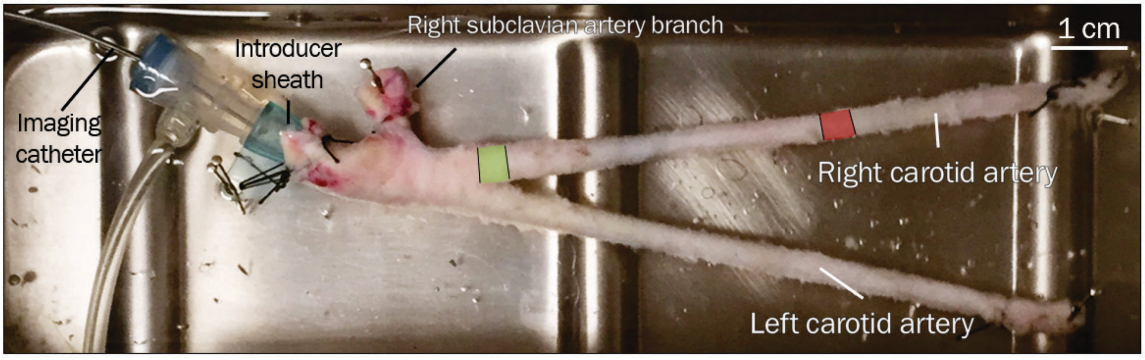

Figure 2.4. **Gross image of a fresh carotid artery.** Gross image of the fresh carotid artery sample in which we identified, by multiple modalities, a positive region of interest (highlighted green) immediately proximal to the carotid bifurcation and a negative region of interest (highlighted red) in the distal portion of the artery.

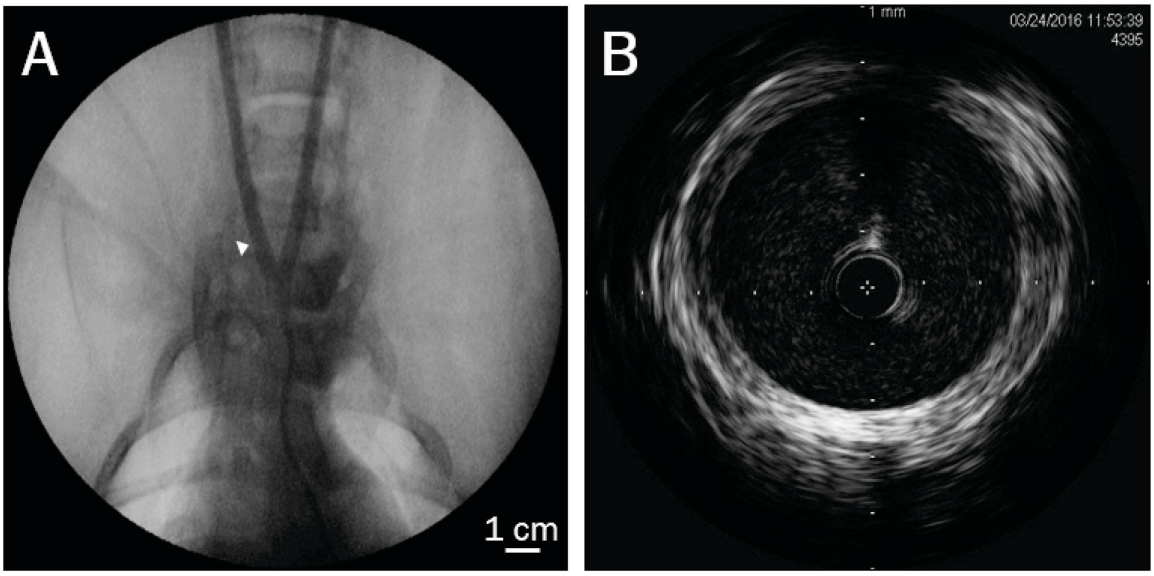

Figure 2.5. ***In vivo*** **angiogram and grayscale IVUS imaging.** A) Angiogram of the carotid artery bifurcation, showing no stenotic lesions. B) Grayscale IVUS cross-sectional frame, showing a three-layer appearance and no disease. The relative position of this frame in the carotid artery is indicated in (A) by an arrowhead.

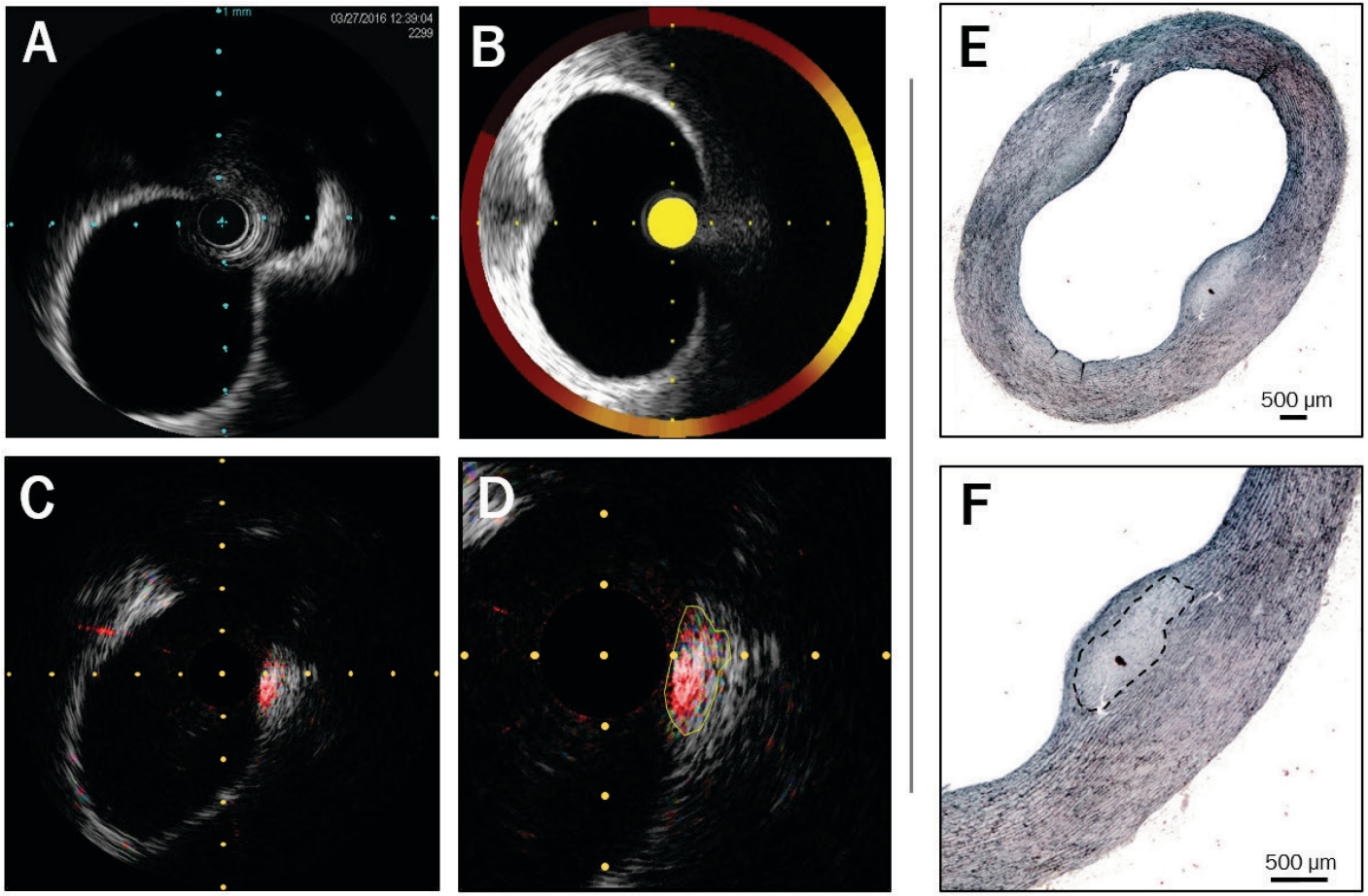

Figure 2.6. ***Ex vivo*** **imaging frames and histopathology of identical cross-sections at the positive region of interest, proximal to the carotid bifurcation.** We identified identical position on all imaging and histological sections based on the bifurcate anatomy. A) On grayscale IVUS, we did not observe any disease. B) On NIRS-IVUS, we observed a high probability of lipid (yellow) at approximately 2 to 4 o'clock. C) Merged IVPA-US image shows lipid (red) on the intimal surface. D) We calculated the area with strong lipid signal on IVPA as 0.62 mm^2. E, F) Movat's pentachrome stained section, showing a raise lesion (traced) with a lesion area of 0.70 mm^2.

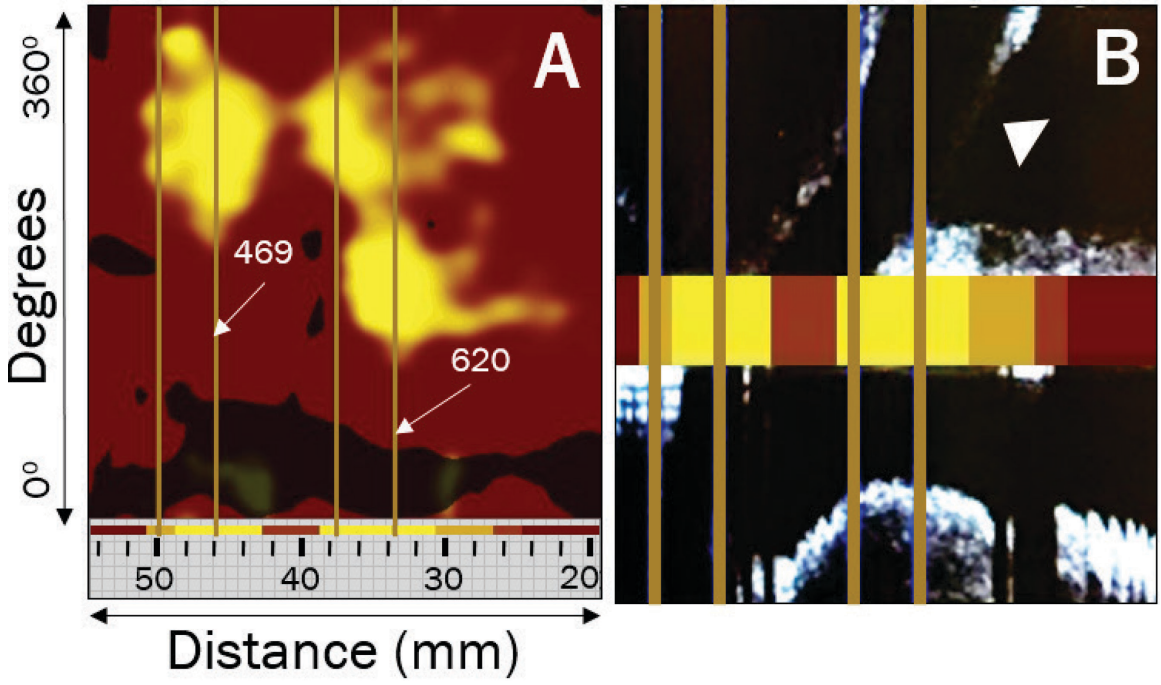

Figure 2.7. **NIRS chemogram at the positive region of interest, proximal to the carotid bifurcation.** A) The 2D chemogram shows the positive region interest as having a high probability of lipid. The maxLCBI$_{4mm}$ were calculated for two regions (outlined in gold), distal to the bifurcation (620) and proximal to the bifurcation (469). Also shown is the block chemogram above the *x*-axis scale, which summarizes the total chemogram into 2-mm colorized blocks representing the probability of lipid into four distinct colors from red (low) through orange and tan to yellow (high). B) NIRS block chemogram in relation to the longitudinal grayscale IVUS image. The regions within which the maxLCBI$_{4mm}$ were calculated are outlined in gold and the left carotid artery is indicated by an arrowhead.

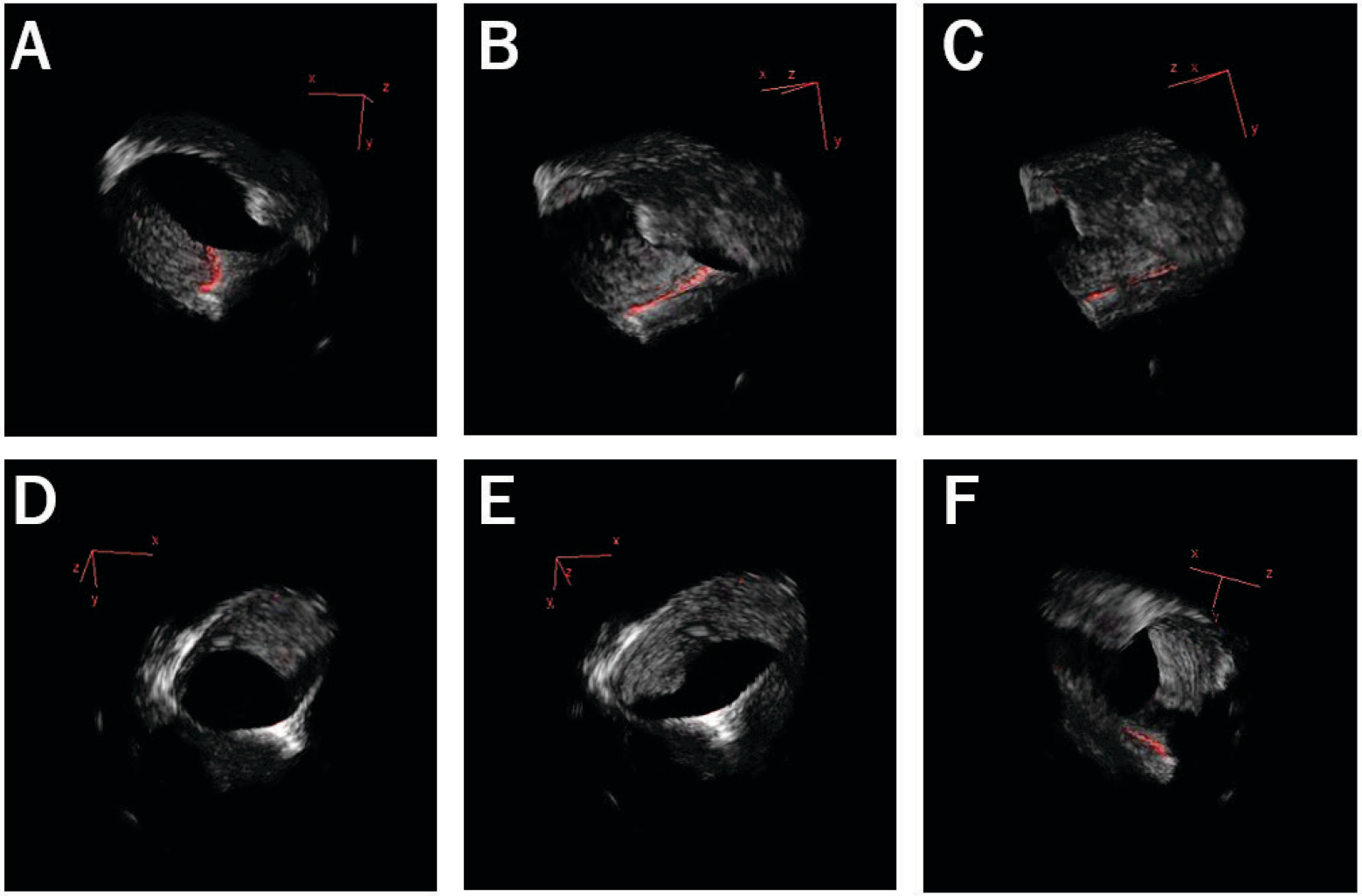

Figure 2.8. **3D reconstruction of the positive region of interest.** Lipid deposition, as a continuous streak, is visible (red) in this merged 3D reconstruction of a 0.9 mm segment. (A-F) Panels advance in a clockwise rotation, showing lipid deposition in relation to the bifurcation, which is best visualized in panels B and E.

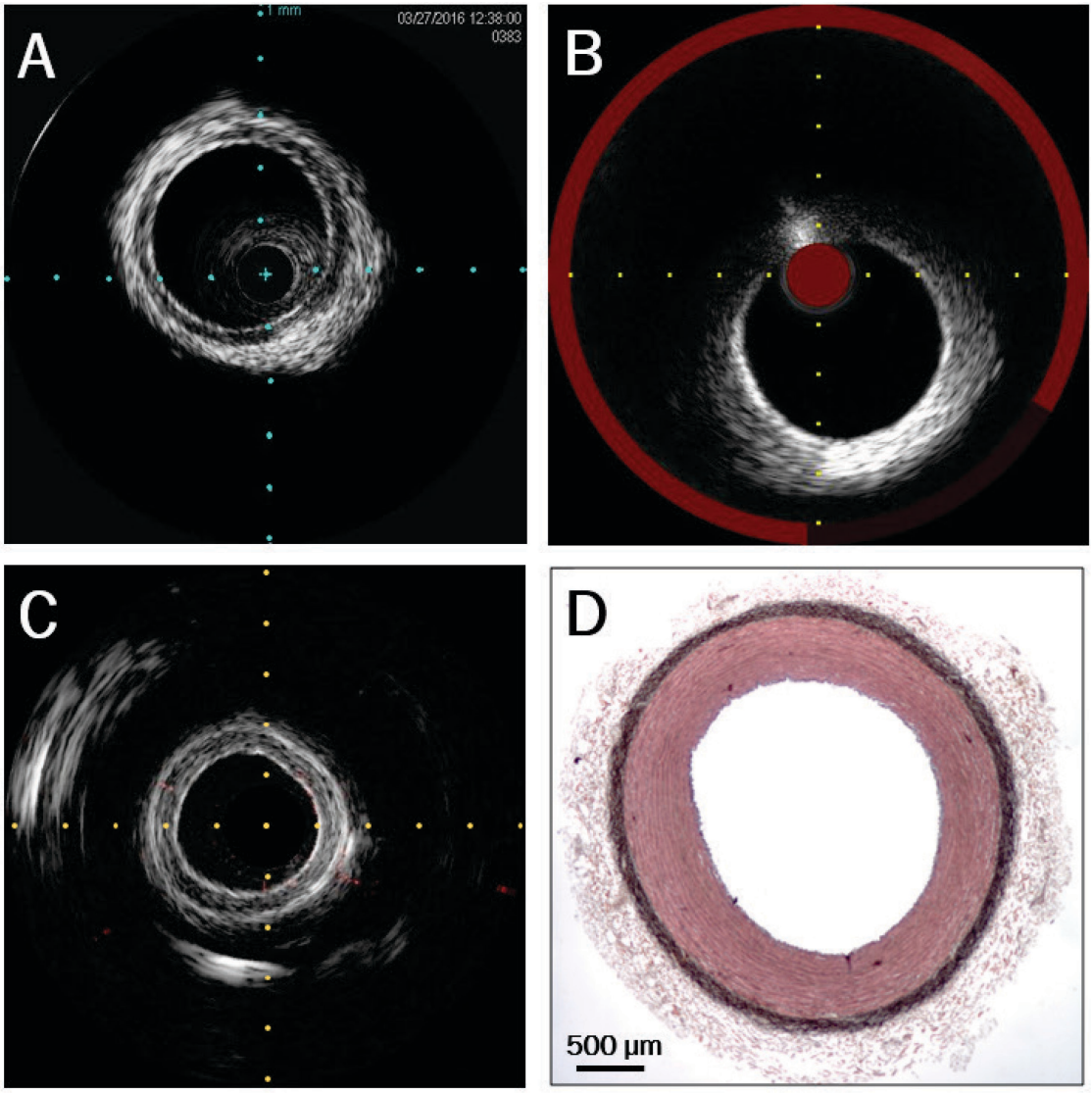

Figure 2.9. ***Ex vivo*** **imaging frames and histopathology of identical cross-sections at the approximate negative region of interest.** A) On grayscale IVUS, we did not observe any disease. B) On NIRS-IVUS, we did not detect any presence of lipid. C) On IVPA-US image (merged shown) we did not observe and lipid signal. D) We calculated the area with strong lipid signal on IVPA as 0.62 mm^2. E, F) Movat's pentachrome stained section, showing healthy artery morphology.

2.4 Discussion

In this study, we have shown that our IVPA-US imaging system and collinear catheter design is capable of depth-resolved assessment of lipid content in both fixed and fresh carotid arteries from Ossabaw swine on atherogenic diet. On IVPA-US imaging of the fixed carotid artery specimen, we found strong and unambiguous lipid signal on the PA channel within the borders of the internal elastic lamina, as identified on the US channel.

It is only by virtue of the depth resolution and uniform overlap of two modalities that we were able to localize the lipid core. Our imaging results provided us with sufficient structural (i.e. fibrous and eccentric by US channel) and compositional (i.e lipid by PA channel) information to posit the observed plaque to be a fibrofatty phenotype [23]. We, however, were not able to conclude this lipid-rich plaque phenotype definitively. The main limitation in the investigation of this sample was the ambiguity in of the ORO stained histology, in which there was an artifact due to tissue tearing [301]. While this is common when cryosectioning soft lipid-laden plaques, it is not acceptable for device validation. Despite this overarching limitation in this data set, it provided us invaluable data for proof-of-concept capability of our platform. Just as vital was the feedback from this investigation in refinement of our fresh carotid artery imaging protocol.

In our fresh carotid artery imaging experiments, we performed the first comparison to commercially available intravascular tools, including NIRS-IVUS which is the only clinically-approved dual-modality catheter for lipid detection. On traditional angiography and grayscale IVUS imaging, the early atherosclerotic changes present in the Ossabaw swine were unidentifiable and assumed to be disease-free—a gross misclassification. It was only with the addition of a second modality to IVUS that we were able to observe pathology at the carotid bifurcation, confirming the value of hybrid imaging [58, 273]. This site of disease development is in accordance with our understanding that atherosclerosis often develops preferentially at branch points with turbulent flow [302-305]. We found that our IVPA-US imaging catheter produces comparable results to NIRS-IVUS. The agreement between the modalities is nontrivial, particularly because NIRS-IVUS imaging has been exhaustively validated for lipid detection previously [108, 110, 205, 292]. Furthermore, comparison of the results from both modalities to gold-standard histopathology suggests that IVPA-US results correlate better than NIRS-IVUS results. As IVPA-US imaging provides the depth-resolution lacking in NIRS-IVUS, we were able to quantify the cross-sectional lipid core area, which agreed with the area calculated on histology (0.62 mm^2 vs. 0.70 mm^2). Additionally, we localized the lipid core as superficial, confirmed by histology. Conversely, NIRS-IVUS imaging overestimated lipid deposition at the positive region of interest, showing high probability of lipid spatially distributed from 2 to 4 o'clock and a very high $maxLCBI_{4mm}$ of 469. This disagreement with histology

further illustrates the need for depth-resolved lipid core imaging and head-to-head comparative study.

The major limitation in this investigation was the limited sample size. Although we imaged 16 carotid arteries, 15 data sets were not useable. This was due to either inability to identify anatomic landmarks on US for alignment of modalities or lack of any lipid-positive regions of interest. We hypothesize that the low levels of disease may be attributed to the young age that animals were started on their diet (approximately 6 months) during which time they are more resistant to vascular changes, even in the presence of elevated cholesterol [306]. Nonetheless, this provided samples in which we were able to exhibit sensitivity for pre-clinical levels of lipid content. Furthermore, we acknowledge that US resolution of our collinear catheter was limited in deep-field, attributed to the multiple reflection surfaces in the design. While this did not affect interpretation of the vessel wall in which three-layer appearance was identifiable, deep-field structures such as branches were difficult to identify consistently. Lastly, our IVPA-US imaging catheter lacked a protective sheath, precluding us from performing pressure-perfused imaging. In NIRS-IVUS, we did perform pressure-perfused imaging with PBS. However, the automated analysis algorithms are optimized for imaging through blood which attenuates spectroscopic signal, which may explain some overestimation by this modality [108, 197]. In the future, we intend to extend our study to include a robust data set of plaque phenotypes form early to advanced lesions.

2.5 Conclusions and Outlook

Taken together, we have shown proof-of-concept demonstration of our IVPA-US imaging catheter system and collinear catheter design for lipid content detection in a fixed carotid artery with atherosclerotic disease. Furthermore, we have shown validation of our catheter-based system for additional depth-resolved detection and quantification of preclinical atherosclerosis in a fresh carotid artery. This was conducted via systematic comparison to gold-standard histopathology and NIRS-IVUS at identical artery segments. Furthermore, without the additional information gained from a lipid-specific modality, one could perceive this artery from a dyslipidemic swine as disease-free with the use of grayscale IVUS alone – a gross misclassification.

Ultimately, lipid-specific imaging with depth resolution will advance understanding of the pathogenesis and prevalence of vulnerable plaque rupture and development of preventative and interventional therapies [55]. Particularly, quantitative localization of early atherosclerosis will permit longitudinal studies to monitor progression to the most vulnerable plaque phenotype: TCFA [58, 59, 272, 273]. We currently do not know the prevalence of TCFAs in the general population and precisely how prone to rupture and subsequent MACE they are [275, 288]. Despite the advances made, our understanding of plaque rupture and progression to ACS is primarily based on post-mortem studies from the late 1990s to early 2000s [21, 33, 40, 286, 307]. The only *in vivo* evidence we have is from the PROSPECT study, which reported only 4.4% of TCFAs, as defined by VH-IVUS, caused MACE during 3.4-year follow-up period. This is low, especially considering the study enrollees were already high-risk patients [100]. This observation and lack of sound evidence supporting the vulnerable plaque hypothesis has led to recent challenges to the concept [276, 280, 284-287, 308, 309]. However, this challenge to vulnerable plaque hypothesis and imaging is contentious, as the absence of evidence primarily stems from the lack of a valid *in vivo* modality to study this process in the general population. With depth-resolved localization of lipid-rich necrotic cores, a hallmark of TCFAs, IVPA-US imaging has the potential to provide powerful information in filling this void.

3. ASSESSMENT OF LIPID CORE PLAQUES IN HUMAN CORONARY ARTERIES: AN *EX VIVO* VALIDATION STUDY

3.1 Rationale

The present study aims to demonstrate the capability of real-time intravascular photoacoustic-ultrasound (IVPA-US) imaging catheter for depth-resolved assessment of lipid core plaques in fixed and fresh coronary artery specimens from post-mortem and explanted human hearts. Similar to our previous study in a swine model, we compare IVPA-US imaging results to gold-standard histopathology and near-infrared spectroscopy-intravascular ultrasound (NIRS-IVUS), in order to establish agreement between competing modalities and also highlight the relative advantages of each. Although large animal models can provide the advantage of systematic control of vascular pathology, it remains difficult recapitulate the advanced and complex atheromatous plaques of humans [310-314]. Development of humanlike lesions have been shown to be possible, but require significant and long-term infrastructure (e.g. financial and personnel) towards animal maintenance for genetic or diet-induced disease, which still is not always predictable in terms of location and severity [147, 315]. Thus, the *ex vivo* interrogation of fresh, atherosclerotic human coronary arteries is imperative in evaluating the capability to detect lesions that resemble what is encountered in clinical practice. Portions of the work presented in this chapter have been published previously in *Scientific Reports* or under review for publication, and have been intentionally reproduced here with permission [254, 316].

3.2 Materials and Methods

3.2.1 IVPA-US Imaging System and Data Acquisition

A Nd:YAG pumped OPO (Nanjing Institute of Advanced Laser Technology) emitting at a wavelength of 1730 nm, pulse width of 10-11 ns, and repetition rate of 2 kHz was used as the optical excitation source for photoacoustic imaging work presented in this chapter. Light was coupled to the catheter via a multimode fiber (MMF) (FG365LEC, Thorlabs, Inc.) and a custom-built fiber-optical rotary joint, which allowed for efficient optical

coupling and radiofrequency signal transmission at high rotational speeds. The pulse energy at the catheter probe tip was controlled to 80-100 μJ, corresponding to an energy density of approximately 40-50 mJ/cm^2 at the tissue surface, below the 1.0 J/cm^2 ANSI safety standard for skin at 1.7 μm [298]. Video-rate rotational imaging and longitudinal pullback were enabled by a rotatory step motor (X-NMS17C-E01, Zaber Technologies, Inc., Vancouver, BC) and linear stage (X-LRM100A, Zaber Tchnologies, Inc.) Sequential IVPA and IVUS signals were generated and detected with a 5-8 μs time delay (Model 9512, Quantum Composers, Inc., Bozeman, MT) and a single-element transducer (0.5 x 0.6 x 0.2 mm^3, 42 MHz, 50% bandwidth; Blatek, Inc.). Signals were amplified by a factor of 39 dB and acquired digitally via a data acquisition card (ATS9350 PCI express digitizer, AlazerTech) with 12-bit digitization , 500 MS/s sampling rate, and data throughput of 1600 MB/s. The digitized data was processed and displayed in real-time by the computer with LabView-based algorithm (LabVIEW, National Instruments, Austin, TX) and intuitive graphic user interface. A differentiated A-line strategy was used, in which there is a mismatch between the A-lines collected for IVPA and IVUS. This novel strategy overcomes the main limitation to high-speed IVPA-US imaging: laser pulse repetition rate. In this strategy, A-lines are reciprocal with imaging speed and A-lines per IVUS images two times that of IVPA images. In this work, we present data collected at 16 fps (IVUS: 250 A-lines, IVPA: 125 A-lines) and 4 fps (IVUS: 1000 A-lines, IVPA: 500 A-lines). All components of this system were installed on a single cart and made portable. Further characterization of imaging system performance, description of the system architecture, and differentiated A-line strategy are found in detail in work previously published by our group [254].

In this work, we used two catheter designs: collinear and quasi-collinear. Collinear catheter design was the similar as described previously in Chapter 2.2.1, with the key difference being an overall smaller catheter diameter of 1 mm. This was possible by use of a smaller rod mirror (diameter: 365 μm), fabricated from MMF polished to 45^o and coated with gold to provide 99% optical reflection and damage threshold up to 1 J/cm^2. The catheter housing was 3D printed (Proto Labs, Inc., Maple Plain, MN) with micro-resolution stereolithography and maintained alignment of components. This design was used for fixed artery imaging and was not enclosed in a sheath.

For fresh artery imaging, we use a quasi-collinear catheter design that varied slightly from the design presented in Chapter 2.2.1 and above. In this design, the MMF was not polished to 45°. Instead, acoustic delivery was directed to the artery wall without any reflection via tilting of the US transducer at a 10° angle. This angle maximized the overlap between acoustic and optical paths over an estimated depth of 0.6-6 mm, calculated by geometrical calculation that assumed a 6° divergence angle for the optical beam and 3° for the US wave. This design was enclosed in a protective polyurethane sheath (outer diameter: 1.6 mm), due to its low optical absorption at 1.7 μm and low acoustic impedance. The IVPA-US quasi-collinear catheter system demonstrated axial resolution from 85-100 μm and lateral resolution 170-450 μm from at depths ranging from 1.4-4.6 mm, as measured by a 7 μm-diameter carbon fiber in deuterium oxide (D_2O) as a standard. The portable IVPA-US imaging system and catheter designs are summarized in Figure 3.1.

3.2.2 Human Tissue Recovery and Preparation

Fresh human hearts were recovered post-mortem or from individuals undergoing transplant surgery, within 24 hours of death or explant. Arteries were maintained in EH storage solution at 4 ºC and imaged within 48 hours of tissue recovery. The right coronary artery was excised, retaining one inch of surrounding myocardium to maintain vessel structure. The ostium was cannulated with a shortened 6-8 Fr introducer sheath and side branches and the distal end of the artery were ligated with suture for pressure-perfusion. For the artery imaged after fixation, 10% formalin was used to pressure-fix the artery for 20 minutes at 25 mL/min and placed in formalin for 24 to 48 hours. For the artery imaged fresh, perfusion and artery anatomy were observed by *ex vivo* angiography with contrast. This protocol was approved by the Indiana University School of Medicine Institutional Review Board by exemption.

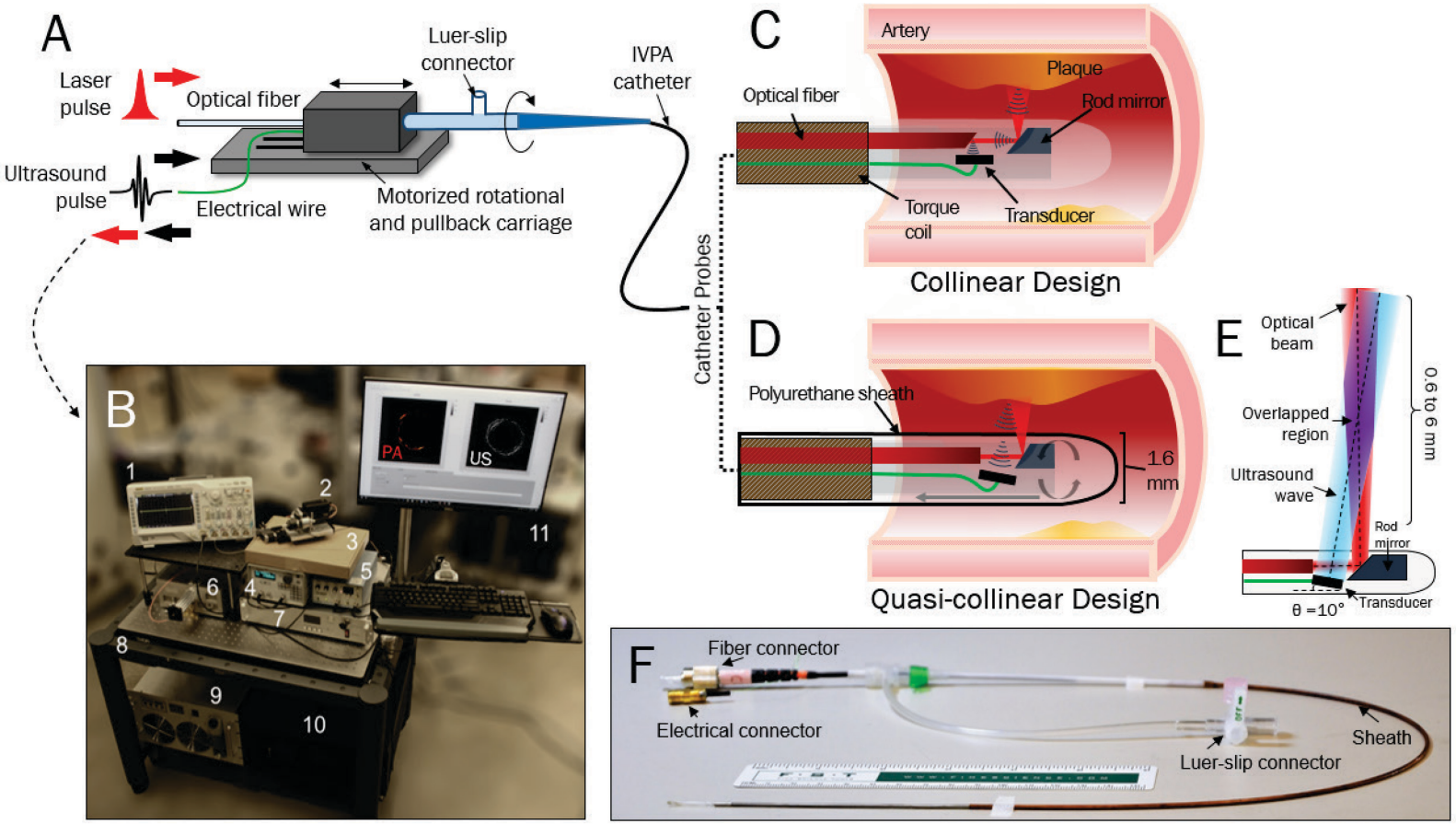

Figure 3.1. **IVPA system architecture and catheter designs.** A) Schematic of the IVPA system. Optical and acoustic pulses are delivered via multimode fiber and electrical wire. Generated signals are acquired and display in real-time on a computer. Rotational and linear translational are enabled by a motorized carriage system. The catheter sheath is flushed via Luer-slip connector. B) Image of the portable system. Major components: 1, oscilloscope; 2, fiber-optic rotary joint; 3, IVPA-US catheter; 4, delay generator; 5, US pulser/receiver; 6, Laser source; 7, Laser controller; 8, Mobile cart; 9, Laser chiller; 10, PC and DAQ card; 11, Monitor. C) Collinear catheter design, used without a sheath for fixed human coronary artery imaging. D, E) Quasi-collinear design, in which angling of the transducer and reduction of reflection surfaces maintained optical and acoustic co-registration and improved US resolution. This design was used for fresh human coronary artery imaging with a polyurethane sheath. F) Photograph of the IVPA-US catheter, with sheath. Adapted from Hui et al. (*Sci Rep,* 2017) and Cao et al. (*Sci Rep*, 2018).

3.2.3 *Ex Vivo* Imaging and Histology

The coronary artery imaged fresh was pinned in a Sylgard® 184 Silicone Elastomer (Dow Corning, Corp.) tray and submerged in 1X PBS at room temperature and was perfused to physiologic pressures during imaging. A 3.2 Fr, 40 MHz NIRS-IVUS catheter (TVC Insight, Infraredx, Inc.) was introduced into the coronary artery via hemostatic introducer sheath and advanced to a maximal distal point, where the artery was ligated (approximately 70 mm distal to the introducer sheath). The vessel was perfused during an automated pullback at 0.5 mm/s and imaging speed of 16 fps. Pullback was complete when the imaging catheter retreated into the introducer sheath. The procedure was repeated using our 4.8 Fr, 42 MHz IVPA-US quasi-collinear catheter with sheath, flushed with D_2O, at a pullback speed of 0.25 mm/s and 4 fps imaging speed. Alignment of pullbacks from different modalities was conducted via identification of fiduciary branch points and the introducer sheath, with angiographic aid.

Imaging of the fixed coronary artery specimen followed a similar protocol, with the following alterations. IVPA-US imaging was performed using a collinear catheter without a surrounding sheath. We did not pressure-perfuse the vessel during imaging due to the lack of sheath and maintenance of vessel structure after pressure-fixation. No NIRS-IVUS imaging was performed, due to inability to advance the catheter into the vessel. The artery was pinned in a Sylgard tray and submerged in D_2O. Next, our IVPA-US catheter was advanced distally to a point of resistance (due to tortuous anatomy and rigid structure after fixation). We performed an automated pullback at 0.2 mm/s and 1 fps imaging speed of the entire segment. Next, we identified a positive region of interest (an area with strong signal in the IVPA channel) and repeated imaging at this location at 16 fps. This region was marked with suture for accurate histological sectioning.

The fresh coronary artery were pressure-fixed using 10% formalin with a large-barrel syringe at approximately 25 mL/min for 30 min and placed in formalin for >24 hours. Fixed arteries were then grossly sectioned in 2.5 to 4 mm segments. Next, segments were paraffin embedded, thin sectioned, and stained with H&E and Movat's pentachrome stain. For segments identified as positive of region interests, multiple thin sections were cut serially at 250 μm intervals. Lipid pools were defined as morphologically distinct empty and/or clear, granular, mostly anucleate spaces, defined as the light-microscopic

characteristics of lipid gruel [202, 300]. Lipid area was calculated using ImageJ (1.48v, National Institutes of Health, USA) software.

3.2.4 IVPA-US and NIRS-IVUS Quantitative Analysis

IVPA-US imaging data were post-processed to identify noise, and photoacoustic pixels greater than 4 times the background noise were counted per cross-sectional frame to calculate lipid area (Fig. 3.2). Pullback segments in which the introducer sheath was present were excluded from analysis. Lipid core volume was calculated per lesion within a 4-mm segment by identifying appropriate depth and angle boundaries within which pixels were counted. All lipid pixel area measurements were calculated using MATLAB software (MathWorks, Inc., Natwick MA).

The NIRS-IVUS TVC Imaging System was used to generate 2D chemograms representing probability of the presence of lipid by a yellow color, with longitudinal pullback position on the *x*-axis and circumferential position on the *y*-axis. As NIRS spectral depth is 1 mm or less, lipid area was estimated by measuring the yellow-colored regions on the chemograms via segmentation using ImageJ. The $\text{maxLCBI}_{4\text{mm}}$ was also calculated by the system.

Calcification was measured by IVUS and defined as strong echogenicity with acoustic shadowing. The total length was calculated as continuous frames in which calcification was present. Maximum arc of calcification was calculated as the largest angle of acoustic shadowing within the total length, with each ray following the acoustic shadowing and the vertex at the center of the vessel lumen [317-320]. All IVUS analysis was performed using ImageJ software.

Data are described as mean ± SEM. Statistical significance defined as $p<0.05$. Unpaired, two-tailed Student's t-tests were used as appropriate using GraphPad Prism statistical software (GraphPad Software, Inc., La Jolla, CA).

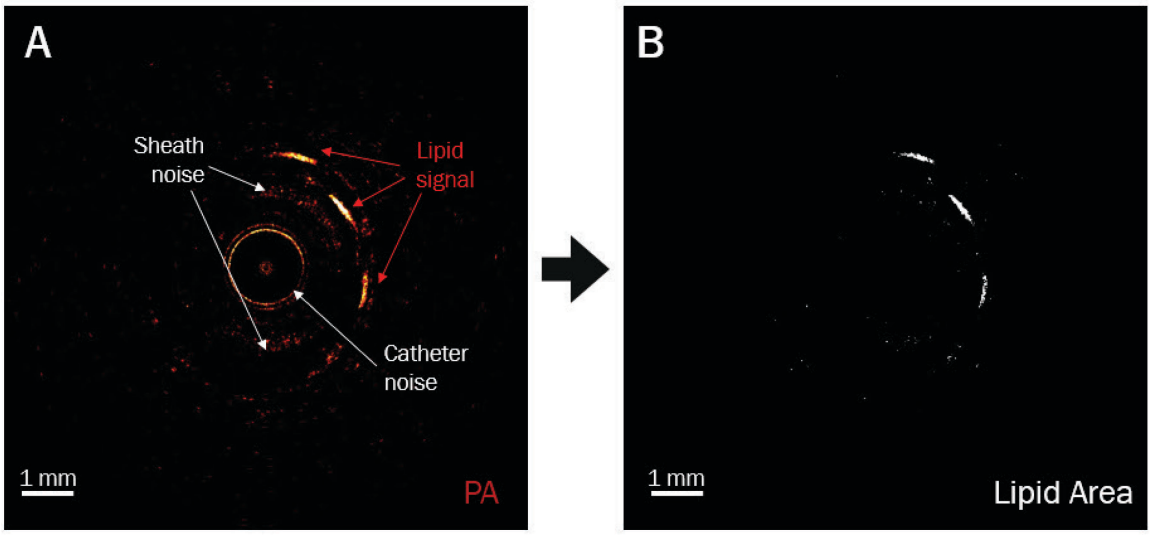

Figure 3.2. **Lipid area calculation from IVPA data.** A) Cross-sectional photoacoustic image, reconstructed from raw data with indiscriminate noise, catheter noise, and sheath noise. B) Cross-sectional binary lipid map after a threshold of 4 times the background noise level was applied (white denotes presence of lipid). The total lipid area in this example was calculated from the sum of white pixels (156.25 μm^2/pixel; total area = 0.15 mm^2).

3.3 Results

3.3.1 IVPA-US Imaging of a Fixed Human Coronary Artery

We imaged a formalin-fixed right coronary artery (RCA) from an obese 44-year old Caucasian male (BMI=32) with a past medical history of tobacco and alcohol use, hypertension, and previous MI. At the time of recovery, pericardial tamponade, left ventricular hypertrophy, and extensive valvular calcification were observed (Fig. 3.3A). The cause of death was reported as atherosclerotic hypertensive cardiovascular disease.

We performed IVPA-US imaging of the segment of interest using a collinear catheter without sheath in a D_2O environment at 16 fps imaging speed (Fig. 3.3B). IVUS, IVPA, and merged cross-sectional images are shown in Figure 3.4A-C. On IVUS (Fig. 3.4A), we observed a lesion encroaching the lumen at 1 to 3 o'clock. On IVPA (Fig. 3.4B), we identified two areas with strong PA signal at 1 to 3 o'clock and 8 o'clock, suggesting the presence of lipid-rich cores. On merged imaging (Fig. 3.4C), we used IVUS findings to localize these suspected lipid cores. The first suspected core was shown to be superficial in the eccentric lesion encroaching the lumen, with a total lipid area of 0.21 mm^2. The second suspected core was shown to be superficial, thin, and within a concentric fibrous

lesion, as evidenced by the strong echogenicity observed on IVUS [321]. The total lipid area was measured as 0.07 mm^2. On Movat's pentachrome-stained histopathology (Fig. 3.4D), we confirmed the presence of an advanced fibroatheroma with pathologic features that match imaging results. First, we observed a concentric fibroatheroma with a raised area, showing identical lumen morphology as seen on imaging. Secondly, we observed two lipid-rich necrotic cores at locations and sizes that correlate with imaging results (Fig. 3.4E-G). On histopathology, lipid-rich necrotic cores were identified as acellular areas with macrophage infiltration to the core and cap, devoid of extracellular matrix, lack of specific staining, cholesterol clefts, and an overlying fibrous cap [15, 23, 28, 41, 139]. We measured necrotic core areas of 0.59 mm^2 and 0.35 mm^2 for the lesions at 2 to 3 o'clock and 9 to 11 o'clock, respectively. Fibrous cap thickness overlying both cores were approximately 200 μm at the thinnest region. Additionally, we noted other pathologic features that indicate the advanced thick-cap fibroatheroma phenotype such as medial thinning and microcalcifications, a marker of inflammation and instability [322, 323]. Lastly, we observed intraplaque hemorrhage as another marker of vulnerability, possibly from neovascularization (Fig. 3.4H) [324, 325]. IVPA-US imaging results and corresponding histopathology were consistent with the reported past medical history of the donor.

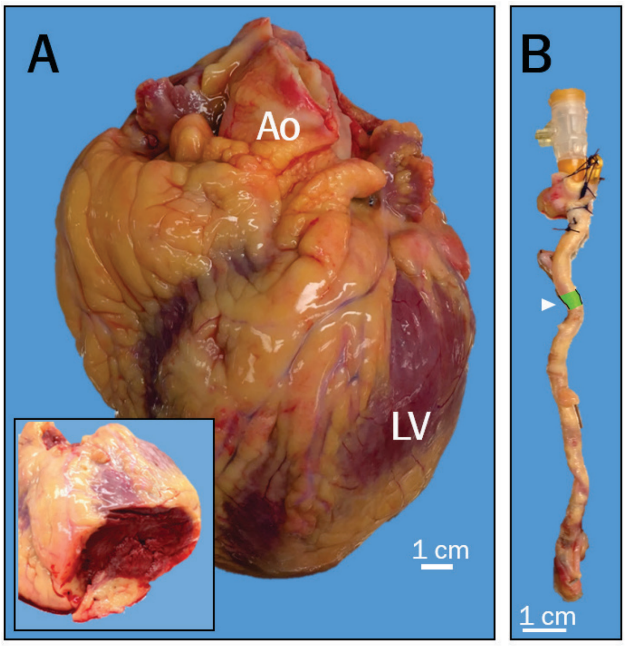

Figure 3.3. **Post-mortem human heart and right coronary artery gross image.** A) Gross image of the human heart, with the aorta (Ao) and hypertrophic left ventricle (LV) shown in the inset. B) Excised right coronary artery, with the approximate region of interest imaged by IVPA-US highlighted (green, arrowhead).

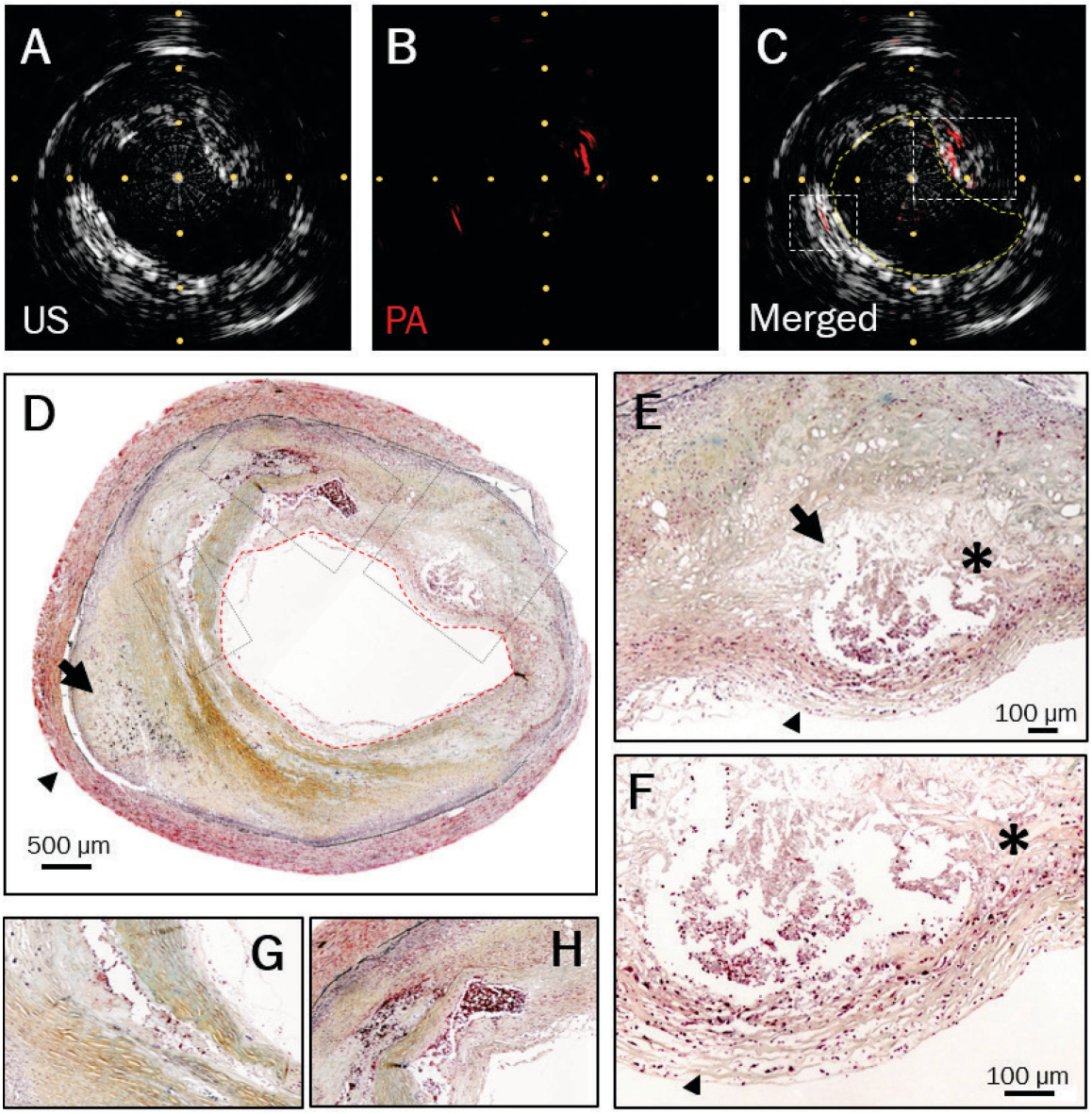

Figure 3.4. **IVPA-US imaging results and corresponding histopathology.** A) IVUS cross-sectional image, showing an eccentric raised lesion encroaching the lumen at 1-3 o'clock. B) IVPA image showing lipid (red). C) Merged IVPA-US image shows a strong area of PA signal in relation to the lumen as seen on IVUS (traced), suggesting the presence of two lipid-rich cores (boxes). D) Movat's pentachrome stained histology section, with lumen border traced and key features outlined in boxes; from left: thin lipid-rich necrotic core (G), intraplaque hemorrhage, large lipid-rich necrotic core (E,F). Also shown are microcalcifications stained black (arrow) and medial thinning (arrowhead). E, F) Magnified views of the large lipid-rich necrotic core (arrow) with cholesterol clefts (*) and an overlying thick fibrous cap with macrophage infiltration (arrowhead). G) Magnified view of the second lipid-rich necrotic core, thin in morphology with a thick fibrous cap. H) Non-communicating intraplaque hemorrhage, consistent with neovascularization. Horizontal and vertical axis tracings in A-C are 1 mm apart. Adapted from Hui et al. (*Sci Rep,* 2017).

3.3.2 Comparative IVPA-US and NIRS-IVUS Imaging of a Fresh Human Coronary Artery

We imaged a fresh human RCA harvested from a 59-year old male undergoing transplant surgery. The patient had coronary heart disease risk factors of obesity (BMI=31), smoking, past history of hypertension, and age. Additionally, the patient had past medical history of heart failure with reduced ejection fraction and paroxysmal atrial fibrillation. On *ex vivo* imaging of the diseased artery, we identified two advanced fibroatheromas with calcification on both IVPA-US and NIRS-IVUS (Fig. 3.5). Comparison between modalities was conducted with angiographic aid and identification of anatomical and physical landmarks, such as fiduciary side branches and the introducer sheath. We defined the atheroma proximal to the introducer sheath as Lesion 1 and the distal atheroma as Lesion 2 (Fig. 3.6). On both hybrid modalities, calcification was evident on ultrasound by strong echogenicity with acoustic shadowing. Furthermore, lipid was present as indicated by yellow color on the circumferential chemogram by NIRS and red color on co-registered cross-sectional images by IVPA-US. Characterization of the atherosclerotic features in both lesions were confirmed by histopathology, with calcified lipid pool areas measuring 0.42 mm^2 and 1.36 mm^2 for Lesions 1 and 2, respectively.

On IVPA imaging, we calculated the average cross-sectional lipid area within a 4-mm segment for both lesions. Lesion 1 had an average lipid area of 0.15 ± 0.004 mm^2 (Range: 0.08 – 0.24) and Lesion 2 had an average lipid area of 0.40 ± 0.03 mm^2 (Range: 0.04 – 1.04). Particularly, Lesion 2, within the measured 4-mm segment, had a significantly greater average lipid area than the remaining length of artery (0.40 mm^2 vs. 0.26 mm^2; $p<0.0001$). We further measured the total lipid area within a 4-mm segment for each lesion (Lesion 1: 9.57 mm^2, Lesion 2: 25.95 mm^2). Lastly, depth resolution and co-registered imaging allowed us to identify the contiguous lipid areas adjacent to calcification as the plaque lipid core and calculated the volumes as 0.11 mm^3 and 0.25 mm^3 for Lesions 1 and 2, respectively. Relation of the plaque lipid core to calcification and the lumen border is further illustrated by three-dimensional reconstruction of the 4-mm segments (Fig. 3.6C, D). These quantifications were in agreement with histopathology and similar measures made by NIRS-IVUS imaging.

On NIRS-IVUS, we found Lesion 2 to have a high $maxLCBI_{4mm}$ value of 326, consistent with the large lipid area and core volume measured by IVPA-US. No $maxLCBI_{4mm}$ was calculated for Lesion 1 due to lack of sufficient spectrally valid pixels. Using the generated chemogram, we approximated lipid areas as 5.22 mm^2 for Lesion 1 and 26.38 mm^2 for Lesions 2, comparable to the values measured by IVPA-US. Comparison of NIRS chemogram and IVPA fold-out map of PA signal intensity are illustrated in Figure 36, with the two lesion 4-mm segments highlighted. At areas where lipid was detected by IVPA, in the absence of an atheroma, PA signal was localized to arise from perivascular adipose tissue (PVAT) (Fig. 3.6E). No lipid was detected at identical regions by NIRS (Fig. 3.6F).

In addition, we characterized the calcification in both lesions by measuring the total length and maximal arc of calcification, as shown in Table 3.1. Both IVPA-US and NIRS-IVUS systems showed similar values, demonstrating comparable US resolution for the identification of calcification. Comparative imaging by multiple modalities and gold-standard histopathology confirm that depth-resolved IVPA-US has the capability to quantify and localize plaque lipid cores with calcification.

Table 3.1. **Comparison of lesion characteristics from *ex vivo* imaging of a human right coronary artery by NIRS-IVUS and IVPA-US.**

	Lesion 1 (Proximal)	**Lesion 2 (Distal)**
NIRS-IVUS Measured Lesion Characteristics		
$maxLCBI_{4mm}$	N/A	326
Total Lipid Area (mm^2)	5.22	26.38
Total Calcified Length (mm)	3.1	2.0
Maximum Arc of Calcification (°)	46.2	66.7
IVPA-US Measured Lesion Characteristics		
Average Lipid $Area_{4mm}$ (mm^2)	0.15 ± 0.004	0.40 ± 0.03
Total Lipid $Area_{4mm}$ (mm^2)	9.57	25.95
Lesion Lipid Core Volume (mm^3)	0.11	0.25
Total Calcified Length (mm)	3.4	2.4
Maximum Arc of Calcification (°)	58.1	66.4

Figure 3.5. **Correlation between modalities in a fresh human coronary artery.** A) *Ex vivo* angiogram of the artery, in which the sheath (I), side branches (II, V), and lesions locations (III, IV) are identified. Location III refers to Lesion 1 and location IV to Lesion 2. B, C) Corresponding cross-sectional still frames are shown from NIRS-IVUS (B) in which lipid is shown with yellow and from IVPA-US (C) in which lipid is represented by red. Notable side branches are indicated by arrowheads and calcification by arrows. D) Movat's pentachrome stained histological sections of lipid core lesions (*) with calcification (arrows). Horizontal and vertical axis tracings are 1 mm apart.

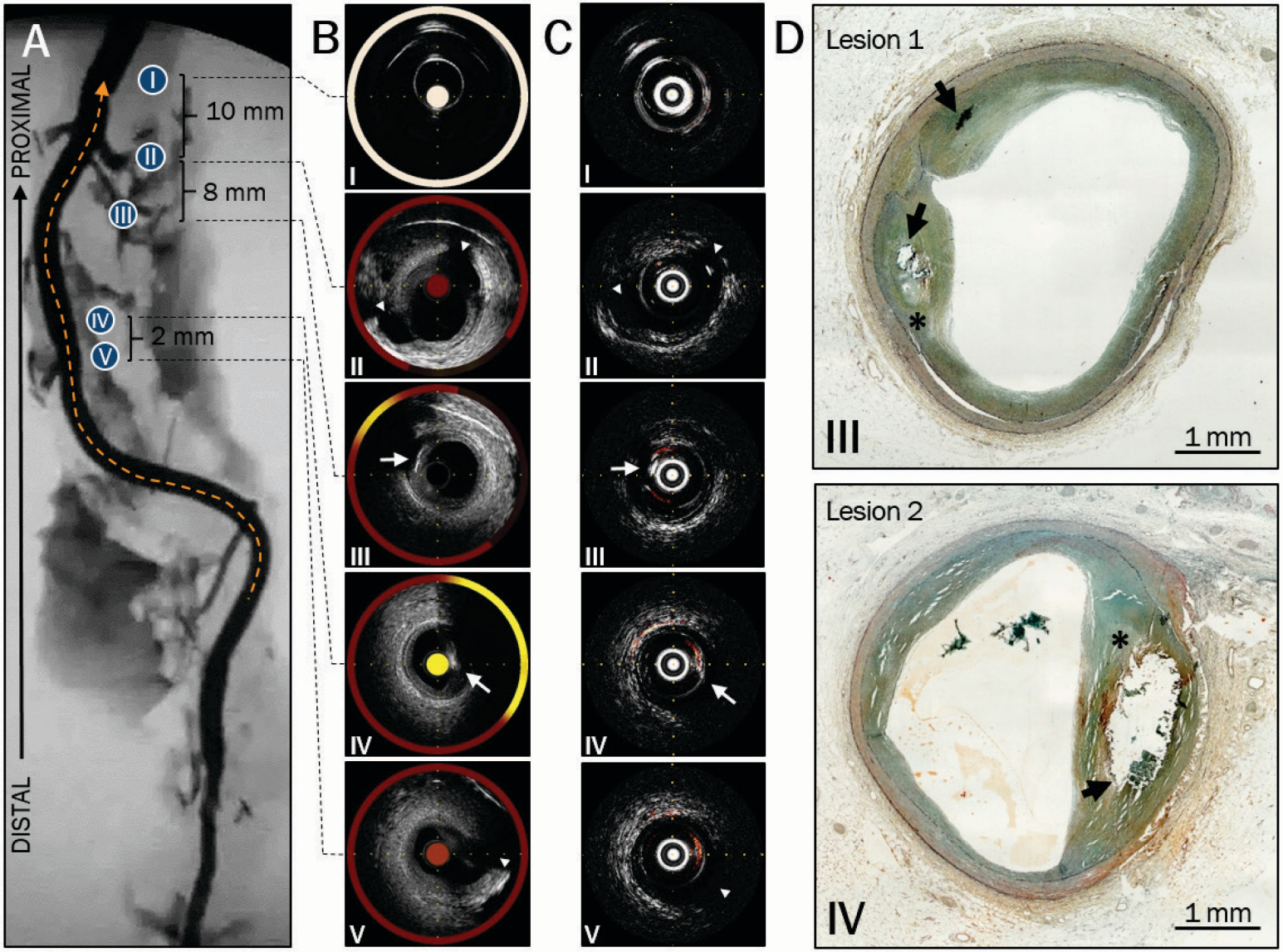
A
PROXIMAL
DISTAL
I
II
III
IV
V
10 mm
8 mm
2 mm
B
C
D
Lesion 1
1 mm
Lesion 2
1 mm

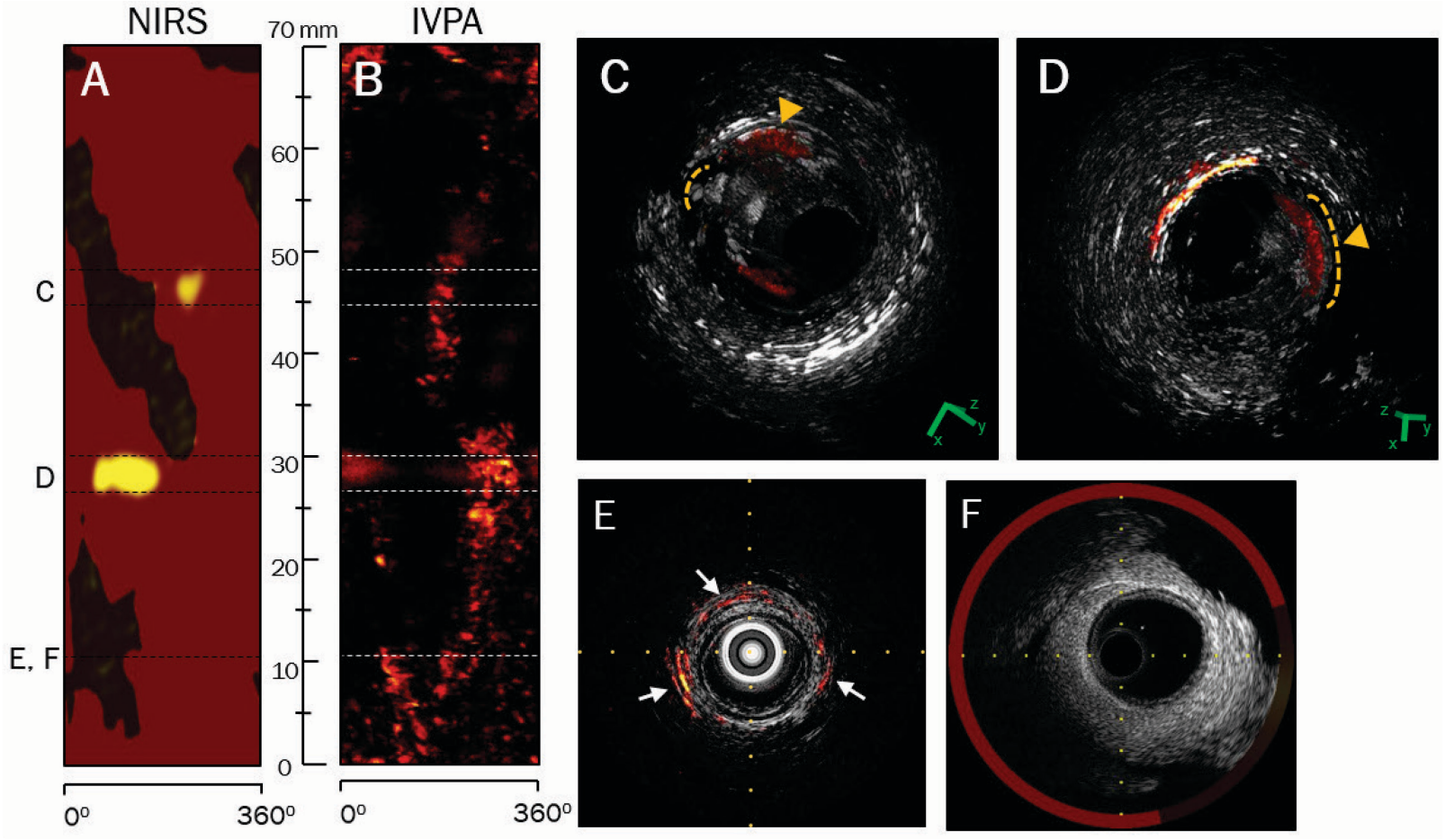

Figure 3.6. **Aligned chemogram comparison for human coronary artery imaging and 3D reconstructions of fibroatheromas imaged by IVPA-US.** A, B) At the highlighted 4-mm lesion segments, both modalities show lipid either by yellow color on the NIRS chemogram or red color on the IVPA fold-out map. C, D) Merged reconstructions for Lesion 1 (C) and Lesion 2 (D), in which the US channel is depicted in grayscale and PA channel in red. Calcification has been traced with a dash line and lipid core identified with an arrowhead. Both reconstructions are 4-mm in length and correspond to the segments highlighted in A and B. E) IVPA-US still frame image at a proximal portion of the artery, at which no lesion was observed and detected lipid (red) was localized as perivascular adipose tissue (arrows). F) NIRS-IVUS still frame at the same region, with no lipid detected. Horizontal and vertical axis tracings are 1 mm apart.

3.4 Discussion

In this study, we have demonstrated that our IVPA-US imaging system, with collinear and quasi-collinear catheter designs, can detect the lipid rich-cores with depth-resolution, as validated against gold-standard histopathology.

On IVPA-US imaging of a fixed atherosclerotic coronary artery, we identified two lipid cores by strong and unambiguous signal on IVPA. Furthermore, depth resolution allowed us to localize these plaque cores as superficial and quantify the size and shape. The larger plaque core (0.21 mm^2) was located close to the lumen border within a raised eccentric lesion. The smaller plaque core (0.07 mm^2) was within a fibrous area, as evidenced by the strong echogenicity on IVUS. Our findings were confirmed by correlation of plaque features and lumen morphology on histopathology. We characterized the plaque as an advanced fibroatheroma, with two lipid-rich necrotic cores that correlate in size and location to our imaging findings. The discrepancy in core areas calculated on histology versus IVPA-US was expected, as imaging identified areas of lipid with chemical-selectivity and on histology we calculated areas of the total plaque core. Although lipid-rich, plaque cores in advanced lesions have heterogeneity that also includes calcification, inflammatory infiltrate, and apoptotic cellular debris which are not apparent on imaging. Both IVPA and IVUS axial resolutions were insufficient to properly assess fibrous cap thickness, but with improvements this could be possible via post hoc calculation of the distance between the lumen border (by US) and lipid core (PA). Additionally, we identified intraplaque hemorrhage on histopathology, but not on IVPA-US imaging. This provides evidence of lipid-specificity, but demonstrates limitation in identifying multiple determinants of instability. In the future, identification of other components via spectral analysis, such as cholesterol crystals, may serve to provide information regarding plaque vulnerability as a surrogate marker [261]. Lastly, this investigation achieved milestones towards clinical translation. We provided the first demonstration of IVPA-US imaging at video-rate imaging speed (16 fps), comparable to commercial systems and sufficient to suppress artifacts of cardiac motion. In addition, we integrated our system with a real-time display interface. This nontrivial feature provided the operator with feedback necessary to adjust parameters (i.e. pulse energy, amplification, imaging and pullback speeds) and

catheter position based on the processed and displayed IVPA and IVUS images. The overarching limitations of our study include the lack of a protective sheath, imaging of a post-mortem specimen in which plaque features may be altered due to fixation, and demonstration in an ideal D_2O environment that does not mimic *in vivo* challenges [326]. These have been addressed subsequently in our fresh artery imaging experiment.

In our study of a fresh specimen, we provide the first comparison of IVPA-US to NIRS-IVUS for the detection of lipid core plaques. As the only approved device for imaging lipid rich plaques, NIRS-IVUS undoubtedly has great promise in clinical practice. Yet, lack of depth resolution limits quantitative imaging of lipid and relies upon LCBI as a derived measure to distinguish between high- and low-risk plaques, for which the optimal cutoffs are still undetermined [216, 217, 221, 222]. In this comparative study, we have shown agreement between modalities in detection of lipid at matching sites within the RCA, using IVUS-defined features such as calcification and branches as fiduciary landmarks to align pullbacks. These findings were confirmed on histopathology. Furthermore, we highlighted the value of depth resolution in lipid assessment. We have demonstrated the capability of IVPA-US to differentiate between superficial and deep lipid, i.e. lipid within a plaque core versus PVAT. We showed localization of lipid cores in relation to plaque features such as calcification and quantification of plaque volume. Volumetric quantification permits more meaningful longitudinal studies monitoring plaque changes. Furthermore, alterations in plaque morphology and composition would be more apparent with visualization of core dimensions and relation to other plaque components. This would aid in elucidation of the prevalence and mechanisms of TCFA development, stability, and rupture as discussed previously (see Chapter 2.4) [275, 327]. Additionally, in disease-free segments with lipid signal, we localized signals to arise from PVAT, a key mediator of atherogenesis [242, 255, 267-269]. This was not apparent on NIRS-IVUS imaging at the same region.

Lastly, we demonstrated functionality of an outer polyurethane sheath with minimal PA and US signal attenuation. This materials engineering feat fulfilled a prerequisite for *in vivo* imaging. A proper sheath is a practical necessity in order to provide a mechanical barrier to prevent bleeding at the site of catheter introduction *in vivo* (e.g. femoral artery), in addition to preventing damage and impingement of the rotating torque coil during pullback. Furthermore, a sheath protects the vascular endothelium from damage as the

catheter tip rotates and retreats at high-speed within the intravascular space during pullback. Although signal loss was minimal, there is room for improvement with the use of thinner materials and post-processing removal of PA artifacts arising from the sheath. We also demonstrated improved US resolution with our quasi-collinear catheter design and differential gain applied radially, i.e. higher gain at larger depths. Direct interrogation of the vessel wall without reflection allowed us to identify deep-field structures such as side branches and also characterize calcification with similar resolution to commercial devices. Our study was limited by a small sample size that did not include a range of atherosclerotic plaque phenotypes. Thus, we were unable to calibrate our thresholding algorithm for lipid area to match histopathological lipid core area and PVAT thickness. We intend to build a larger calibration data set to address this limitation.

3.5 Conclusions and Outlook

Despite advances in creating humanlike atherosclerosis in animal models, there is no substitute for imaging true complex atherosclerotic plaques from humans. Here, we provide *ex vivo* validation of IVPA-US for the detection of advanced lesions with depth resolution to localize and quantify lipid cores, as confirmed by histology. Furthermore, as modalities for lipid imaging advance in capability and combination, comparison will be instrumental in determining the relative advantages and disadvantages. To our knowledge, this is the first head-to-head study of IVPA-US against NIRS-IVUS for characterization of post-mortem human coronary atherosclerosis. We have shown agreement between modalities and the value of depth resolution. Lastly, this study introduced key technical innovations towards clinical translation: real-time imaging at video-rate speeds, improvement of US resolution, and incorporation of a sheath.

Understanding lipid core dimensions would provide powerful information in longitudinal studies of the efficacy of pharmaceutical therapies, lifestyle modifications, and public policy measures [309]. Furthermore, early identification of plaques with superficial lipid cores would allow cardiologists to implement preventive measures such as aggressive medical therapy or placement of vascular scaffolds—both with the intent to promote plaque stabilization [277-279, 283]. Thus, IVPA-US imaging could open opportunities beyond the reach of other intervascular imaging tools [57, 58, 61].

4. *IN VIVO* ASSSESSMENT OF IVPA-US IMAGING IN OSSABAW SWINE WITH METABOLIC SYNDROME

4.1 Rationale

Ex vivo studies for intravascular imaging device validation are natural prerequisites for clinical translation. These studies provide the basis for iterative refinement of catheter design, calibration of classification algorithms, and demonstration of predictive accuracy, all in a controlled environment. To simulate *in vivo* conditions, researchers have incorporated pulsatile flow pumps for perfusion of whole blood at physiologic pressure and temperature [203]. Despite these efforts, there are many *in vivo* parameters that are not recapitulated well or at all *ex vivo*. Vascular motion, hemodynamics, and physiologic noise are all better studied *in vivo*. Furthermore, evaluation of safety and robustness of the device and procedure are best conducted *in vivo*, where there is less control of the environment. Thus, parallel *in vivo* testing in preclinical models can provide valuable information guiding catheter enhancement and validation. In this work, we present *in vivo* evaluation of our IVPA-US imaging catheter in a systematic comparative study against NIRS-IVUS. We use both modalities to investigate sensitivity to detect early atherosclerosis in Ossabaw miniature swine with metabolic syndrome (MetS) versus lean control swine. We further use this investigation as an opportunity to evaluate the safety, performance, and reproducibility of our device for *in vivo* imaging. The work presented in this chapter is currently under review for publication.

4.2 Materials and Methods

4.2.1 IVPA-US Imaging System and Data Acquisition

The portable high-speed IVPA-US imaging system used in this work has been described in detail previously (see Chapter 3.2.1). Briefly, a nanosecond Nd:YAG pumped optical parametric oscillator excitation laser source emitting at 1.7 μm with a 2 kHz repetition rate was used for photoacoustic excitation. A collinear catheter with a 42 MHz transducer was used for all swine imaging presented in this chapter. The catheter was fully enclosed within a protective sheath composed of polyurethane and had an outer diameter of 1.6 mm. For

all IVPA-US imaging, the catheter sheath was flushed with D_2O due to decreased optical absorption compared to H_2O.

4.2.2 Animal Care and Use

Ossabaw miniature swine (*n*=3) were maintained to meet the characteristics of MetS for eight months, seven of which they were fed a hypercaloric, atherogenic diet (1 kg/day), and aged approximately 16 months at the time of euthanasia. For a lean control, a subset of swine (*n*=2) were fed a standard chow diet (0.7 kg/day). Swine were individually housed with free access to water. Metabolic data including body weight, blood pressure, serum chemistry, and plasma lipids were collected to confirm development of MetS and dyslipidemia. Development of MetS and CAD in this naturally progressive animal model of human disease has been characterized in previous work (e.g. [294, 296, 328]).

Anesthesia was induced via intramuscular injection of telazol (5-6 mg/kg) and xylazine (2.2 mg/kg), and maintained with 2-4% isoflurane mixed with 100% oxygen. The isoflurane level was adjusted during the in vivo procedure to maintain stable hemodynamics. This protocol was performed according to the *Guide for the Care and Use of Laboratory Animals* and approved by the Indiana University School of Medicine Animal Care and Use Committee [299].

4.2.3 *In Vivo* Imaging: Angiography, Grayscale IVUS, IVPA-US

A shortened 7 Fr introducer sheath was inserted in the right femoral artery of swine and heparin was administered (50 U/kg). An angiogram with contrast was recorded to visualize lower limb vascular anatomy. Next, a shortened 7 Fr guiding catheter was advanced to access the right iliac artery, through which our 4.8 Fr, 42 MHz IVPA-US catheter was advanced 80 mm distally and two automated pullbacks were recorded at 0.5 mm/s (Fig. 4.1). All *in vivo* IVPA-US data were collected at 8 fps imaging speed. Following IVPA-US catheter removal, a 3.2 Fr, 45 MHz commercial grayscale IVUS catheter (Revolution, Volcano, Corp.) was advanced 80 mm distally and a pullback was recorded at 0.5 mm/s. Angiograms without contrast were recorded after catheter placement and with contrast after removal. In one lean control animal, right and left iliac arteries were both imaged. Following imaging, the animals were euthanatized by isoflurane overdose and cardiectomy.

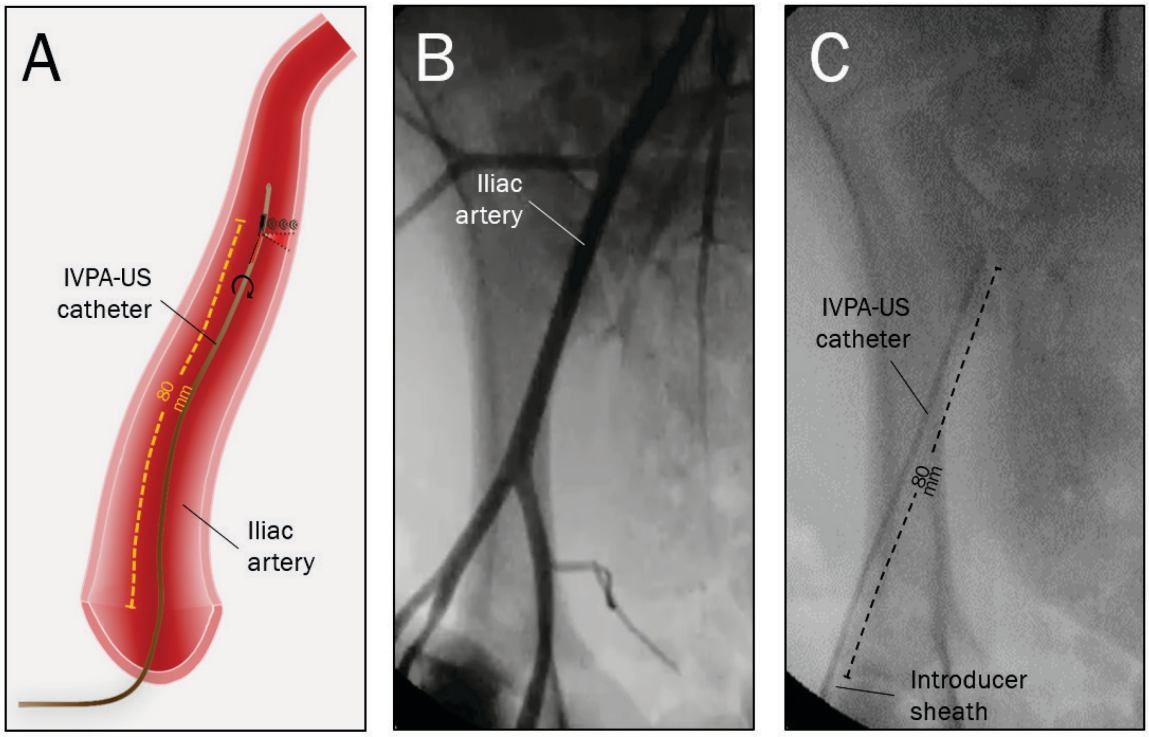

Figure 4.1. **IVPA-US imaging probe and *in vivo* imaging procedure.** A) Schematic of the *in vivo* procedure, in which the IVPA-US catheter was advanced 80 mm into the iliac artery of swine. B) Angiogram with contrast to visualize vascular anatomy. C) Angiogram without contrast to confirm IVPA-US catheter placement at 80 mm distal to the introducer sheath.

4.2.4 Tissue Recovery and *Ex Vivo* Imaging

Following euthanasia, the iliac artery was isolated, marked with a suture knot 80 mm distal to the guiding catheter, and dissected out of the animal with the introducer sheath in place. Side branches and the distal end were ligated with suture for pressure-perfusion during *ex vivo* imaging. The Ossabaw iliac artery segment was pinned in a Sylgard® 184 Silicone Elastomer tray and submerged in 1X PBS, at room temperature. The IVPA-US catheter was advanced to the 80 mm mark and perfused with 1X PBS at physiologic pressure, during which an automated pullback was recorded at 0.25 mm/s. All *ex vivo* IVPA-US data were collected at 4 fps imaging speed. This procedure was repeated with a 3.2 F, 40 MHz NIRS-IVUS catheter (TVC Insight, Infraredx, Inc.) with a 0.5 mm/s pullback speed.

4.2.5 Imaging and Histology Quantitative Analysis

IVPA-US imaging data were post-processed to reduce noise, and pixels at which PA intensity was greater than a set threshold were counted per cross-sectional frame to

calculate lipid area (4 times the background noise for all *ex vivo* data sets and 5 times the background noise for all *in vivo* data sets) (Fig. 3.2). Pullback segments in which the introducer sheath was present were excluded from analysis. All lipid area measurements were calculated using MATLAB software (MathWorks, Inc.). Cross-sectional lipid areas were binned and averaged for correlation analysis between repeated *in vivo* and *ex vivo* pullbacks to assess reproducibility of data. The NIRS-IVUS TVC Imaging System was used to generate 2D chemograms. The system also generated block chemograms, representing the artery in 2-mm segments with discrete colorized representation of the probability of lipid present. We defined blocks colored red as having no lipid present ($P<0.57$) and all other colors as having high probability of lipid present (orange: $0.57<P\leq0.84$, tan: $0.84<P\leq0.98$, and yellow: $P\geq0.98$) [206]. Lastly, the total LCBI was calculated by the system.

Imaged arteries were pressure-fixed using 10% formalin and placed in formalin overnight. Arteries were then grossly sectioned in 3-4 mm segments. Next, segments were paraffin embedded, thin sectioned, and stained with H&E and Veorhoeff-Van Gieson elastin stain. Contralateral control iliac arteries from Ossabaw swine were not pressure-fixed. Blinded analysis of maximal intimal thickness was performed using ImageJ to measure the thickest neointimal layer as determined on Veorhoeff-Van Gieson stained sections.

All data are described as mean ± SEM. Statistical significance was defined as $p<0.05$. Unpaired, two-tailed Student's t-tests and Pearson's correlation were used as appropriate using GraphPad Prism statistical software (GraphPad Software, Inc.).

4.3 Results

4.3.1 Multimodal Imaging of Ossabaw Swine Iliac Arteries

Ossabaw swine on a hypercaloric, atherogenic diet developed the characteristics of MetS, including significantly greater total cholesterol, triglycerides, blood glucose, and weight at sacrifice compared to swine in the lean control group (Table 4.1).

Table 4.1. **Metabolic Characteristics of Ossabaw Swine**

	Lean (*n* = 2)	**MetS (*n* = 3)**	***P*-Value**
Sex (M/F)	1/1	0/3	N/A
Weight at sacrifice (kg)	50.5 ± 10.5	95.0 ± 1.5*	**0.01**
Mean weight gain (kg)	31.0	58.7 ± 3.0	N/A
Serum chemistry profile			
AST (IU/L)	33 ± 4	48 ± 7	0.21
ALT (IU/L)	24 ± 4	26 ± 5	0.79
Alkaline Phosphatase (IU/L)	100 ± 13	85 ± 9	0.39
Bilirubin (mg/dL)	0.1	0.3 ± 0.1	N/A
Blood glucose (mg/dL)	62 ± 3	167 ± 24*	**0.04**
Plasma lipids			
Cholesterol (mg/dL)	71 ± 12	465 ± 53*	**0.01**
Triglycerides (mg/dL)	26 ± 2	63 ± 4*	**0.01**

*$p < 0.05$ when compared with the lean group.
AST, aspartate aminotransferase; ALT, alanine aminotransferase.

On *in vivo* and *ex vivo* iliac artery imaging of both groups, no intimal disease was observed on all modalities, consistent with histology which showed minimal neointimal hyperplasia (Fig. 4.2). In the artery segments where lipid signal was present on IVPA-US imaging, it was localized to the perivascular region and confirmed as perivascular adipose tissue (PVAT) by histology (Fig. 4.3D). On *in vivo* IVPA-US imaging, we found the average cross-sectional lipid area was significantly greater in the iliac arteries of swine with MetS as compared to lean swine (0.089 ± 0.016 mm^2 vs. 0.059 ± 0.001 mm^2; $p<0.0001$) (Fig. 4.4A). These results were also observed on *ex vivo* imaging (0.032 ± 0.001 mm^2 vs. 0.005 ± 0.0002 mm^2; $p<0.0001$) (Fig. 4.4B). On *ex vivo* NIRS-IVUS imaging, we found similar results, as arteries of swine with MetS had significantly more 2-mm block chemograms with high probability of lipid present than arteries of lean swine (8/117 blocks with lipid vs. 0/80 blocks with lipid; $p=0.02$). Additionally, arteries of swine with MetS

had a greater average total LCBI than lean swine (50.3 vs. 12.0; p=0.48). However, on histology, we did not observe any pathologic disease and no significant difference in the maximal intimal thickness (MetS: 114.2 ± 25.9 µm, Lean: 92.4 ± 15.8 µm; p=0.49) (Fig. 4.4C). Taken together, these results conclude IVPA-US is comparable to NIRS-IVUS in sensitivity for the detection of increased lipid deposition, even before overt pathology is apparent on histology. Depth-resolved IVPA-US imaging provides the ability to localize lipid deposition; more specifically, lipid signals that arise from PVAT.

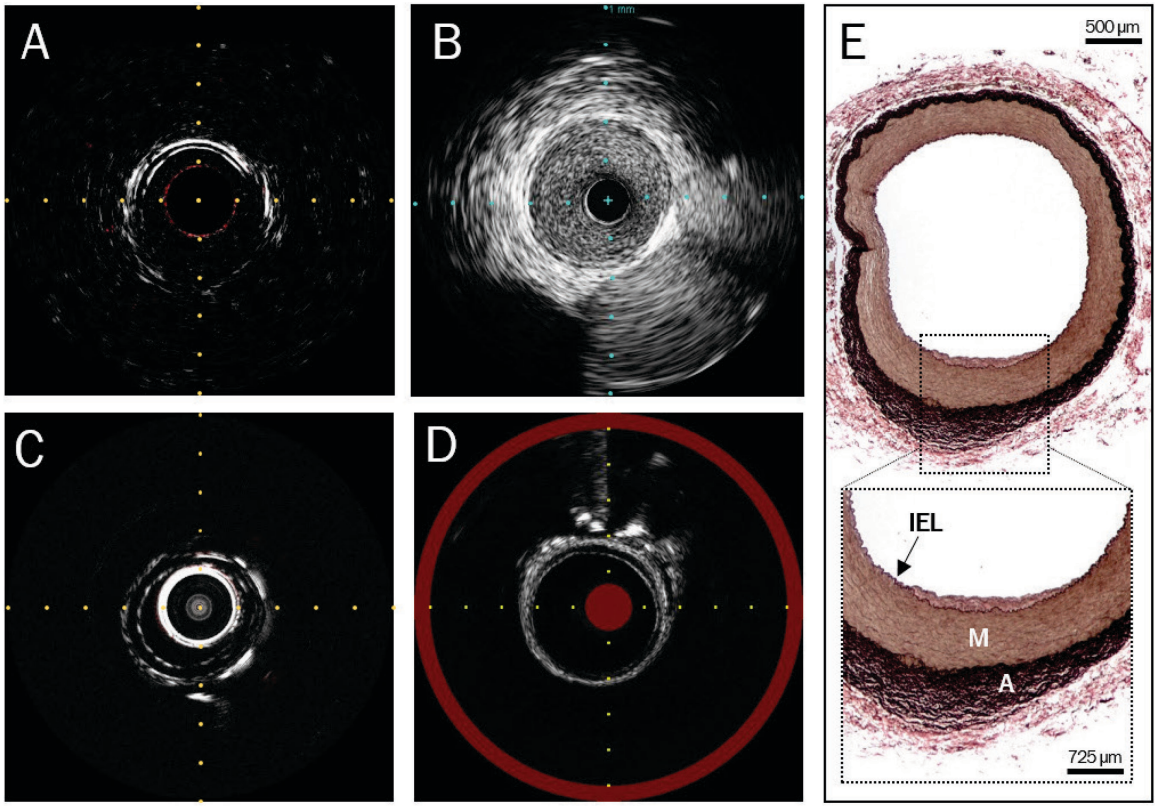

Figure 4.2. **Imaging and histology from a MetS Ossabaw swine iliac artery.** A) *In vivo* IVPA-US still frame, in which no lipid deposition and a healthy artery morphology (three-layer appearance) was observed. B) *In vivo* commercial IVUS still frame, depicting healthy artery morphology, i.e. 3-layer appearance. C) *Ex vivo* IVPA-US still frame, in which no lipid deposition and a healthy artery morphology were observed. D) *Ex vivo* NIRS-IVUS still frame, in which no lipid deposition and a healthy artery morphology were observed. E) Verhoeff–Van Gieson stained histological section, showing healthy artery morphology with a small area of neointimal thickening (inset) on the luminal side of the internal elastic lamina (IEL). M, media; A, adventitia. Horizontal and vertical axis tracings are 1 mm apart.

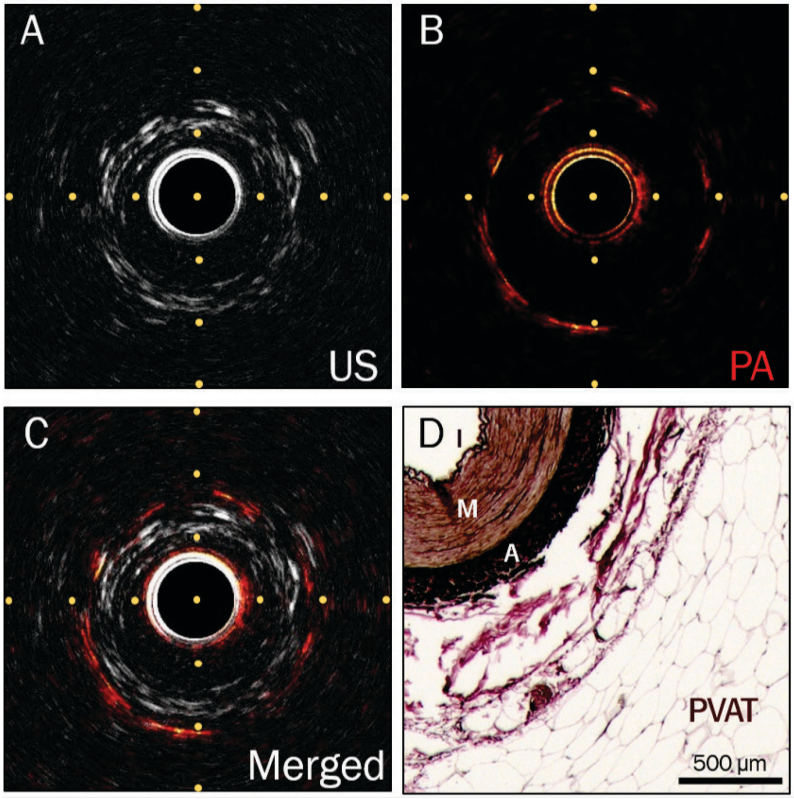

Figure 4.3. ***In vivo* IVPA-US imaging from a MetS Ossabaw swine.** A) IVUS channel showing a healthy three-layer appearance of the iliac artery. B) IVPA channel showing concentric lipid signal (red). C) Merged composite showing lipid signal localized to the perivascular region. D) Verhoeff–Van Gieson stained histological section showing abundant perivascular adipose tissue (PVAT). I, intima; M, media; A, adventitia. Horizontal and vertical axis tracings are 1 mm apart.

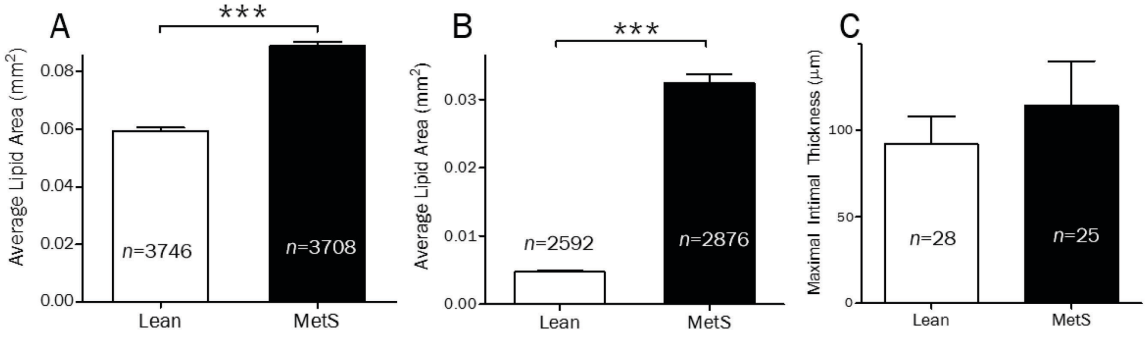

Figure 4.4. **Average cross-sectional lipid area and maximal intimal thickening in iliac arteries as determined by IVPA imaging and histology.** The average cross-sectional lipid area, as calculated by photoacoustic signal intensity per frame above a pre-determined threshold, is significantly greater in the iliac arteries of swine with MetS as compared to lean swine, both by *in vivo* (A) and *ex vivo* (B) imaging; *** $p<0.0001$; *n* refers to number of cross-sectional frames analyzed. C) However, there was no significant difference in the average maximal intimal thickness the iliac arteries of swine with MetS as compared to lean swine; $p=0.49$; *n* refers to number of histological sections analyzed.

Lastly, we evaluated the safety of the *in vivo* imaging procedure and reproducibility of our results. On angiography, we observed no significant vasospasm after IVPA-US pullback (Fig. 4.5A,B). On histology, we did not observe any significant damage to the internal elastic lamina of imaged arteries compared to contralateral control arteries (Fig. 4.5C-F). Additionally, in three arteries, we performed repeat *in vivo* pullbacks and there was significant correlation of lipid area between pullbacks ($p<0.0001$ for all data sets) (Fig. 4.6). In a MetS-group swine iliac artery, we further compared lipid area measures from *in vivo* pullbacks with *ex vivo* pullback data and we also found significant correlation ($p<0.05$ for all data sets) (Fig. 4.7).

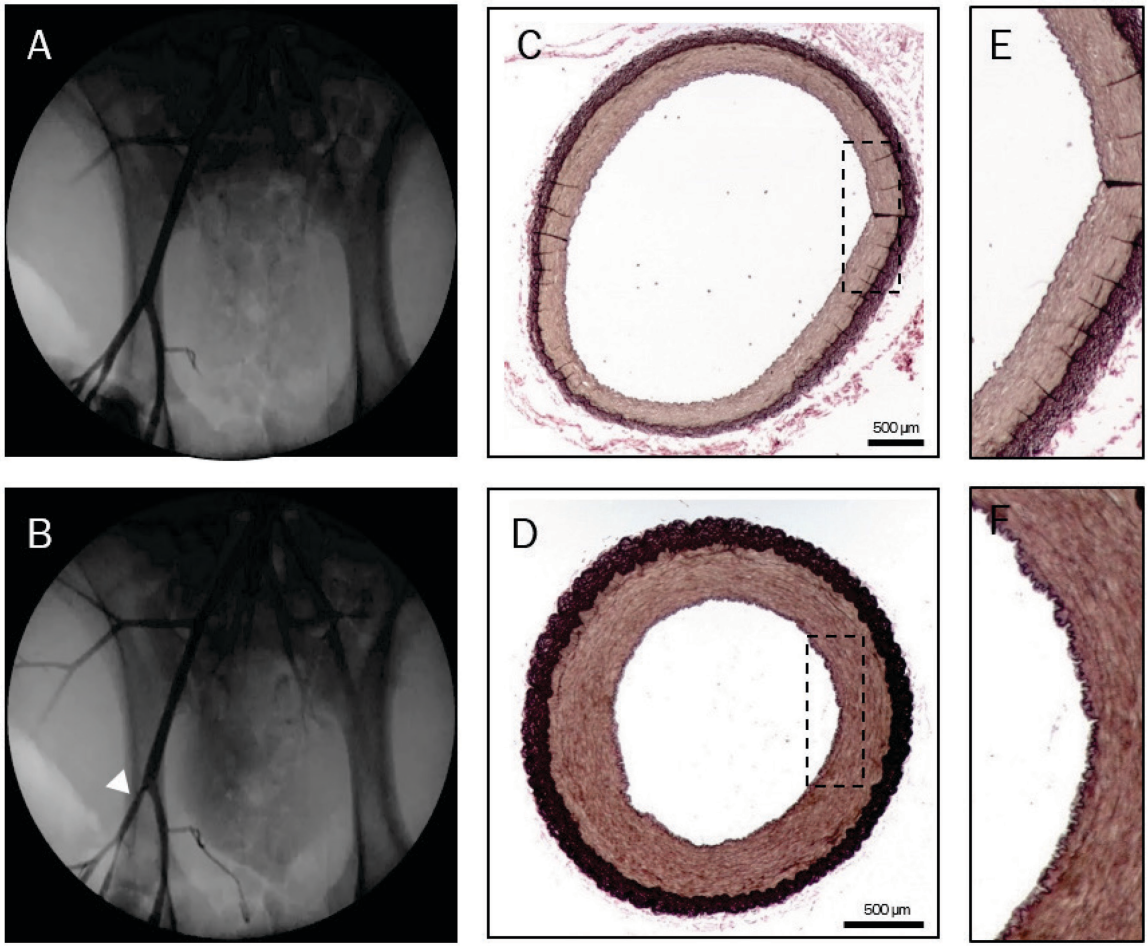

Figure 4.5. **Sheath performance as measured by post-catheterization vasospasm and endothelial denudation.** A) Pre-IVPA-US angiogram of an artery without catheter intervention. B) Post-IVPA-US angiogram taken immediately after pullback, showing only mild spasm of the vessel (arrowhead). C) Verhoeff–Van Gieson stained histological section from an imaged iliac artery, showing an intact internal elastic lamina (inset, E). D, F) Uncatheterized contralateral iliac artery as control.

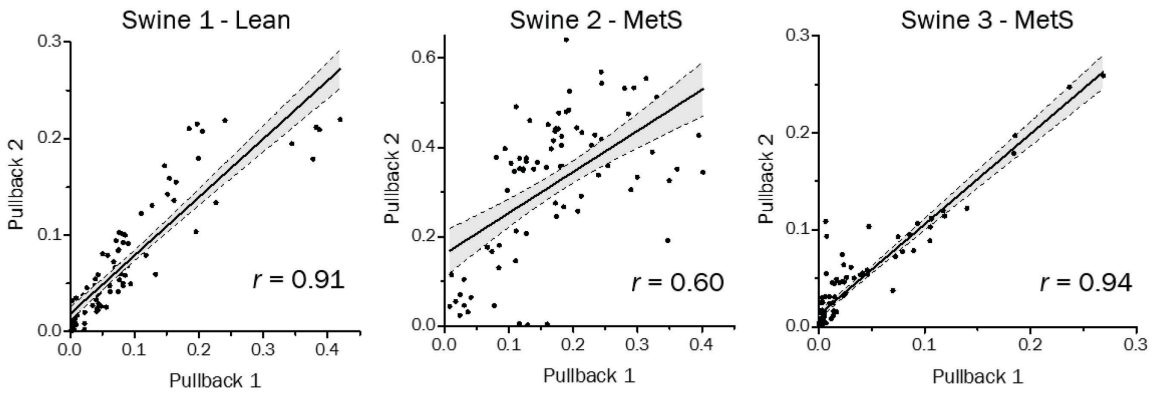

Figure 4.6. **Reproducibility of *in vivo* procedure and results.** In three swine, we repeated our pullback procedure to study the reproducibility of our catheter for lipid area data acquisition. In each animal, we observe significant correlation between the initial (Pullback 1) and repeat (Pullback 2) data sets. All data sets were averaged and binned to 50 data points.

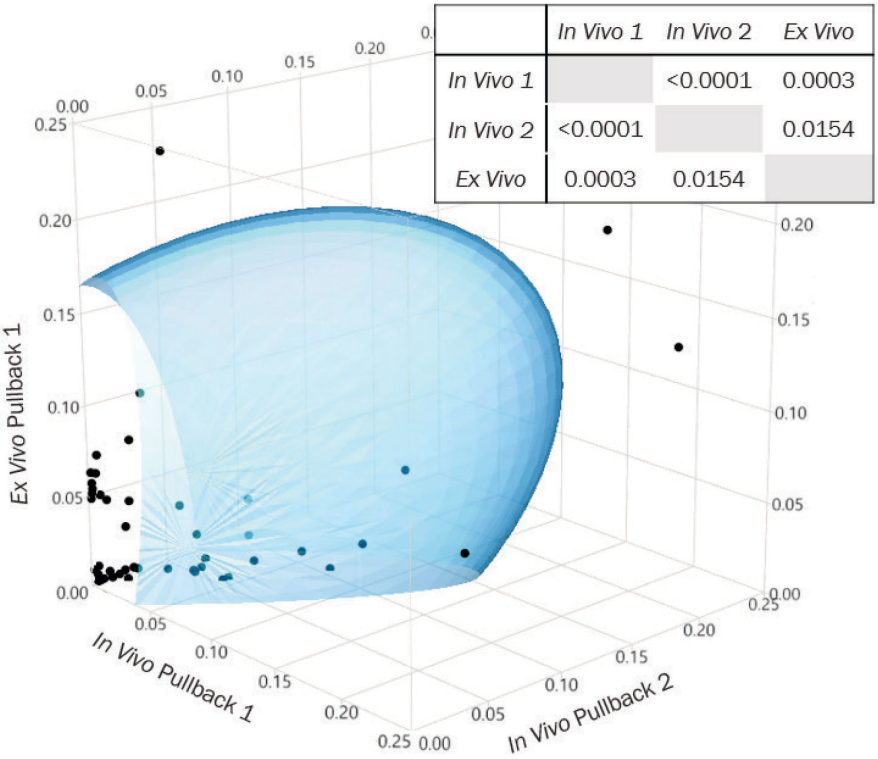

	In Vivo 1	*In Vivo 2*	*Ex Vivo*
In Vivo 1		<0.0001	0.0003
In Vivo 2	<0.0001		0.0154
Ex Vivo	0.0003	0.0154	

Figure 4.7. **Correlation plot between *in vivo* and *ex vivo* results with 95% confidence ellipsoid.** In a swine with MetS, in which we had minimal noise in two repeat *in vivo* pullbacks (8 fps imaging speed and 0.5 mm/s pullback speed) and one *ex vivo* pullback (4 fps imaging speed and 0.25 mm/s pullback speed), we found average cross-sectional lipid areas to significantly correlate between all data sets (all $p < 0.05$). All data sets were averaged and binned to 50 data points.

4.4 Discussion

Here, we have demonstrated detection of increased lipid deposition in Ossabaw swine with MetS versus lean swine by *in vivo* IVPA-US imaging, in agreement with *ex vivo* NIRS-IVUS imaging of the same specimens. To our knowledge, this was the first comparative *in vivo* IVPA-US imaging investigation for the detection of native atherosclerosis. We did not observe any significant intimal pathology on all structural imaging modalities (angiography, commercial IVUS, and IVUS from both hybrid devices) and histology in both MetS and lean animals. Thus, we conclude agreement in negative control samples. However, on compositional modalities, i.e. NIRS and IVPA, we observed inter-group differences in arterial lipid content. MetS-group swine with dyslipidemia exhibited significantly greater detected lipid than lean swine, as measured by lipid area on IVPA and block chemogram on NIRS. As NIRS-IVUS lacks depth-resolution, we were unable to characterize the source of detected lipid. These results were problematic as no lipid-laden intimal pathology was observed on histology and NIRS spectral data is limited to a depth of 1 mm or less [206, 254]. It is feasible that NIRS detected PVAT, given that the artery was healthy with wall thickness less than 0.5 mm in some instances (Fig. 4.5C). On depth-resolved IVPA-US imaging, we were able to localize the source of lipid signal as perivascular, as confirmed by histology. Intravascular detection of PVAT would be valuable in investigating its implication in atherogenesis. Recent studies have shown the role of PVAT in "outside to inside" local stimulation of atherosclerotic plaque formation via adipokines and pro-inflammatory cytokines [269]. Additionally, there is extensive evidence of the correlation between PVAT thickness/volume and CAD metrics, such as percent stenosis, coronary calcium score, presence of plaque, and MACE [268]. Furthermore, work by our group has shown excision of PVAT arrests atherogenesis [329, 330]. However, PVAT is traditionally measured by computed tomography along the cardiac short axis and co-localization to intravascular measures such as plaque burden are not possible on a routine basis. In other words, we do not have the tools necessary to answer the question over the length of the artery: do local depots of PVAT contribute to the development of underlying atherosclerotic lesions? This shortcoming could be addressed by IVPA-US, which has penetration depths of up to 6 mm and can imaged plaque burden and PVAT in one procedure.

Notably, recent hypotheses have suggested assessment of 'vulnerability' not be limited to scanning coronary arteries for solitary lesions. There is a lack of consensus evidence to support the notion that lesions deemed high-risk by imaging are the same lesions to progress to cardiovascular events [275, 286, 327]. In fact, many lesions regress without event, while others rupture without event. It is proposed that lipid imaging be extended to include assessment of the entire artery, to account for the complex and dynamic pathophysiology regulating plaque rupture. In this work, we have shown quantification of average cross-sectional lipid area in swine iliac arteries, without solitary lesions. The measured difference in lipid area between groups likely arise from PVAT, a potential mediator of atherogenesis. Thus, the demonstrated sensitivity of IVPA-US imaging for early disease is advantageous in assessment of an entire artery for vulnerability to a future event.

Additionally, our study provided significant findings pertinent to future clinical application. First, we did not observe any iliac vasospasm or any other adverse angiographic outcomes (dissection, perforation, thrombus, no-reflow) after IVPA-US pullback. Second, no peri-procedural adverse events occurred during IVPA-US imaging, including electrocardiograph ST-segment elevation, ventricular arrhythmias, and severe bradycardia. Additionally, there was no apparent endothelial denudation in iliac arteries on histology. The reported safety of our device and procedure was due to skilled operators and the incorporation of an outer polyurethane sheath. Further testing is necessary to meet regulatory safety and biocompatibility requirements. Lastly, clinical translation of IVPA-US will require validation against a robust data set of human histopathology, conducted *ex vivo*. Here, we have shown evidence in swine demonstrating correlation between *ex vivo* imaging through saline and *in vivo* imaging through blood. This provides strong evidence in the methodology and results presented previously (Chapter 2 and 3), and for future *ex vivo* investigations.

This study is limited by the lack of lipid-laden pathology in the iliac arteries of Ossabaw swine and subsequent absence of analysis for correlation of *in vivo* lipid imaging to histopathology. The lack of overt atherosclerosis was in spite of elevated cholesterol of swine in the MetS group. Minimal peripheral atherosclerosis with diet alone has been observed in this model previously [331]. In future studies, with greater catheter flexibility

and miniaturization, we intend to advance our catheter to the swine coronary arteries in which atherosclerotic disease develops more predictably [294, 296]. Furthermore, due to the small sample size, we were unable to calibrate our thresholding algorithm for lipid area to match PVAT thickness. We intend to build a larger calibration data set to address this limitation. Lastly, in this study we used a collinear catheter design. This design, combined with attenuation from both the sheath and luminal blood, limited US resolution.

4.5 Conclusions and Outlook

In this study, we demonstrate quantification of early atherosclerotic changes in Ossabaw miniature swine with MetS and dyslipidemia by IVPA-US imaging, with comparison to previously validated NIRS-IVUS imaging. We provide the first comprehensive comparison of *in vivo* and *ex vivo* IVPA-US imaging to *ex vivo* NIRS-IVUS and other existing modalities, including traditional IVUS and angiography. We detected limited lipid content with both hybrid modalities, in agreement with mild neointimal thickening on histology in both groups. Comparison of groups showed MetS swine had significantly greater arterial lipid than lean swine, by both modalities. Depth resolution of IVPA-US allowed us to localize detected lipid as PVAT.

There remain significant hurdles preventing clinical translation of IVPA-US. These include catheter design considerations, such as further miniaturization to a 1 mm diameter with sheath, optimized sheath material with reduced transmission loss, and broadband transducer covering low-frequency PA signals. Furthermore, development and validation of predictive algorithms that match IVPA-US lipid area to gold-standard histopathology will require a considerably larger and heterogeneous sample size. Nonetheless, small preclinical *in vivo* investigations performed in parallel provide unmatched feedback towards optimal catheter design and highlight the potential opportunities for intravascular imaging. With IVPA-US imaging, we see potential beyond imaging focal lipid-laden plaques. Atherosclerosis is a dynamic and chronic process, with many systemic and local factors that regulate progression to the final act: plaque rupture and thrombus. With depth-resolved detection of lipids, IVPA-US is a powerful tool to delineate the role of PVAT in this course.

5. CONCLUSION AND FUTURE DIRECTIONS

5.1 Conclusions

Comprehension of CAD and the complex pathophysiology leading to adverse cardiovascular events has been in part due to the widespread development and demonstrated utility of intravascular imaging tools over the past three decades [11, 73, 128, 161, 281, 327]. Current understanding has brought discussion and intense research to detect 'vulnerable' plaques or TCFAs to the front line [55, 144, 275, 276, 285, 288, 332]. It is hypothesized that a plaque rupture contributes to approximately 1 in 10 deaths in the United States [276, 333]. Currently, several intravascular modalities aim to target the hallmarks of TCFAs that contribute to its propensity for dangerous rupture: a weak thin-fibrous cap with inflammatory infiltrate, a pro-thrombogenic lipid-rich necrotic core, and positive remodeling that evades detection on routing examination [24, 26, 55, 58, 60, 272]. Of all technologies, NIRS-IVUS has been at the leading edge of demonstrating clinical value of the identification of lipid core plaques as a prognostic indicator of cardiovascular outcomes [216, 217, 221]. Preliminary studies have supported the notion that accurate detection of vulnerable plaques by a reliable intravascular modality, or combination of modalities, could be predictive of lesions at high risk to progress to cardiovascular events. Multiple ongoing prospective studies using NIRS-IVUS, including PROSPECT II ABSORB sub-study (NCT02171065), the Lipid Rich Plaque Study (NCT02033694), PREDICT (NCT02792075), and PREVENT (NCT02316886), aim to answer this important question [222]. Importantly, these studies must also address interpretation of data. As NIRS-IVUS lacks depth resolution to localize and quantify lipid cores, the threshold of risk is reliant on a LCBI metric and unclear of its meaning.

IVPA-US, an emerging modality that also targets lipids, has the power to provide clarity in this doubt and complete a missing piece of the picture: true visualization of lipid-rich plaque cores. This critical information—localization and quantification of lipid within a plaque—would have substantial clinical relevance in the areas of mechanistic studies, preventative cardiology, and interventional cardiology. Mechanistically, *in vivo* ability to longitudinally monitor the dynamic changes of a lipid core as it stabilizes or destabilizes would provide a stronger understanding of

vulnerable plaque rupture beyond what we know from post-mortem histopathology. Similarly, observational studies of how pharmaceutical therapies alter plaque morphology and lipid-core size could prompt discovery of novel and aggressive medical therapies for prevention of future cardiac events [218, 219]. Lastly, the ability to visualize the extent to which a lipid-rich core is vulnerable to rupture based on size and superficiality could provide a cardiologist with sufficient evidence to intervene with a protective scaffold [277-279]. Thus, despite the numerous intravascular imaging tools being developed or hybridized for the cardiologist's toolbox, IVPA-US has demonstrated powerful and unique capabilities to be at the forefront. No other modality has the capability of chemically-specific detection of lipid with the same resolution and depth as IVPA-US, as evidenced by the key conclusions drawn from work presented in this dissertation.

First, we demonstrated lipid detection was feasible using an IVPA-US collinear catheter to *ex vivo* image a fixed carotid artery specimen from a dyslipidemic Ossabaw swine. In a fresh swine carotid artery with preclinical atherosclerosis, we further validated IVPA-US with comparison against gold-standard histopathology. Additionally, we compared IVPA-US to NIRS-IVUS in this specimen, which highlighted the advantage of depth-resolved detection and quantification. In a similar manner, we provided validation of IVPA-US imaging for the detection of lipid core plaques in fixed and fresh human coronary artery specimens with advanced atherosclerotic lesions. Our results were in agreement with histopathology and NIRS-IVUS. It is only by virtue of depth-resolved lipid imaging by IVPA, co-registered with IVUS, that we were able to localize the plaque core and calculate total volume. Lastly, we showed *in vivo* feasibility using an IVPA-US catheter with an outer sheath in a systematic comparative study performed in Ossabaw swine. Again, depth resolution allowed us to localize lipid; however, not to a lipid-rich plaque core, but perivascular adipose tissue. Thus, these advantages offered from the combination of light and sound can advance our knowledge of atherosclerosis, change clinical diagnosis and management, and ultimately reduce CAD-related morbidity and mortality.

5.2 Future Directions

Currently, our conclusions towards validation of IVPA-US imaging for the detection, localization, and quantification of lipid-laden atherosclerotic plaques have suffered from a limited sample size. Naturally, the future directions of our work entail repeating described studies with a greater sample size. Particularly, we intend to image a much larger, robust set of post-mortem fresh human coronary arteries that include a wide range of atherosclerotic phenotypes. An appropriate cohort would include upwards of 80 hearts and 200 total coronary artery segments, similar to landmark *ex vivo* studies validating OCT [176], VH-IVUS [134], and NIRS-IVUS [203]. A subset of specimens (up to one-third) would serve as a calibration set to develop a predictive lipid area algorithm, such that appropriate post-processing and photoacoustic signal-to-noise thresholding would produce quantitative imaging results that correlate to corresponding histopathology with the highest sensitivity and specificity. For future clinical compatibility, collection of calibration data sets should be performed in the presence of pulsatile human blood at body temperature and pressures. The remainder would be used in a comprehensive validation set to demonstrate predictive accuracy of IVPA-US for quantitative detection of plaque lipid in an array of lesions. Validation studies should be double-blinded: operators performing *ex vivo* IVPA-US imaging and histopathology of specimens should not have access to algorithms and vice versa. Subsequently, photoacoustic signal similarity between *ex vivo* and *in vivo* imaging should be confirmed in preclinical and small cohort clinical investigations. It is only after this high standard of evidence is reported that we may use IVPA-US in prospective clinical tests to develop new conclusions about human cardiovascular disease and test prognostic value.

It is clear clinical translation will require pathological correlation, but the overarching aim for IVPA-US remains *in vivo* detection of plaques vulnerable to rupture. Our research should be conducted in the context of providing a general clinician with a diagnostic tool to prospectively prevent acute cardiovascular events. This means demonstration of predictive value, not only against histopathology and outside the setting of specific imaging expertise. Acknowledging the strengths of other modalities and integration of two or more complementary techniques may provide the strongest opportunity towards achieving this goal.

APPENDIX A. IVPA-US SYSTEM ARCHITECTURE

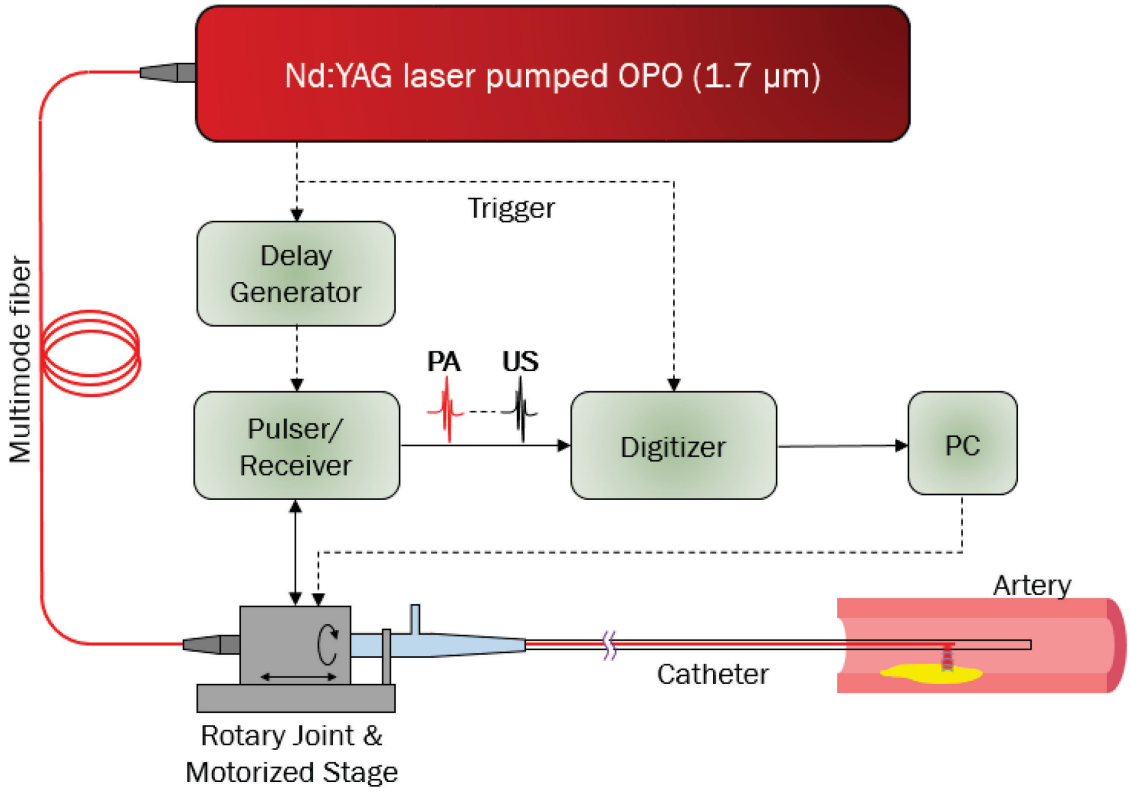

Figure A.1. **IVPA-US system architecture**. Schematic of IVPA imaging system, as described in Chapter 3 and 4. OPO, optical parametric oscillator; PA, photoacoustic; US, ultrasound; PC, personal computer. Adapted from Cao et al. (*Sci Rep*, 2018).

APPENDIX B. ANALYSIS PROTOCOLS

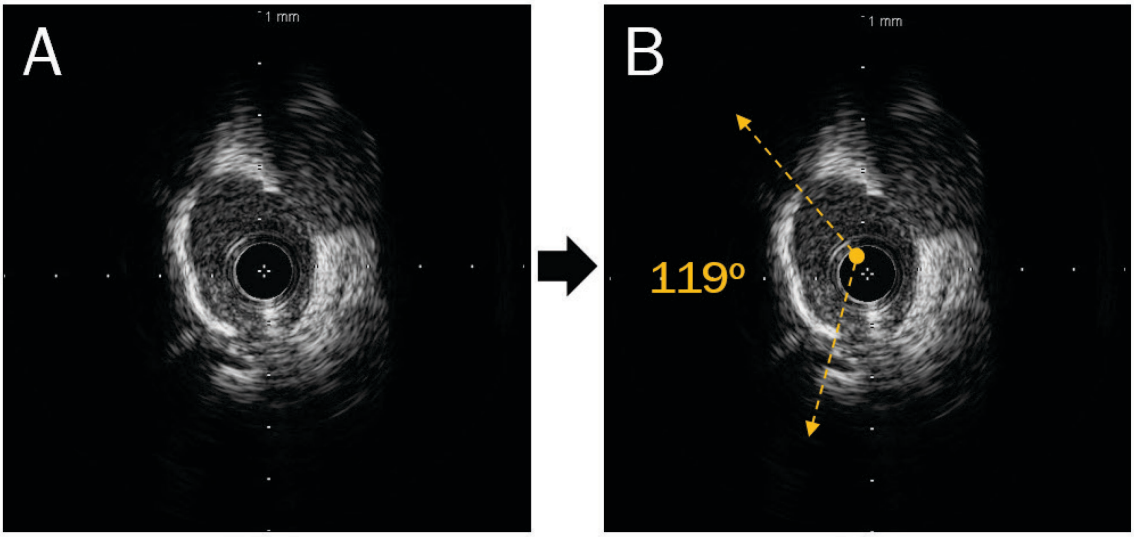

Figure B.1. **IVUS analysis for arc of calcification**. A) IVUS still-frame showing calcification from 6 to 11 o'clock, as indicated by strong echogenicity with acoustic shadowing. B) Arc of calcification, as calculated as the maximum angle of acoustic shadowing within the total pullback length, with each ray bordering the shadow and the vertex at the center of the vessel lumen. Example calculation shows a maximum arc of calcification of 119o. The total length was calculated as continuous frames in which calcification was present.

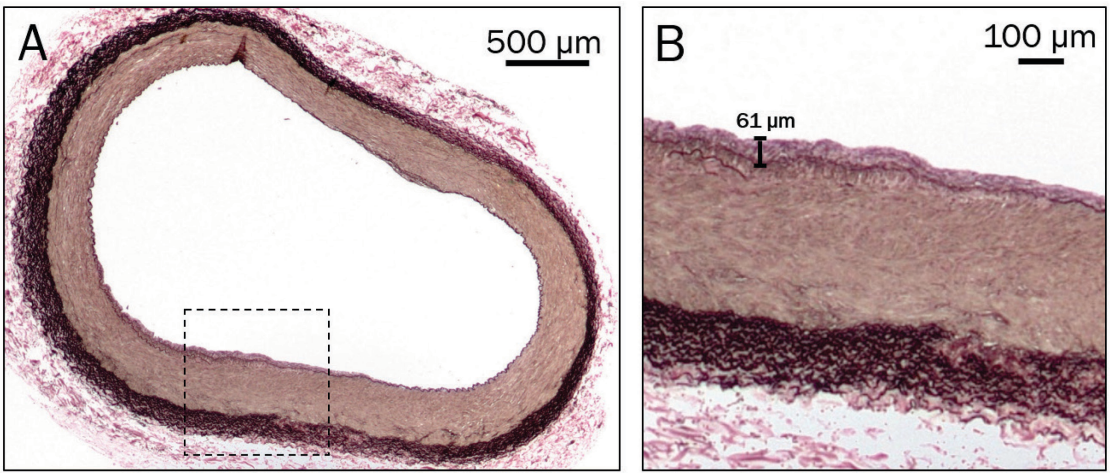

Figure B.2. **Histology analysis for maximal intimal thickness**. A) Veorhoeff-Van Gieson stained section from an Ossabaw swine, with inset shown in (B) magnified. B) Maximal intimal thickness was defined as the thickest neointima (from internal elastic lamina to the lumen) at any point in the vessel. Example calculation shows a maximal intimal thickness of 61 µm.

APPENDIX C. PHYSIOLOGICAL BUFFER SOLUTIONS

Table C.1. **EH Storage Media**

Components	Concentration (mM)	1000 mL	500 mL
$CaCl_2$	2.0	20 ml of 0.1 M	10 ml of 0.1 M
NaCl	135	135 ml of 1.0 M	67.5 ml of 1.0 M
$MgCl_2$	1	10 ml of 0.1 M	5 ml of 0.1 M
KCl	5	50 ml of 0.1 M	25 ml of 0.1 M
KH_2PO_4	0.44	4.4 ml of 0.1 M	2.2 ml of 0.1 M
Na_2HPO_4	0.34	3.4 ml of 0.1 M	1.7 ml of 0.1 M
$NaHCO_3$	2.6	26 ml of 0.1 M	13 ml of 0.1 M
Amino Acids	1X	20 ml of 50X	10 ml of 50X
Vitamins	1X	10 ml of 100X	5 ml of 100X
Phenol Red	0.001%	2 ml of 0.5%	1 ml of 0.5%
HEPES	20	20 ml of 1.0 M	10 ml of 1.0 M
Glucose	10	1.8 g	0.9 g
pH	7.4	with NaOH	with NaOH
PS	1%	10 ml	5 ml
Horse Serum	2%	20 ml	10 ml

EH storage medium is type of Eagle's Minimal Essential Medium (EMEM), but also has HEPES as a pH buffer, so that bubbling the solution with O_2 is not necessary for maintenance of pH.

REFERENCES

[1] V. Kumar, A. K. Abbas, and J. C. Aster, "Blood Vessels," in *Robbins & Cotran Pathologic Basis of Disease*, 9th ed Philadelphia, PA: Saunders/Elsevier Health Sciences, 2014, pp. 483-522.

[2] A. J. Lusis, "Atherosclerosis," *Nature,* vol. 407, pp. 233-41, 2000.

[3] A. S. Go, D. Mozaffarian, V. L. Roger, E. J. Benjamin, J. D. Berry, M. J. Blaha, S. Dai, E. S. Ford, C. S. Fox, S. Franco, H. J. Fullerton, C. Gillespie, S. M. Hailpern, J. A. Heit, V. J. Howard, M. D. Huffman, S. E. Judd, B. M. Kissela, S. J. Kittner, D. T. Lackland, J. H. Lichtman, L. D. Lisabeth, R. H. Mackey, D. J. Magid, G. M. Marcus, A. Marelli, D. B. Matchar, D. K. McGuire, E. R. Mohler, 3rd, C. S. Moy, M. E. Mussolino, R. W. Neumar, G. Nichol, D. K. Pandey, N. P. Paynter, M. J. Reeves, P. D. Sorlie, J. Stein, A. Towfighi, T. N. Turan, S. S. Virani, N. D. Wong, D. Woo, M. B. Turner, C. American Heart Association Statistics, and S. Stroke Statistics, "Heart disease and stroke statistics--2014 update: a report from the American Heart Association," *Circulation,* vol. 129, pp. e28-e292, 2014.

[4] B. Cannon, "Cardiovascular disease: Biochemistry to behaviour," *Nature,* vol. 493, pp. S2-S3, 2013.

[5] S. Mendis, S. Davis, and B. Norrving, "Organizational update: the world health organization global status report on noncommunicable diseases 2014; one more landmark step in the combat against stroke and vascular disease," *Stroke,* vol. 46, pp. e121-2, 2015.

[6] H. D. White and D. P. Chew, "Acute myocardial infarction," *Lancet,* vol. 372, pp. 570-84, 2008.

[7] V. Fuster, L. Badimon, J. J. Badimon, and J. H. Chesebro, "The pathogenesis of coronary artery disease and the acute coronary syndromes (1)," *N Engl J Med,* vol. 326, pp. 242-50, 1992.

[8] V. Fuster, L. Badimon, J. J. Badimon, and J. H. Chesebro, "The pathogenesis of coronary artery disease and the acute coronary syndromes (2)," *N Engl J Med,* vol. 326, pp. 310-8, 1992.

[9] P. Libby, "Vascular biology of atherosclerosis: overview and state of the art," *Am J Cardiol,* vol. 91, pp. 3A-6A, 2003.

[10] C. K. Glass and J. L. Witztum, "Atherosclerosis: The Road Ahead," *Cell,* vol. 104, pp. 503-16, 2001.

[11] P. Libby, P. M. Ridker, and G. K. Hansson, "Progress and challenges in translating the biology of atherosclerosis," *Nature,* vol. 473, pp. 317-325, 2011.

[12] P. Libby, P. M. Ridker, and G. K. Hansson, "Inflammation in atherosclerosis: from pathophysiology to practice," *J Am Coll Cardiol,* vol. 54, pp. 2129-38, 2009.

[13] H. A. Sattar, "Vascular Pathology," in *Fundamentals of Pathology*, ed Chicago, IL: Pathoma.com, 2011, pp. 65-71.

[14] J. Plutzky, "The vascular biology of atherosclerosis," *Am J Med,* vol. 115 Suppl 8A, pp. 55S-61S, 2003.

[15] E. Falk, M. Nakano, J. F. Bentzon, A. V. Finn, and R. Virmani, "Update on acute coronary syndromes: the pathologists' view," *European Heart Journal,* vol. 34, pp. 719-28, 2013.

[16] J. A. Schaar, J. E. Muller, E. Falk, R. Virmani, V. Fuster, P. W. Serruys, A. Colombo, C. Stefanadis, S. Ward Casscells, P. R. Moreno, A. Maseri, and A. F. van der Steen, "Terminology for high-risk and vulnerable coronary artery plaques. Report of a meeting on the vulnerable plaque, June 17 and 18, 2003, Santorini, Greece," *European Heart Journal,* vol. 25, pp. 1077-82, 2004.

[17] J. E. Muller, G. H. Tofler, and P. H. Stone, "Circadian variation and triggers of onset of acute cardiovascular disease," *Circulation,* vol. 79, pp. 733-43, 1989.

[18] M. Naghavi, P. Libby, E. Falk, S. W. Casscells, S. Litovsky, J. Rumberger, J. J. Badimon, C. Stefanadis, P. Moreno, G. Pasterkamp, Z. Fayad, P. H. Stone, S. Waxman, P. Raggi, M. Madjid, A. Zarrabi, A. Burke, C. Yuan, P. J. Fitzgerald, D. S. Siscovick, C. L. de Korte, M. Aikawa, K. E. Juhani Airaksinen, G. Assmann, C. R. Becker, J. H. Chesebro, A. Farb, Z. S. Galis, C. Jackson, I. K. Jang, W. Koenig, R. A. Lodder, K. March, J. Demirovic, M. Navab, S. G. Priori, M. D. Rekhter, R. Bahr, S. M. Grundy, R. Mehran, A. Colombo, E. Boerwinkle, C. Ballantyne, W. Insull, Jr., R. S. Schwartz, R. Vogel, P. W. Serruys, G. K. Hansson, D. P. Faxon, S. Kaul, H. Drexler, P. Greenland, J. E. Muller, R. Virmani, P. M. Ridker, D. P. Zipes, P. K. Shah, and J. T. Willerson, "From vulnerable plaque to vulnerable patient: a call for new definitions and risk assessment strategies: Part I," *Circulation,* vol. 108, pp. 1664-72, 2003.

[19] H. C. Stary, A. B. Chandler, R. E. Dinsmore, V. Fuster, S. Glagov, W. Insull, Jr., M. E. Rosenfeld, C. J. Schwartz, W. D. Wagner, and R. W. Wissler, "A definition of advanced types of atherosclerotic lesions and a histological classification of atherosclerosis. A report from the Committee on Vascular Lesions of the Council on Arteriosclerosis, American Heart Association," *Circulation,* vol. 92, pp. 1355-74, 1995.

[20] H. C. Stary, "Natural history and histological classification of atherosclerotic lesions: an update," *Arterioscler Thromb Vasc Biol,* vol. 20, pp. 1177-8, 2000.

[21] R. Virmani, F. D. Kolodgie, A. P. Burke, A. Farb, and S. M. Schwartz, "Lessons from sudden coronary death: a comprehensive morphological classification scheme for atherosclerotic lesions," *Arterioscler Thromb Vasc Biol,* vol. 20, pp. 1262-75, 2000.

[22] F. D. Kolodgie, A. P. Burke, A. Farb, H. K. Gold, J. Yuan, J. Narula, A. V. Finn, and R. Virmani, "The thin-cap fibroatheroma: a type of vulnerable plaque: the major precursor lesion to acute coronary syndromes," *Curr Opin Cardiol,* vol. 16, pp. 285-92, 2001.

[23] K. Yahagi, F. D. Kolodgie, F. Otsuka, A. V. Finn, H. R. Davis, M. Joner, and R. Virmani, "Pathophysiology of native coronary, vein graft, and in-stent atherosclerosis," *Nat Rev Cardiol,* vol. 13, pp. 79-98, 2016.

[24] P. R. Moreno, "Vulnerable plaque: definition, diagnosis, and treatment," *Cardiol Clin,* vol. 28, pp. 1-30, 2010.

[25] J. Narula and J. C. Kovacic, "Putting TCFA in clinical perspective," *J Am Coll Cardiol,* vol. 64, pp. 681-3, 2014.

[26] P. R. Moreno, "The high-risk thin-cap fibroatheroma: a new kid on the block," *Circ Cardiovasc Interv,* vol. 2, pp. 500-2, 2009.

[27] M. Naghavi, P. Libby, E. Falk, S. W. Casscells, S. Litovsky, J. Rumberger, J. J. Badimon, C. Stefanadis, P. Moreno, G. Pasterkamp, Z. Fayad, P. H. Stone, S. Waxman, P. Raggi, M. Madjid, A. Zarrabi, A. Burke, C. Yuan, P. J. Fitzgerald, D. S. Siscovick, C. L. de Korte, M. Aikawa, K. E. Airaksinen, G. Assmann, C. R. Becker, J. H. Chesebro, A. Farb, Z. S. Galis, C. Jackson, I. K. Jang, W. Koenig, R. A. Lodder, K. March, J. Demirovic, M. Navab, S. G. Priori, M. D. Rekhter, R. Bahr, S. M. Grundy, R. Mehran, A. Colombo, E. Boerwinkle, C. Ballantyne, W. Insull, Jr., R. S. Schwartz, R. Vogel, P. W. Serruys, G. K. Hansson, D. P. Faxon, S. Kaul, H. Drexler, P. Greenland, J. E. Muller, R. Virmani, P. M. Ridker, D. P. Zipes, P. K. Shah, and J. T. Willerson, "From vulnerable plaque to vulnerable patient: a call for new definitions and risk assessment strategies: Part II," *Circulation,* vol. 108, pp. 1772-8, 2003.

[28] A. V. Finn, M. Nakano, J. Narula, F. D. Kolodgie, and R. Virmani, "Concept of vulnerable/unstable plaque," *Arterioscler Thromb Vasc Biol,* vol. 30, pp. 1282-92, 2010.

[29] P. Schoenhagen, K. M. Ziada, D. G. Vince, S. E. Nissen, and E. M. Tuzcu, "Arterial remodeling and coronary artery disease: the concept of "dilated" versus "obstructive" coronary atherosclerosis," *J Am Coll Cardiol,* vol. 38, pp. 297-306, 2001.

[30] C. K. Zarins, E. Weisenberg, G. Kolettis, R. Stankunavicius, and S. Glagov, "Differential enlargement of artery segments in response to enlarging atherosclerotic plaques," *J Vasc Surg,* vol. 7, pp. 386-94, 1988.

[31] M. Takano, K. Mizuno, K. Okamatsu, S. Yokoyama, T. Ohba, and S. Sakai, "Mechanical and structural characteristics of vulnerable plaques: analysis by coronary angioscopy and intravascular ultrasound," *J Am Coll Cardiol,* vol. 38, pp. 99-104, 2001.

[32] R. Virmani, "Are Our Tools for the Identification of TCFA Ready and Do We Know Them?," *JACC Cardiovasc Imaging,* vol. 4, pp. 656-658, 2011.

[33] A. P. Burke, A. Farb, G. T. Malcom, Y. H. Liang, J. Smialek, and R. Virmani, "Coronary risk factors and plaque morphology in men with coronary disease who died suddenly," *N Engl J Med,* vol. 336, pp. 1276-82, 1997.

[34] J. Narula, M. Nakano, R. Virmani, F. D. Kolodgie, R. Petersen, R. Newcomb, S. Malik, V. Fuster, and A. V. Finn, "Histopathologic characteristics of atherosclerotic coronary disease and implications of the findings for the invasive and noninvasive detection of vulnerable plaques," *J Am Coll Cardiol,* vol. 61, pp. 1041-51, 2013.

[35] H. M. Loree, R. D. Kamm, R. G. Stringfellow, and R. T. Lee, "Effects of fibrous cap thickness on peak circumferential stress in model atherosclerotic vessels," *Circ Res,* vol. 71, pp. 850-8, 1992.

[36] S. Waxman, F. Ishibashi, and J. E. Muller, "Detection and treatment of vulnerable plaques and vulnerable patients: novel approaches to prevention of coronary events," *Circulation,* vol. 114, pp. 2390-411, 2006.

[37] B. D. MacNeill, I. K. Jang, B. E. Bouma, N. Iftimia, M. Takano, H. Yabushita, M. Shishkov, C. R. Kauffman, S. L. Houser, H. T. Aretz, D. DeJoseph, E. F. Halpern, and G. J. Tearney, "Focal and multi-focal plaque macrophage distributions in patients with acute and stable presentations of coronary artery disease," *J Am Coll Cardiol,* vol. 44, pp. 972-9, 2004.

[38] P. Libby, "Changing concepts of atherogenesis," *J Intern Med,* vol. 247, pp. 349-58, 2000.

[39] J. Chen, C. H. Tung, U. Mahmood, V. Ntziachristos, R. Gyurko, M. C. Fishman, P. L. Huang, and R. Weissleder, "In vivo imaging of proteolytic activity in atherosclerosis," *Circulation,* vol. 105, pp. 2766-71, 2002.

[40] M. J. Davies, "The pathophysiology of acute coronary syndromes," *Heart,* vol. 83, pp. 361-6, 2000.

[41] R. Virmani, A. P. Burke, A. Farb, and F. D. Kolodgie, "Pathology of the vulnerable plaque," *J Am Coll Cardiol,* vol. 47, pp. C13-8, 2006.

[42] R. Virmani, A. Burke, A. Farb, F. D. Kolodgie, A. V. Finn, and H. K. Gold, "Pathology of the vulnerable plaque," in *The Vulnerable Plaque*, R. Waksman, P. W. Serruys, and J. Schaar, Eds., 2 ed Boca Raton, FL: CRC Press, 2007, pp. 13-29.

[43] C. V. Felton, D. Crook, M. J. Davies, and M. F. Oliver, "Relation of plaque lipid composition and morphology to the stability of human aortic plaques," *Arterioscler Thromb Vasc Biol,* vol. 17, pp. 1337-45, 1997.

[44] P. R. Moreno, V. H. Bernardi, J. Lopez-Cuellar, A. M. Murcia, I. F. Palacios, H. K. Gold, R. Mehran, S. K. Sharma, Y. Nemerson, V. Fuster, and J. T. Fallon, "Macrophages, smooth muscle cells, and tissue factor in unstable angina. Implications for cell-mediated thrombogenicity in acute coronary syndromes," *Circulation,* vol. 94, pp. 3090-7, 1996.

[45] F. D. Kolodgie, R. Virmani, A. P. Burke, A. Farb, D. K. Weber, R. Kutys, A. V. Finn, and H. K. Gold, "Pathologic assessment of the vulnerable human coronary plaque," *Heart,* vol. 90, pp. 1385-91, 2004.

[46] A. J. Taylor, C. N. Merz, and J. E. Udelson, "34th Bethesda Conference: Executive summary--can atherosclerosis imaging techniques improve the detection of patients at risk for ischemic heart disease?," *J Am Coll Cardiol,* vol. 41, pp. 1860-2, 2003.

[47] K. L. Gould, K. Lipscomb, and G. W. Hamilton, "Physiologic basis for assessing critical coronary stenosis. Instantaneous flow response and regional distribution during coronary hyperemia as measures of coronary flow reserve," *Am J Cardiol,* vol. 33, pp. 87-94, 1974.

[48] G. Niccoli, G. G. Stefanini, D. Capodanno, F. Crea, J. A. Ambrose, and R. Berg, "Are the culprit lesions severely stenotic?," *JACC Cardiovasc Imaging,* vol. 6, pp. 1108-14, 2013.

[49] R. Virmani, A. P. Burke, F. D. Kolodgie, A. Farb, A. V. Finn, and H. Gold, "Pathology and pathophysiology of coronary atherosclerotic plaques," in *CT of the Heart*, ed New York, NY: Humana Press, 2005, pp. 351-364.

[50] P. R. Moreno, K. R. Purushothaman, M. Sirol, A. P. Levy, and V. Fuster, "Neovascularization in human atherosclerosis," *Circulation,* vol. 113, pp. 2245-52, 2006.

[51] P. R. Moreno, R. Purushothaman, V. Fuster, D. Echeverri, H. Truszczynska, S. K. Sharma, J. J. Badimon, and W. N. O'Connor, "Plaque neovascularization is increased in ruptured atherosclerotic lesions of human aorta - Implications for plaque vulnerability," *Circulation,* vol. 110, pp. 2032-2038, 2004.

[52] O. J. de Boer, A. C. van der Wal, P. Teeling, and A. E. Becker, "Leucocyte recruitment in rupture prone regions of lipid-rich plaques: a prominent role for neovascularization?," *Cardiovasc Res,* vol. 41, pp. 443-9, 1999.

[53] S. Kaul and G. A. Diamond, "Improved prospects for IVUS in identifying vulnerable plaques?," *JACC Cardiovasc Imaging,* vol. 5, pp. S106-10, 2012.

[54] H. M. Garcia-Garcia, N. Gonzalo, J. F. Granada, E. Regar, and P. W. Serruys, "Diagnosis and treatment of coronary vulnerable plaques," *Expert Rev Cardiovasc Ther,* vol. 6, pp. 209-22, 2008.

[55] M. J. Bom, D. J. van der Heijden, E. Kedhi, J. van der Heyden, M. Meuwissen, P. Knaapen, S. A. J. Timmer, and N. van Royen, "Early Detection and Treatment of the Vulnerable Coronary Plaque: Can We Prevent Acute Coronary Syndromes?," *Circ Cardiovasc Imaging,* vol. 10, 2017.

[56] S. Honda, Y. Kataoka, T. Kanaya, T. Noguchi, H. Ogawa, and S. Yasuda, "Characterization of coronary atherosclerosis by intravascular imaging modalities," *Cardiovasc Diagn Ther,* vol. 6, pp. 368-81, 2016.

[57] T. Ma, B. Zhou, T. K. Hsiai, and K. K. Shung, "A Review of Intravascular Ultrasound-Based Multimodal Intravascular Imaging: The Synergistic Approach to Characterizing Vulnerable Plaques," *Ultrason Imaging,* 2015.

[58] C. V. Bourantas, F. A. Jaffer, F. J. Gijsen, G. van Soest, S. P. Madden, B. K. Courtney, A. M. Fard, E. Tenekecioglu, Y. Zeng, A. F. van der Steen, S. Emelianov, J. Muller, P. H. Stone, L. Marcu, G. J. Tearney, and P. W. Serruys, "Hybrid intravascular imaging: recent advances, technical considerations, and current applications in the study of plaque pathophysiology," *European Heart Journal,* 2016.

[59] B. A. Danek, A. Karatasakis, R. D. Madder, J. E. Muller, S. Madden, S. Banerjee, and E. S. Brilakis, "Experience with the Multimodality Near-Infrared Spectroscopy/Intravascular Ultrasound Coronary Imaging System: Principles, Clinical Experience, and Ongoing Studies," *Curr Cardiovasc Imaging Rep,* vol. 9, 2016.

[60] M. Michail, P. W. Serruys, R. Stettler, T. Crake, R. Torii, E. Tenekecioglu, Y. Zeng, Y. Onuma, A. Mathur, and C. V. Bourantas, "Intravascular multimodality imaging: feasibility and role in the evaluation of coronary plaque pathology," *Eur Heart J Cardiovasc Imaging,* vol. 18, pp. 613-620, 2017.

[61] G. van Soest, L. Marcu, B. E. Bouma, and E. Regar, "Intravascular imaging for characterization of coronary atherosclerosis," *Current Opinion in Biomedical Engineering,* vol. 3, pp. 1-12, 2017.

[62] J. W. Verjans, E. A. Osborn, G. J. Ughi, M. A. Calfon Press, E. Hamidi, A. P. Antoniadis, M. I. Papafaklis, M. F. Conrad, P. Libby, P. H. Stone, R. P. Cambria, G. J. Tearney, and F. A. Jaffer, "Targeted Near-Infrared Fluorescence Imaging of Atherosclerosis: Clinical and Intracoronary Evaluation of Indocyanine Green," *JACC Cardiovasc Imaging,* vol. 9, pp. 1087-1095, 2016.

[63] H. Yoo, J. W. Kim, M. Shishkov, E. Namati, T. Morse, R. Shubochkin, J. R. McCarthy, V. Ntziachristos, B. E. Bouma, F. A. Jaffer, and G. J. Tearney, "Intra-arterial catheter for simultaneous microstructural and molecular imaging in vivo," *Nature Medicine,* vol. 17, p. 1680, 2011.

[64] S. Kim, M. W. Lee, T. S. Kim, J. W. Song, H. S. Nam, H. S. Cho, S.-J. Jang, J. Ryu, D. J. Oh, D.-G. Gweon, S. H. Park, K. Park, W.-Y. Oh, H. Yoo, and J. W. Kim, "Intracoronary dual-modal optical coherence tomography-near-infrared fluorescence structural–molecular imaging with a clinical dose of indocyanine green for the assessment of high-risk plaques and stent-associated inflammation in a beating coronary artery," *European Heart Journal,* vol. 37, pp. 2833-2844, 2016.

[65] F. A. Jaffer, M. A. Calfon, A. Rosenthal, G. Mallas, R. N. Razansky, A. Mauskapf, R. Weissleder, P. Libby, and V. Ntziachristos, "Two-dimensional intravascular near-infrared fluorescence molecular imaging of inflammation in atherosclerosis and stent-induced vascular injury," *J Am Coll Cardiol,* vol. 57, pp. 2516-26, 2011.

[66] H. Wang, J. A. Gardecki, G. J. Ughi, P. V. Jacques, E. Hamidi, and G. J. Tearney, "Ex vivo catheter-based imaging of coronary atherosclerosis using multimodality OCT and NIRAF excited at 633 nm," *Biomed Opt Express,* vol. 6, pp. 1363-1375, 2015.

[67] G. J. Ughi, H. Wang, E. Gerbaud, J. A. Gardecki, A. M. Fard, E. Hamidi, P. Vacas-Jacques, M. Rosenberg, F. A. Jaffer, and G. J. Tearney, "Clinical Characterization of Coronary Atherosclerosis With Dual-Modality OCT and Near-Infrared Autofluorescence Imaging," *JACC Cardiovasc Imaging,* 2016.

[68] H. Fatakdawala, D. Gorpas, J. W. Bishop, J. Bec, D. Ma, J. A. Southard, K. B. Margulies, and L. Marcu, "Fluorescence Lifetime Imaging Combined with Conventional Intravascular Ultrasound for Enhanced Assessment of Atherosclerotic Plaques: an Ex Vivo Study in Human Coronary Arteries," *J Cardiovasc Transl Res,* vol. 8, pp. 253-263, 2015.

[69] D. Gorpas, H. Fatakdawala, J. Bec, D. Ma, D. R. Yankelevich, J. Qi, and L. Marcu, "Fluorescence Lifetime Imaging and Intravascular Ultrasound: Co-Registration Study Using Ex Vivo Human Coronaries," *IEEE Trans Med Imaging,* vol. 34, pp. 156-166, 2015.

[70] J. Bec, D. M. Ma, D. R. Yankelevich, J. Liu, W. T. Ferrier, J. Southard, and L. Marcu, "Multispectral fluorescence lifetime imaging system for intravascular diagnostics with ultrasound guidance: in vivo validation in swine arteries," *Journal of Biophotonics,* vol. 7, pp. 281-5, 2014.

[71] J. Bec, J. E. Phipps, D. Gorpas, D. Ma, H. Fatakdawala, K. B. Margulies, J. A. Southard, and L. Marcu, "In vivo label-free structural and biochemical imaging of coronary arteries using an integrated ultrasound and multispectral fluorescence lifetime catheter system," *Sci Rep,* vol. 7, p. 8960, 2017.

[72] T. J. Ryan, "The coronary angiogram and its seminal contributions to cardiovascular medicine over five decades," *Circulation,* vol. 106, pp. 752-6, 2002.

[73] P. J. de Feyter, P. W. Serruys, K. Nieman, N. Mollet, F. Cademartiri, R. J. van Geuns, C. Slager, A. F. van der Steen, R. Krams, J. A. Schaar, P. Wielopolski, P. M. Pattynama, A. Arampatzis, A. van der Lugt, E. Regar, J. Ligthart, and P. Smits, "Imaging of coronary atherosclerosis and identification of the vulnerable plaque," *Neth Heart J,* vol. 11, pp. 347-358, 2003.

[74] S. E. Nissen and P. Yock, "Intravascular ultrasound: novel pathophysiological insights and current clinical applications," *Circulation,* vol. 103, pp. 604-16, 2001.

[75] G. M. Julio Nunez, "Coronary Angiography, Too Far to be a Gold Standard Technique for Identifying a Vulnerable Plaque," *J Clin Exp Cardiolog,* vol. 02, 2011.

[76] S. E. Nissen, "Pathobiology, not angiography, should guide management in acute coronary syndrome/non-ST-segment elevation myocardial infarction: the non-interventionist's perspective," *J Am Coll Cardiol,* vol. 41, pp. 103S-112S, 2003.

[77] G. Minana, "Coronary Angiography, Too Far to be a Gold Standard Technique for Identifying a Vulnerable Plaque," *J Clin Exp Cardiolog,* 2011.

[78] S. G. Ellis, "Role of Coronary Angiography," in *Atherothrombosis and Coronary Artery Disease*, V. Fuster, E. J. Topol, and E. G. Nabel, Eds., ed Philadelphia, PA: Lippincott Williams & Wilkins, 2004, pp. 1340-1362.

[79] E. J. Topol and S. E. Nissen, "Our Preoccupation With Coronary Luminology: The Dissociation Between Clinical and Angiographic Findings in Ischemic Heart Disease," *Circulation,* vol. 92, pp. 2333-2342, 1995.

[80] J. A. Ambrose, M. A. Tannenbaum, D. Alexopoulos, C. E. Hjemdahlmonsen, J. Leavy, M. Weiss, S. Borrico, R. Gorlin, and V. Fuster, "Angiographic Progression of Coronary Artery Disease and the Development of Myocardial Infarction," *J Am Coll Cardiol,* vol. 12, pp. 56-62, 1988.

[81] W. C. Roberts and A. A. Jones, "Quantitation of coronary arterial narrowing at necropsy in sudden coronary death: analysis of 31 patients and comparison with 25 control subjects," *Am J Cardiol,* vol. 44, pp. 39-45, 1979.

[82] W. C. Little, M. Constantinescu, R. J. Applegate, M. A. Kutcher, M. T. Burrows, F. R. Kahl, and W. P. Santamore, "Can Coronary Angiography Predict the Site of a Subsequent Myocardial-Infarction in Patients with Mild-to-Moderate Coronary-Artery Disease," *Circulation,* vol. 78, pp. 1157-1166, 1988.

[83] J. A. Schaar, F. Mastik, E. Regar, C. A. den Uil, F. J. Gijsen, J. J. Wentzel, P. W. Serruys, and A. F. van der Stehen, "Current diagnostic modalities for vulnerable plaque detection," *Curr Pharm Des,* vol. 13, pp. 995-1001, 2007.

[84] P. Yock, E. L. Johnson, and D. T. Linker, "Intravascular ultrasound: Development and clinical potential," *Am J Cardiol,* vol. 2, pp. 185-193, 1988.

[85] A. Caixeta, A. Maehara, and G. S. Mintz, "Intravascular Ultrasound: Principles, Image Interpretation, and Clinical Applications," in *Interventional Cardiology: Principles and Practice*, C. Di Mario, G. Dangas, and P. Barlis, Eds., ed Hoboken, NJ: Wiley-Blackwell, 2011, pp. 145-171.

[86] A. Maehara, G. S. Mintz, and N. J. Weissman, "Intravascular Ultrasound : Principles and Clinical Applications," in *Practice of Clinical Echocardiography*, C. M. Otto, Ed., ed Philadelphia, PA: Elsevier Health Sciences, 2012, pp. 130-142.

[87] G. S. Mintz, J. J. Popma, A. D. Pichard, K. M. Kent, L. F. Salter, Y. C. Chuang, J. Griffin, and M. B. Leon, "Intravascular ultrasound predictors of restenosis after percutaneous transcatheter coronary revascularization," *J Am Coll Cardiol,* vol. 27, pp. 1678-87, 1996.

[88] F. Schiele, N. Meneveau, A. Vuillemenot, D. D. Zhang, S. Gupta, M. Mercier, N. Danchin, B. Bertrand, and J. P. Bassand, "Impact of intravascular ultrasound guidance in stent deployment on 6-month restenosis rate: a multicenter, randomized study comparing two strategies--with and without intravascular ultrasound guidance. RESIST Study Group. REStenosis after Ivus guided STenting," *J Am Coll Cardiol,* vol. 32, pp. 320-8, 1998.

[89] T. Kubo, A. Maehara, G. S. Mintz, H. Doi, K. Tsujita, S. Y. Choi, O. Katoh, K. Nasu, A. Koenig, M. Pieper, J. H. Rogers, W. Wijns, D. Bose, M. P. Margolis, J. W. Moses, G. W. Stone, and M. B. Leon, "The dynamic nature of coronary artery lesion morphology assessed by serial virtual histology intravascular ultrasound tissue characterization," *J Am Coll Cardiol,* vol. 55, pp. 1590-7, 2010.

[90] J. M. Tobis, J. Mallery, D. Mahon, K. Lehmann, P. Zalesky, J. Griffith, J. Gessert, M. Moriuchi, M. McRae, M. L. Dwyer, and et al., "Intravascular ultrasound imaging of human coronary arteries in vivo. Analysis of tissue characterizations with comparison to in vitro histological specimens," *Circulation,* vol. 83, pp. 913-26, 1991.

[91] G. W. Stone, J. M. Hodgson, F. G. St Goar, A. Frey, H. Mudra, H. Sheehan, and T. J. Linnemeier, "Improved procedural results of coronary angioplasty with intravascular ultrasound-guided balloon sizing: the CLOUT Pilot Trial. Clinical Outcomes With Ultrasound Trial (CLOUT) Investigators," *Circulation,* vol. 95, pp. 2044-52, 1997.

[92] A. Abizaid, A. D. Pichard, G. S. Mintz, A. S. Abizaid, M. W. Klutstein, L. F. Satler, R. Mehran, B. Leiboff, K. M. Kent, and M. B. Leon, "Acute and long-term results of an intravascular ultrasound-guided percutaneous transluminal coronary angioplasty/provisional stent implantation strategy," *Am J Cardiol,* vol. 84, pp. 1298-303, 1999.

[93] P. J. Fitzgerald, A. Oshima, M. Hayase, J. A. Metz, S. R. Bailey, D. S. Baim, M. W. Cleman, E. Deutsch, D. J. Diver, M. B. Leon, J. W. Moses, S. N. Oesterle, P. A. Overlie, C. J. Pepine, R. D. Safian, J. Shani, C. A. Simonton, R. W. Smalling, P. S. Teirstein, J. P. Zidar, A. C. Yeung, R. E. Kuntz, and P. G. Yock, "Final results of the Can Routine Ultrasound Influence Stent Expansion (CRUISE) study," *Circulation,* vol. 102, pp. 523-30, 2000.

[94] C. Briguori, A. Anzuini, F. Airoldi, G. Gimelli, T. Nishida, M. Adamian, N. Corvaja, C. Di Mario, and A. Colombo, "Intravascular ultrasound criteria for the assessment of the functional significance of intermediate coronary artery stenoses and comparison with fractional flow reserve," *Am J Cardiol,* vol. 87, pp. 136-41, 2001.

[95] A. A. Fassa, K. Wagatsuma, S. T. Higano, V. Mathew, G. W. Barsness, R. J. Lennon, D. R. Holmes, Jr., and A. Lerman, "Intravascular ultrasound-guided treatment for angiographically indeterminate left main coronary artery disease: a long-term follow-up study," *J Am Coll Cardiol,* vol. 45, pp. 204-11, 2005.

[96] J. A. Kobashigawa, J. M. Tobis, R. C. Starling, E. M. Tuzcu, A. L. Smith, H. A. Valantine, A. C. Yeung, M. R. Mehra, H. Anzai, B. T. Oeser, K. H. Abeywickrama, J. Murphy, and N. Cretin, "Multicenter intravascular ultrasound validation study among heart transplant recipients: outcomes after five years," *J Am Coll Cardiol,* vol. 45, pp. 1532-7, 2005.

[97] J. M. Hodgson, "If You Want to Stent … Do Intravascular Ultrasound!," *JACC Cardiovasc Imaging,* vol. 3, pp. 818-820, 2010.

[98] S. J. Kang, J. Y. Lee, J. M. Ahn, G. S. Mintz, W. J. Kim, D. W. Park, S. C. Yun, S. W. Lee, Y. H. Kim, C. W. Lee, S. W. Park, and S. J. Park, "Validation of intravascular ultrasound-derived parameters with fractional flow reserve for assessment of coronary stenosis severity," *Circ Cardiovasc Interv,* vol. 4, pp. 65-71, 2011.

[99] G. N. Levine, E. R. Bates, J. C. Blankenship, S. R. Bailey, J. A. Bittl, B. Cercek, C. E. Chambers, S. G. Ellis, R. A. Guyton, S. M. Hollenberg, U. N. Khot, R. A. Lange, L. Mauri, R. Mehran, I. D. Moussa, D. Mukherjee, B. K. Nallamothu, and H. H. Ting, "2011 ACCF/AHA/SCAI Guideline for Percutaneous Coronary Intervention: A Report of the American College of Cardiology Foundation/American Heart Association Task Force on Practice Guidelines and the Society for Cardiovascular Angiography and Interventions," *J Am Coll Cardiol,* vol. 58, pp. e44-e122, 2011.

[100] G. W. Stone, A. Maehara, A. J. Lansky, B. de Bruyne, E. Cristea, G. S. Mintz, R. Mehran, J. McPherson, N. Farhat, S. P. Marso, H. Parise, B. Templin, R. White, Z. Zhang, and P. W. Serruys, "A Prospective Natural-History Study of Coronary Atherosclerosis," *N Engl J Med,* vol. 364, pp. 226-235, 2011.

[101] B. Witzenbichler, A. Maehara, G. Weisz, F.-J. Neumann, M. Rinaldi, D. C. Metzger, T. Henry, D. Cox, P. Duffy, B. Brodie, T. Stuckey, E. Mazzaferri, K. Xu, R. Mehran, H. Parise, G. Mintz, and G. Stone, "TCT-21 Use of IVUS Reduces Stent Thrombosis: Results from the Prospective, multicenter ADAPT-DES Study," *J Am Coll Cardiol,* vol. 60, 2012.

[102] Y. Zhang, V. Farooq, H. M. Garcia-Garcia, C. V. Bourantas, N. Tian, S. Dong, M. Li, S. Yang, P. W. Serruys, and S. L. Chen, "Comparison of intravascular ultrasound versus angiography-guided drug-eluting stent implantation: a meta-analysis of one randomised trial and ten observational studies involving 19,619 patients," *EuroIntervention,* vol. 8, pp. 855-65, 2012.

[103] A. Colombo, P. Hall, S. Nakamura, Y. Almagor, L. Maiello, G. Martini, A. Gaglione, S. L. Goldberg, and J. M. Tobis, "Intracoronary stenting without anticoagulation accomplished with intravascular ultrasound guidance," *Circulation,* vol. 91, pp. 1676-88, 1995.

[104] G. S. Mintz, S. E. Nissen, W. D. Anderson, S. R. Bailey, R. Erbel, P. J. Fitzgerald, F. J. Pinto, K. Rosenfield, R. J. Siegel, E. M. Tuzcu, and P. G. Yock, "American College of Cardiology Clinical Expert Consensus Document on Standards for Acquisition, Measurement and Reporting of Intravascular Ultrasound Studies (IVUS). A report of the American College of Cardiology Task Force on Clinical Expert Consensus Documents," *J Am Coll Cardiol,* vol. 37, pp. 1478-92, 2001.

[105] T. Kume, H. Yasuhiro, and P. J. Fitzgerald, "Intravascular Coronary Ultrasound and Beyond," in *Cardiology: An Illustrated Textbook*, K. Chatterjee, M. Anderson, D. Heistad, and R. E. Kerber, Eds., ed Kathmandu, Nepal Jaypee Brothers Medical Publishers, 2012, pp. 349-381.

[106] F. Ciompi, C. Gatta, O. Pujol, O. Rodriguez-Leor, J. M. Ferre, and P. Radeva, "Reconstruction and Analysis of Intravascular Ultrasound Sequences," in *Recent Advances in Biomedical Signal Processing*, J. M. Górriz, E. W. Lang, and J. Ramírez, Eds., ed Sharjah, UAE: Bentham Science Publishers, 2011, pp. 231-250.

[107] C. Di Mario, G. Gorge, R. Peters, P. Kearney, F. Pinto, D. Hausmann, C. von Birgelen, A. Colombo, H. Mudra, J. Roelandt, and R. Erbel, "Clinical application and image interpretation in intracoronary ultrasound. Study Group on Intracoronary Imaging of the Working Group of Coronary Circulation and of the Subgroup on Intravascular Ultrasound of the Working Group of Echocardiography of the European Society of Cardiology," *European Heart Journal,* vol. 19, pp. 207-29, 1998.

[108] M.-J. Bertrand, P. Lavoie-L'Allier, and J.-C. Tardif, "Near-Infrared Spectroscopy (NIRS): A Novel Tool for Intravascular Coronary Imaging," in *Developments in Near-Infrared Spectroscopy*, K. G. Kyprianidis and J. Skvaril, Eds., ed Rijeka: InTech, 2017, p. Ch. 02.

[109] M. A. Syed and J. M. Hodgson, "Enhanced IVUS: Advances Allowing Higher Resolution and Integrated Devices," *Curr Cardiovasc Imaging Rep,* vol. 9, 2016.

[110] S. I. Negi, R. Didier, H. Ota, M. A. Magalhaes, C. J. Popma, M. R. Kollmer, M. A. Spad, R. Torguson, W. Suddath, L. F. Satler, A. Pichard, and R. Waksman, "Role of near-infrared spectroscopy in intravascular coronary imaging," *Cardiovasc Revasc Med,* vol. 16, pp. 299-305, 2015.

[111] H. M. Garcia-Garcia, N. Kukreja, and P. W. Serruys, "Virtual histology," in *The Vulnerable Plaque*, R. Waksman, P. W. Serruys, and J. Schaar, Eds., 2 ed Boca Raton, FL: CRC Press, 2007, pp. 223-233.

[112] G. A. Rodriguez-Granillo, E. P. McFadden, J. Aoki, C. A. van Mieghem, E. Regar, N. Bruining, and P. W. Serruys, "In vivo variability in quantitative coronary ultrasound and tissue characterization measurements with mechanical and phased-array catheters," *Int J Cardiovasc Imaging,* vol. 22, pp. 47-53, 2006.

[113] E. Sanidas and G. Dangas, "Evolution of intravascular assessment of coronary anatomy and physiology: from ultrasound imaging to optical and flow assessment," *Eur J Clin Invest,* vol. 43, pp. 996-1008, 2013.

[114] E. J. Gussenhoven, C. E. Essed, C. T. Lancee, F. Mastik, P. Frietman, F. C. van Egmond, J. Reiber, H. Bosch, H. van Urk, J. Roelandt, and et al., "Arterial wall characteristics determined by intravascular ultrasound imaging: an in vitro study," *J Am Coll Cardiol,* vol. 14, pp. 947-52, 1989.

[115] R. A. Nishimura, W. D. Edwards, C. A. Warnes, G. S. Reeder, D. R. Holmes, Jr., A. J. Tajik, and P. G. Yock, "Intravascular ultrasound imaging: in vitro validation and pathologic correlation," *J Am Coll Cardiol,* vol. 16, pp. 145-54, 1990.

[116] R. J. Siegel, J. S. Chae, G. Maurer, M. Berlin, and M. C. Fishbein, "Histopathologic correlation of the three-layered intravascular ultrasound appearance of normal adult human muscular arteries," *Am Heart J,* vol. 126, pp. 872-8, 1993.

[117] C. R. Meyer, E. H. Chiang, K. P. Fechner, D. W. Fitting, D. M. Williams, and A. J. Buda, "Feasibility of high-resolution, intravascular ultrasonic imaging catheters," *Radiology,* vol. 168, pp. 113-6, 1988.

[118] D. Velican and C. Velican, "Comparative study on age-related changes and atherosclerotic involvement of the coronary arteries of male and female subjects up to 40 years of age," *Atherosclerosis,* vol. 38, pp. 39-50, 1981.

[119] F. G. St Goar, F. J. Pinto, E. L. Alderman, P. J. Fitzgerald, E. B. Stinson, M. E. Billingham, and R. L. Popp, "Detection of coronary atherosclerosis in young adult hearts using intravascular ultrasound," *Circulation,* vol. 86, pp. 756-63, 1992.

[120] P. J. Fitzgerald, F. G. St Goar, A. J. Connolly, F. J. Pinto, M. E. Billingham, R. L. Popp, and P. G. Yock, "Intravascular ultrasound imaging of coronary arteries. Is three layers the norm?," *Circulation,* vol. 86, pp. 154-8, 1992.

[121] G. S. Mintz, J. J. Popma, A. D. Pichard, K. M. Kent, L. F. Satler, Y. C. Chuang, C. J. Ditrano, and M. B. Leon, "Patterns of calcification in coronary artery disease. A statistical analysis of intravascular ultrasound and coronary angiography in 1155 lesions," *Circulation,* vol. 91, pp. 1959-65, 1995.

[122] E. M. Tuzcu, B. Berkalp, A. C. De Franco, S. G. Ellis, M. Goormastic, P. L. Whitlow, I. Franco, R. E. Raymond, and S. E. Nissen, "The dilemma of diagnosing coronary calcification: angiography versus intravascular ultrasound," *J Am Coll Cardiol,* vol. 27, pp. 832-8, 1996.

[123] G. S. Mintz, P. Douek, A. D. Pichard, K. M. Kent, L. F. Satler, J. J. Popma, and M. B. Leon, "Target lesion calcification in coronary artery disease: an intravascular ultrasound study," *J Am Coll Cardiol,* vol. 20, pp. 1149-55, 1992.

[124] C. Di Mario, S. H. The, S. Madretsma, R. J. van Suylen, R. A. Wilson, N. Bom, P. W. Serruys, E. J. Gussenhoven, and J. R. Roelandt, "Detection and characterization of vascular lesions by intravascular ultrasound: an in vitro study correlated with histology," *J Am Soc Echocardiogr,* vol. 5, pp. 135-46, 1992.

[125] B. N. Potkin, A. L. Bartorelli, J. M. Gessert, R. F. Neville, Y. Almagor, W. C. Roberts, and M. B. Leon, "Coronary artery imaging with intravascular high-frequency ultrasound," *Circulation,* vol. 81, pp. 1575-85, 1990.

[126] Q. Rasheed, P. J. Dhawale, J. Anderson, and J. M. Hodgson, "Intracoronary ultrasound-defined plaque composition: computer-aided plaque characterization and correlation with histologic samples obtained during directional coronary atherectomy," *Am Heart J,* vol. 129, pp. 631-7, 1995.

[127] E. M. Tuzcu and N. J. Weissman, "Imaging coronary artery histology: a virtual pursuit?," *Circ Cardiovasc Imaging,* vol. 3, pp. 348-50, 2010.

[128] A. Maehara, G. S. Mintz, and N. J. Weissman, "Advances in intravascular imaging," *Circ Cardiovasc Interv,* vol. 2, pp. 482-90, 2009.

[129] M. Vavuranakis, I. A. Kakadiaris, S. M. O'Malley, T. G. Papaioannou, E. A. Sanidas, M. Naghavi, S. Carlier, D. Tousoulis, and C. Stefanadis, "A new method for assessment of plaque vulnerability based on vasa vasorum imaging, by using contrast-enhanced intravascular ultrasound and differential image analysis," *International Journal of Cardiology,* vol. 130, pp. 23-9, 2008.

[130] S. Carlier, I. A. Kakadiaris, N. Dib, M. Vavuranakis, S. M. O'Malley, K. Gul, C. J. Hartley, R. Metcalfe, R. Mehran, C. Stefanadis, E. Falk, G. Stone, M. Leon, and M. Naghavi, "Vasa vasorum imaging: a new window to the clinical detection of vulnerable atherosclerotic plaques," *Curr Atheroscler Rep,* vol. 7, pp. 164-9, 2005.

[131] N. Guo and G. S. Mintz, "Quantitative, Qualitative, and Diagnostic Intravascular Ultrasound," in *Textbook of Cardiovascular Intervention*, C. A. Thompson, Ed., ed London, UK: Springer London, 2013, pp. 23-39.

[132] D. G. Vince and A. Nair, "Intravascular Ultrasound for Plaque Characterization," in *The Vulnerable Atherosclerotic Plaque: Strategies for Diagnosis and Management*, R. Virmani, J. Narula, M. B. Leon, and J. T. Willerson, Eds., ed Malden, MA: Blackwell Publishing, 2007, pp. 222-229.

[133] A. Nair, B. D. Kuban, N. Obuchowski, and D. G. Vince, "Assessing spectral algorithms to predict atherosclerotic plaque composition with normalized and raw intravascular ultrasound data," *Ultrasound Med Biol,* vol. 27, pp. 1319-31, 2001.

[134] A. Nair, B. D. Kuban, E. M. Tuzcu, P. Schoenhagen, S. E. Nissen, and D. G. Vince, "Coronary plaque classification with intravascular ultrasound radiofrequency data analysis," *Circulation,* vol. 106, pp. 2200-6, 2002.

[135] A. Nair, M. P. Margolis, B. D. Kuban, and D. G. Vince, "Automated coronary plaque characterisation with intravascular ultrasound backscatter: ex vivo validation," *EuroIntervention,* vol. 3, pp. 113-20, 2007.

[136] K. Nasu, E. Tsuchikane, O. Katoh, D. G. Vince, R. Virmani, J. F. Surmely, A. Murata, Y. Takeda, T. Ito, M. Ehara, T. Matsubara, M. Terashima, and T. Suzuki, "Accuracy of in vivo coronary plaque morphology assessment: a validation study of in vivo virtual histology compared with in vitro histopathology," *J Am Coll Cardiol,* vol. 47, pp. 2405-12, 2006.

[137] J. Huisman, R. Egede, A. Rdzanek, D. Bose, R. Erbel, J. Kochman, L. O. Jensen, J. van de Palen, M. Hartmann, G. S. Mintz, and C. von Birgelen, "Between-centre reproducibility of volumetric intravascular ultrasound radiofrequency-based analyses in mild-to-moderate coronary atherosclerosis: an international multicentre study," *EuroIntervention,* vol. 5, pp. 925-31, 2010.

[138] M. Hartmann, E. S. Mattern, J. Huisman, G. K. van Houwelingen, F. H. de Man, M. G. Stoel, P. W. Danse, H. W. Louwerenburg, and C. von Birgelen, "Reproducibility of volumetric intravascular ultrasound radiofrequency-based analysis of coronary plaque composition in vivo," *Int J Cardiovasc Imaging,* vol. 25, pp. 13-23, 2009.

[139] H. M. Garcia-Garcia, G. S. Mintz, A. Lerman, D. G. Vince, M. P. Margolis, G. A. van Es, M. A. Morel, A. Nair, R. Virmani, A. P. Burke, G. W. Stone, and P. W. Serruys, "Tissue characterisation using intravascular radiofrequency data analysis: recommendations for acquisition, analysis, interpretation and reporting," *EuroIntervention,* vol. 5, pp. 177-89, 2009.

[140] K. Nasu, E. Tsuchikane, O. Katoh, H. Fujita, J. F. Surmely, M. Ehara, Y. Kinoshita, N. Tanaka, T. Matsubara, Y. Asakura, K. Asakura, M. Terashima, and T. Suzuki, "Plaque characterisation by Virtual Histology intravascular ultrasound analysis in patients with type 2 diabetes," *Heart,* vol. 94, pp. 429-33, 2008.

[141] T. Muramatsu, H. M. Garcia-Garcia, S. Brugaletta, J. H. Heo, Y. Onuma, R. J. Fedewa, A. Nair, Y. Ozaki, and P. W. Serruys, "Reproducibility of intravascular ultrasound radiofrequency data analysis (virtual histology) with a 45-MHz rotational imaging catheter in ex vivo human coronary arteries," *J Cardiol,* vol. 65, pp. 134-42, 2015.

[142] A. Nair, D. Calvetti, and D. G. Vince, "Regularized autoregressive analysis of intravascular ultrasound backscatter: improvement in spatial accuracy of tissue maps," *IEEE Trans Ultrason Ferroelectr Freq Control,* vol. 51, pp. 420-31, 2004.

[143] G. A. Rodriguez-Granillo, H. M. García-García, E. P. Mc Fadden, M. Valgimigli, J. Aoki, P. de Feyter, and P. W. Serruys, "In Vivo Intravascular Ultrasound-Derived Thin-Cap Fibroatheroma Detection Using Ultrasound Radiofrequency Data Analysis," *J Am Coll Cardiol,* vol. 46, pp. 2038-2042, 2005.

[144] A. V. Finn, Y. Chandrashekhar, and J. Narula, "Vulnerable plaques: from PROSPECT to prospects," *JACC Cardiovasc Imaging,* vol. 5, pp. 334-6, 2012.

[145] S. Brugaletta, C. Cola, V. Martin-Yuste, G. Vilahur, J. Oriol, T. Padro, J. M. Guerra, R. Borras, L. Badimon, and M. Sabate, "Qualitative and quantitative accuracy of ultrasound-based virtual histology for detection of necrotic core in human coronary arteries," *Int J Cardiovasc Imaging,* vol. 30, pp. 469-76, 2014.

[146] S. W. Kim, G. S. Mintz, Y. J. Hong, R. Pakala, K. S. Park, A. D. Pichard, L. F. Satler, K. M. Kent, W. O. Suddath, R. Waksman, and N. J. Weissman, "The virtual histology intravascular ultrasound appearance of newly placed drug-eluting stents," *Am J Cardiol,* vol. 102, pp. 1182-6, 2008.

[147] J. F. Granada, D. Wallace-Bradley, H. K. Win, C. L. Alviar, A. Builes, E. I. Lev, R. Barrios, D. G. Schulz, A. E. Raizner, and G. L. Kaluza, "In vivo plaque characterization using intravascular ultrasound-virtual histology in a porcine model of complex coronary lesions," *Arterioscler Thromb Vasc Biol,* vol. 27, pp. 387-93, 2007.

[148] T. Thim, M. K. Hagensen, D. Wallace-Bradley, J. F. Granada, G. L. Kaluza, L. Drouet, W. P. Paaske, H. E. Botker, and E. Falk, "Unreliable assessment of necrotic core by virtual histology intravascular ultrasound in porcine coronary artery disease," *Circ Cardiovasc Imaging,* vol. 3, pp. 384-91, 2010.

[149] R. Virmani and G. Nakazawa, "Animal models and virtual histology," *Arterioscler Thromb Vasc Biol,* vol. 27, pp. 1666; author reply 1667-8, 2007.

[150] G. W. Stone and G. S. Mintz, "Letter by Stone and Mintz regarding article, "unreliable assessment of necrotic core by virtual histology intravascular ultrasound in porcine coronary artery disease"," *Circ Cardiovasc Imaging,* vol. 3, p. e4; author reply e5, 2010.

[151] P. A. Calvert, D. R. Obaid, M. O'Sullivan, L. M. Shapiro, D. McNab, C. G. Densem, P. M. Schofield, D. Braganza, S. C. Clarke, K. K. Ray, N. E. J. West, and M. R. Bennett, "Association Between IVUS Findings and Adverse Outcomes in Patients With Coronary Artery DiseaseThe VIVA (VH-IVUS in Vulnerable Atherosclerosis) Study," *JACC Cardiovasc Imaging,* vol. 4, pp. 894-901, 2011.

[152] J. M. Cheng, H. M. Garcia-Garcia, S. P. de Boer, I. Kardys, J. H. Heo, K. M. Akkerhuis, R. M. Oemrawsingh, R. T. van Domburg, J. Ligthart, K. T. Witberg, E. Regar, P. W. Serruys, R. J. van Geuns, and E. Boersma, "In vivo detection of high-risk coronary plaques by radiofrequency intravascular ultrasound and cardiovascular outcome: results of the ATHEROREMO-IVUS study," *European Heart Journal,* vol. 35, pp. 639-47, 2014.

[153] S. J. Park, S. J. Kang, J. M. Ahn, M. Chang, S. C. Yun, J. H. Roh, P. H. Lee, H. W. Park, S. H. Yoon, D. W. Park, S. W. Lee, Y. H. Kim, C. W. Lee, G. S. Mintz, K. H. Han, and S. W. Park, "Effect of Statin Treatment on Modifying Plaque Composition: A Double-Blind, Randomized Study," *J Am Coll Cardiol,* vol. 67, pp. 1772-1783, 2016.

[154] S. E. Nissen, "IVUS Virtual Histology: Unvalidated Gimmick or Useful Technique?," *J Am Coll Cardiol,* vol. 67, pp. 1784-1785, 2016.

[155] D. Huang, E. A. Swanson, C. P. Lin, J. S. Schuman, W. G. Stinson, W. Chang, M. R. Hee, T. Flotte, K. Gregory, C. A. Puliafito, and et al., "Optical coherence tomography," *Science,* vol. 254, pp. 1178-81, 1991.

[156] M. L. Gabriele, G. Wollstein, H. Ishikawa, L. Kagemann, J. Xu, L. S. Folio, and J. S. Schuman, "Optical Coherence Tomography: History, Current Status, and Laboratory Work," *Invest Ophthalmol Vis Sci,* vol. 52, pp. 2425-36, 2011.

[157] E. Regar and I. K. Jang, "Optical coherence tomography," in *The Vulnerable Plaque*, R. Waksman, P. W. Serruys, and J. Schaar, Eds., 2 ed Boca Raton, FL: CRC Press, 2007, pp. 211-222.

[158] P. Magnin and E. Regar, "Optical Coherence Tomography," in *The Vulnerable Atherosclerotic Plaque: Strategies for Diagnosis and Management*, R. Virmani, J. Narula, M. B. Leon, and J. T. Willerson, Eds., ed Malden, MA: Blackwell Publishing, 2007, pp. 273-288.

[159] P. Barlis, J. Tanigawa, P. W. Serruys, and E. Regar, "Principles of Intra-Coronary Optical Coherence Tomography," in *Interventional Cardiology: Principles and Practice*, C. Di Mario, G. Dangas, and P. Barlis, Eds., ed Hoboken, NJ: Wiley-Blackwell, 2011, pp. 172-178.

[160] G. Ferrante, P. Presbitero, R. Whitbourn, and P. Barlis, "Current applications of optical coherence tomography for coronary intervention," *International Journal of Cardiology,* vol. 165, pp. 7-16, 2013.

[161] R. Puri, E. M. Tuzcu, S. E. Nissen, and S. J. Nicholls, "Exploring coronary atherosclerosis with intravascular imaging," *International Journal of Cardiology,* vol. 168, pp. 670-9, 2013.

[162] M. Terashima, H. Kaneda, and T. Suzuki, "The Role of Optical Coherence Tomography in Coronary Intervention," *Korean J Intern Med,* vol. 27, pp. 1-12, 2012.

[163] I. K. Jang, G. Tearney, and B. Bouma, "Visualization of tissue prolapse between coronary stent struts by optical coherence tomography: comparison with intravascular ultrasound," *Circulation,* vol. 104, p. 2754, 2001.

[164] I. K. Jang, B. E. Bouma, D. H. Kang, S. J. Park, S. W. Park, K. B. Seung, K. B. Choi, M. Shishkov, K. Schlendorf, E. Pomerantsev, S. L. Houser, H. T. Aretz, and G. J. Tearney, "Visualization of coronary atherosclerotic plaques in patients using optical coherence tomography: comparison with intravascular ultrasound," *J Am Coll Cardiol,* vol. 39, pp. 604-9, 2002.

[165] S. A. Boppart, B. E. Bouma, C. Pitris, J. F. Southern, M. E. Brezinski, and J. G. Fujimoto, "In vivo cellular optical coherence tomography imaging," *Nature Medicine,* vol. 4, pp. 861-5, 1998.

[166] T. Kume, T. Akasaka, T. Kawamoto, H. Okura, N. Watanabe, E. Toyota, Y. Neishi, R. Sukmawan, Y. Sadahira, and K. Yoshida, "Measurement of the thickness of the fibrous cap by optical coherence tomography," *Am Heart J,* vol. 152, pp. 755 e1-4, 2006.

[167] I. K. Jang, G. J. Tearney, B. MacNeill, M. Takano, F. Moselewski, N. Iftima, M. Shishkov, S. Houser, H. T. Aretz, E. F. Halpern, and B. E. Bouma, "In vivo characterization of coronary atherosclerotic plaque by use of optical coherence tomography," *Circulation,* vol. 111, pp. 1551-5, 2005.

[168] S. Takarada, T. Imanishi, T. Kubo, T. Tanimoto, H. Kitabata, N. Nakamura, A. Tanaka, M. Mizukoshi, and T. Akasaka, "Effect of statin therapy on coronary fibrous-cap thickness in patients with acute coronary syndrome: assessment by optical coherence tomography study," *Atherosclerosis,* vol. 202, pp. 491-7, 2009.

[169] S. Chia, O. C. Raffel, M. Takano, G. J. Tearney, B. E. Bouma, and I. K. Jang, "Association of statin therapy with reduced coronary plaque rupture: an optical coherence tomography study," *Coron Artery Dis,* vol. 19, pp. 237-42, 2008.

[170] G. J. Tearney, H. Yabushita, S. L. Houser, H. T. Aretz, I. K. Jang, K. H. Schlendorf, C. R. Kauffman, M. Shishkov, E. F. Halpern, and B. E. Bouma, "Quantification of macrophage content in atherosclerotic plaques by optical coherence tomography," *Circulation,* vol. 107, pp. 113-9, 2003.

[171] O. C. Raffel, G. J. Tearney, D. D. Gauthier, E. F. Halpern, B. E. Bouma, and I. K. Jang, "Relationship between a systemic inflammatory marker, plaque inflammation, and plaque characteristics determined by intravascular optical coherence tomography," *Arterioscler Thromb Vasc Biol,* vol. 27, pp. 1820-7, 2007.

[172] S. K. Nadkarni, M. C. Pierce, B. H. Park, J. F. de Boer, P. Whittaker, B. E. Bouma, J. E. Bressner, E. Halpern, S. L. Houser, and G. J. Tearney, "Measurement of collagen and smooth muscle cell content in atherosclerotic plaques using polarization-sensitive optical coherence tomography," *J Am Coll Cardiol,* vol. 49, pp. 1474-81, 2007.

[173] M. Kawasaki, B. E. Bouma, J. Bressner, S. L. Houser, S. K. Nadkarni, B. D. MacNeill, I. K. Jang, H. Fujiwara, and G. J. Tearney, "Diagnostic accuracy of optical coherence tomography and integrated backscatter intravascular ultrasound images for tissue characterization of human coronary plaques," *J Am Coll Cardiol,* vol. 48, pp. 81-8, 2006.

[174] M. E. Brezinski, G. J. Tearney, N. J. Weissman, S. A. Boppart, B. E. Bouma, M. R. Hee, A. E. Weyman, E. A. Swanson, J. F. Southern, and J. G. Fujimoto, "Assessing atherosclerotic plaque morphology: comparison of optical coherence tomography and high frequency intravascular ultrasound," *Heart,* vol. 77, pp. 397-403, 1997.

[175] I. K. Jang and D. S. Ong, "Optical Coherence Tomography and Other Emerging Diagnostic Procedures for Vulnerable Plaque," in *Myocardial Infarction: A Companion to Braunwald's Heart Disease E-Book*, D. A. Morrow, Ed., ed: Elsevier Health Sciences, 2016, pp. 103-113.

[176] H. Yabushita, B. E. Bouma, S. L. Houser, H. T. Aretz, I. K. Jang, K. H. Schlendorf, C. R. Kauffman, M. Shishkov, D. H. Kang, E. F. Halpern, and G. J. Tearney, "Characterization of human atherosclerosis by optical coherence tomography," *Circulation,* vol. 106, pp. 1640-5, 2002.

[177] T. Adriaenssens, "Basic Interpretation Skills," in *Cardiovascular OCT Imaging*, I. K. Jang, Ed., ed New York, NY: Springer International Publishing, 2014, pp. 53-66.

[178] G. S. Mintz, "Understanding Why and When Optical Coherence Tomography Does Not Detect Vulnerable Plaques: Is It Important?," *Circ Cardiovasc Interv,* vol. 9, 2016.

[179] J. E. Phipps, T. Hoyt, D. Vela, T. Wang, J. E. Michalek, L. M. Buja, I. K. Jang, T. E. Milner, and M. D. Feldman, "Diagnosis of Thin-Capped Fibroatheromas in Intravascular Optical Coherence Tomography Images: Effects of Light Scattering," *Circ Cardiovasc Interv,* vol. 9, 2016.

[180] O. Manfrini, E. Mont, O. Leone, E. Arbustini, V. Eusebi, R. Virmani, and R. Bugiardini, "Sources of error and interpretation of plaque morphology by optical coherence tomography," *Am J Cardiol,* vol. 98, pp. 156-9, 2006.

[181] L. Xing, T. Higuma, Z. Wang, A. D. Aguirre, K. Mizuno, M. Takano, H. L. Dauerman, S. J. Park, Y. Jang, C. J. Kim, S. J. Kim, S. Y. Choi, T. Itoh, S. Uemura, H. Lowe, D. L. Walters, P. Barlis, S. Lee, A. Lerman, C. Toma, J. W. C. Tan, E. Yamamoto, K. Bryniarski, J. Dai, T. Zanchin, S. Zhang, B. Yu, H. Lee, J. Fujimoto, V. Fuster, and I. K. Jang, "Clinical Significance of Lipid-Rich Plaque Detected by Optical Coherence Tomography: A 4-Year Follow-Up Study," *J Am Coll Cardiol,* vol. 69, pp. 2502-2513, 2017.

[182] E. Regar, M. Gnanadesigan, A. F. Van der Steen, and G. van Soest, "Quantitative optical coherence tomography tissue-type imaging for lipid-core plaque detection," *JACC Cardiovasc Interv,* vol. 6, pp. 891-2, 2013.

[183] M. Gnanadesigan, T. Kameyama, A. Karanasos, N. S. van Ditzhuijzen, J. N. van der Sijde, R. J. van Geuns, J. Ligthart, K. Witberg, G. J. Ughi, A. F. van der Steen, E. Regar, and G. van Soest, "Automated characterisation of lipid core plaques in vivo by quantitative optical coherence tomography tissue type imaging," *EuroIntervention,* vol. 12, pp. 1490-1497, 2016.

[184] Y. Kim, M. Gnanadesigan, G. van Soest, and T. W. Johnson, "A new technique for lipid core plaque detection by optical coherence tomography for prevention of peri-procedural myocardial infarction: A case report," *Medicine (Baltimore),* vol. 96, p. e7125, 2017.

[185] B. C. Zhang, A. Karanasos, M. Gnanadesigan, J. N. van der Sijde, N. van Ditzhuijzen, K. T. Witberg, J. Ligthart, R. Diletti, R. J. van Geuns, J. Dijkstra, F. Zijlstra, G. van Soest, and E. Regar, "Qualitative and quantitative evaluation of dynamic changes in non-culprit coronary atherosclerotic lesion morphology. A longitudinal OCT study," *EuroIntervention,* 2017.

[186] C. Xu, J. M. Schmitt, S. G. Carlier, and R. Virmani, "Characterization of atherosclerosis plaques by measuring both backscattering and attenuation coefficients in optical coherence tomography," *J Biomed Opt,* vol. 13, p. 034003, 2008.

[187] G. van Soest, T. Goderie, E. Regar, S. Koljenovic, G. L. van Leenders, N. Gonzalo, S. van Noorden, T. Okamura, B. E. Bouma, G. J. Tearney, J. W. Oosterhuis, P. W. Serruys, and A. F. van der Steen, "Atherosclerotic tissue characterization in vivo by optical coherence tomography attenuation imaging," *J Biomed Opt,* vol. 15, p. 011105, 2010.

[188] M. Gnanadesigan, A. S. Hussain, S. White, S. Scoltock, A. Baumbach, A. F. van der Steen, E. Regar, T. W. Johnson, and G. van Soest, "Optical coherence tomography attenuation imaging for lipid core detection: an ex-vivo validation study," *Int J Cardiovasc Imaging,* vol. 33, pp. 5-11, 2017.

[189] J. Yin, H. C. Yang, X. Li, J. Zhang, Q. Zhou, C. Hu, K. K. Shung, and Z. Chen, "Integrated intravascular optical coherence tomography ultrasound imaging system," *J Biomed Opt,* vol. 15, p. 010512, 2010.

[190] J. Li, X. Li, D. Mohar, A. Raney, J. Jing, J. Zhang, A. Johnston, S. Liang, T. Ma, K. K. Shung, S. Mahon, M. Brenner, J. Narula, Q. Zhou, P. M. Patel, and Z. Chen, "Integrated IVUS-OCT for real-time imaging of coronary atherosclerosis," *JACC Cardiovasc Imaging,* vol. 7, pp. 101-3, 2014.

[191] X. Li, J. Li, J. Jing, T. Ma, S. Liang, J. Zhang, D. Mohar, A. Raney, S. Mahon, M. Brenner, P. Patel, K. K. Shung, Q. Zhou, and Z. Chen, "Integrated IVUS-OCT Imaging for Atherosclerotic Plaque Characterization," *IEEE J Sel Top Quantum Electron,* vol. 20, p. 7100108, 2014.

[192] J. Li, T. Ma, D. Mohar, E. Steward, M. Yu, Z. Piao, Y. He, K. K. Shung, Q. Zhou, P. M. Patel, and Z. Chen, "Ultrafast optical-ultrasonic system and miniaturized catheter for imaging and characterizing atherosclerotic plaques in vivo," *Sci Rep,* vol. 5, p. 18406, 2015.

[193] F. Prati, M. T. Mallus, F. Imola, and M. Albertucci, "Optical Coherence Tomography (OCT)," in *Catheter-Based Cardiovascular Interventions: A Knowledge-Based Approach*, P. Lanzer, Ed., ed Berlin, Germany: Springer Berlin-Heidelberg, 2012, pp. 363-374.

[194] B. D. MacNeill, H. C. Lowe, M. Takano, V. Fuster, and I. K. Jang, "Intravascular modalities for detection of vulnerable plaque: current status," *Arterioscler Thromb Vasc Biol,* vol. 23, pp. 1333-42, 2003.

[195] J. N. van der Sijde, A. Karanasos, N. S. van Ditzhuijzen, T. Okamura, R. J. van Geuns, M. Valgimigli, J. M. Ligthart, K. T. Witberg, S. Wemelsfelder, J. M. Fam, B. Zhang, R. Diletti, P. P. de Jaegere, N. M. van Mieghem, G. van Soest, F. Zijlstra, R. T. van Domburg, and E. Regar, "Safety of optical coherence tomography in daily practice: a comparison with intravascular ultrasound," *Eur Heart J Cardiovasc Imaging,* vol. 18, pp. 467-474, 2017.

[196] P. R. Moreno, B. Marshik, and J. E. Muller, "Near-Infrared Spectroscopy," in *The Vulnerable Atherosclerotic Plaque: Strategies for Diagnosis and Management*, R. Virmani, J. Narula, M. B. Leon, and J. T. Willerson, Eds., ed Malden, MA: Blackwell Publishing, 2007, pp. 257-262.

[197] P. R. Moreno and J. E. Muller, "Identification of high-risk atherosclerotic plaques: a survey of spectroscopic methods," *Curr Opin Cardiol,* vol. 17, pp. 638-47, 2002.

[198] S. Waxman, "Near-Infrared Spectroscopy for Plaque Characterization," *J Interv Card,* vol. 21, pp. 452-458, 2008.

[199] J. A. Goldstein, B. Maini, S. R. Dixon, E. S. Brilakis, C. L. Grines, D. G. Rizik, E. R. Powers, D. H. Steinberg, K. A. Shunk, G. Weisz, P. R. Moreno, A. Kini, S. K. Sharma, M. J. Hendricks, S. T. Sum, S. P. Madden, J. E. Muller, G. W. Stone, and M. J. Kern, "Detection of Lipid-Core Plaques by Intracoronary Near-Infrared Spectroscopy Identifies High Risk of Periprocedural Myocardial Infarction," *Circ Cardiovasc Interv,* vol. 4, pp. 429-437, 2011.

[200] L. A. Cassis and R. A. Lodder, "Near-IR imaging of atheromas in living arterial tissue," *Analytical Chemistry,* vol. 65, pp. 1247-56, 1993.

[201] R. J. Dempsey, D. G. Davis, R. G. Buice, and R. A. Lodder, "Biological and medical applications of near-infrared spectrometry," *Appl Spectrosc,* vol. 50, pp. 18A-34A, 1996.

[202] P. R. Moreno, R. A. Lodder, K. R. Purushothaman, W. E. Charash, W. N. O'Connor, and J. E. Muller, "Detection of lipid pool, thin fibrous cap, and inflammatory cells in human aortic atherosclerotic plaques by near-infrared spectroscopy," *Circulation,* vol. 105, pp. 923-7, 2002.

[203] C. M. Gardner, H. Tan, E. L. Hull, J. B. Lisauskas, S. T. Sum, T. M. Meese, C. Jiang, S. P. Madden, J. D. Caplan, A. P. Burke, R. Virmani, J. Goldstein, and J. E. Muller, "Detection of lipid core coronary plaques in autopsy specimens with a novel catheter-based near-infrared spectroscopy system," *JACC Cardiovasc Imaging,* vol. 1, pp. 638-48, 2008.

[204] S. Waxman, S. R. Dixon, P. L'Allier, J. W. Moses, J. L. Petersen, D. Cutlip, J.-C. Tardif, R. W. Nesto, J. E. Muller, M. J. Hendricks, S. T. Sum, C. M. Gardner, J. A. Goldstein, G. W. Stone, and M. W. Krucoff, "In Vivo Validation of a Catheter-Based Near-Infrared Spectroscopy System for Detection of Lipid Core Coronary Plaques: Initial Results of the SPECTACL Study," *JACC Cardiovasc Imaging,* vol. 2, pp. 858-868, 2009.

[205] S. T. Sum, S. P. Madden, M. J. Hendricks, S. J. Chartier, and J. E. Muller, "Near-infrared spectroscopy for the detection of lipid core coronary plaques," *Curr Cardiovasc Imaging Rep,* vol. 2, pp. 307-315, 2009.

[206] I. D. Kilic, G. Caiazzo, E. Fabris, R. Serdoz, S. Abou-Sherif, S. Madden, P. R. Moreno, J. Goldstein, and C. Di Mario, "Near-infrared spectroscopy-intravascular ultrasound: scientific basis and clinical applications," *Eur Heart J Cardiovasc Imaging,* vol. 16, pp. 1299-306, 2015.

[207] D. G. Rizik and J. A. Goldstein, "NIRS-IVUS Characterization of Plaque Structure and Composition: Implications for Optimal Stenting and Detection of Vulnerable Plaque," *J Invasive Cardiol,* vol. 25, 2013.

[208] C. J. Schultz, P. W. Serruys, M. van der Ent, J. Ligthart, F. Mastik, S. Garg, J. E. Muller, M. A. Wilder, A. F. van de Steen, and E. Regar, "First-in-man clinical use of combined near-infrared spectroscopy and intravascular ultrasound: a potential key to predict distal embolization and no-reflow?," *J Am Coll Cardiol,* vol. 56, p. 314, 2010.

[209] D. Raghunathan, A.-R. R. Abdel-Karim, A. C. Papayannis, M. daSilva, O. M. Jeroudi, B. V. Rangan, S. Banerjee, and E. S. Brilakis, "Relation Between the Presence and Extent of Coronary Lipid Core Plaques Detected by Near-Infrared Spectroscopy With Postpercutaneous Coronary Intervention Myocardial Infarction," *Am J Cardiol,* vol. 107, pp. 1613-1618, 2011.

[210] R. D. Madder, J. A. Goldstein, S. P. Madden, R. Puri, K. Wolski, M. Hendricks, S. T. Sum, A. Kini, S. Sharma, D. Rizik, E. S. Brilakis, K. A. Shunk, J. Petersen, G. Weisz, R. Virmani, S. J. Nicholls, A. Maehara, G. S. Mintz, G. W. Stone, and J. E. Muller, "Detection by near-infrared spectroscopy of large lipid core plaques at culprit sites in patients with acute ST-segment elevation myocardial infarction," *JACC Cardiovasc Interv,* vol. 6, pp. 838-46, 2013.

[211] R. M. Oemrawsingh, J. M. Cheng, H. M. García-García, R.-J. van Geuns, S. P. M. de Boer, C. Simsek, I. Kardys, M. J. Lenzen, R. T. van Domburg, E. Regar, P. W. Serruys, K. M. Akkerhuis, and E. Boersma, "Near-Infrared Spectroscopy Predicts Cardiovascular Outcome in Patients With Coronary Artery Disease," *J Am Coll Cardiol,* vol. 64, pp. 2510-2518, 2014.

[212] R. D. Madder, M. Husaini, A. T. Davis, S. M. Vanoosterhout, M. Khan, M. Chi, Z. Turfe, A. Schmale, S. Dionne, D. H. Wohns, J. S. Collins, M. Jacoby, J. Decker, M. Hendricks, S. Sum, S. Madden, and J. E. Muller, "TCT-398 Identification of Vulnerable Patients by Intracoronary Near-infrared Spectroscopy," *J Am Coll Cardiol,* vol. 64, p. B117, 2014.

[213] R. D. Madder, R. Puri, J. E. Muller, J. Harnek, M. Gotberg, S. VanOosterhout, M. Chi, D. Wohns, R. McNamara, K. Wolski, S. Madden, S. Sidharta, J. Andrews, S. J. Nicholls, and D. Erlinge, "Confirmation of the Intracoronary Near-Infrared Spectroscopy Threshold of Lipid-Rich Plaques That Underlie ST-Segment-Elevation Myocardial Infarction," *Arterioscler Thromb Vasc Biol,* 2016.

[214] R. Puri, R. D. Madder, S. P. Madden, S. T. Sum, K. Wolski, J. E. Muller, J. Andrews, K. L. King, Y. Kataoka, K. Uno, S. R. Kapadia, E. M. Tuzcu, S. E. Nissen, R. Virmani, A. Maehara, G. S. Mintz, and S. J. Nicholls, "Near-Infrared Spectroscopy Enhances Intravascular Ultrasound Assessment of Vulnerable Coronary Plaque: A Combined Pathological and In Vivo Study," *Arterioscler Thromb Vasc Biol,* vol. 35, pp. 2423-31, 2015.

[215] A. S. Kini, S. Motoyama, Y. Vengrenyuk, J. E. Feig, J. Pena, U. Baber, A. M. Bhat, P. Moreno, J. C. Kovacic, J. Narula, and S. K. Sharma, "Multimodality Intravascular Imaging to Predict Periprocedural Myocardial Infarction During Percutaneous Coronary Intervention," *JACC Cardiovasc Interv,* vol. 8, pp. 937-45, 2015.

[216] R. D. Madder, M. Husaini, A. T. Davis, S. VanOosterhout, M. Khan, D. Wohns, R. F. McNamara, K. Wolschleger, J. Gribar, J. S. Collins, M. Jacoby, J. M. Decker, M. Hendricks, S. T. Sum, S. Madden, J. H. Ware, and J. E. Muller, "Large lipid-rich coronary plaques detected by near-infrared spectroscopy at non-stented sites in the target artery identify patients likely to experience future major adverse cardiovascular events," *Eur Heart J Cardiovasc Imaging,* vol. 17, pp. 393-9, 2016.

[217] B. A. Danek, A. Karatasakis, J. Karacsonyi, A. Alame, E. Resendes, P. Kalsaria, P. J. Nguyen-Trong, B. V. Rangan, M. Roesle, S. Abdullah, S. Banerjee, and E. S. Brilakis, "Long-term follow-up after near-infrared spectroscopy coronary imaging: Insights from the lipid cORe plaque association with CLinical events (ORACLE-NIRS) registry," *Cardiovasc Revasc Med,* vol. 18, pp. 177-181, 2017.

[218] A. S. Kini, U. Baber, J. C. Kovacic, A. Limaye, Z. A. Ali, J. Sweeny, A. Maehara, R. Mehran, G. Dangas, G. S. Mintz, V. Fuster, J. Narula, S. K. Sharma, and P. R. Moreno, "Changes in Plaque Lipid Content After Short-Term Intensive Versus Standard Statin Therapy: The YELLOW Trial (Reduction in Yellow Plaque by Aggressive Lipid-Lowering Therapy)," *J Am Coll Cardiol,* vol. 62, pp. 21-29, 2013.

[219] A. S. Kini, P. Moreno, J. Kovacic, A. Limaye, Z. Ali, J. Sweeny, U. Baber, G. Dangas, and S. Sharma, "Does aggressive statin therapy reduce coronary atherosclerotic plaque lipid content? results from: reduction in Yellow Plaque By Aggressive Lipid Lowering Therapy (YELLOW) trial," *J Am Coll Cardiol,* vol. 59, pp. E304-E304, 2012.

[220] A. S. Kini, Y. Vengrenyuk, K. Shameer, A. Maehara, M. Purushothaman, T. Yoshimura, M. Matsumura, M. Aquino, N. Haider, K. W. Johnson, B. Readhead, B. A. Kidd, J. E. Feig, P. Krishnan, J. Sweeny, M. Milind, P. Moreno, R. Mehran, J. C. Kovacic, U. Baber, J. T. Dudley, J. Narula, and S. Sharma, "Intracoronary Imaging, Cholesterol Efflux, and Transcriptomes After Intensive Statin Treatment: The YELLOW II Study," *J Am Coll Cardiol,* vol. 69, pp. 628-640, 2017.

[221] A. S. Schuurman, M. Vroegindewey, I. Kardys, R. M. Oemrawsingh, J. M. Cheng, S. de Boer, H. M. Garcia-Garcia, R. J. van Geuns, E. S. Regar, J. Daemen, N. M. van Mieghem, P. W. Serruys, E. Boersma, and K. M. Akkerhuis, "Near-infrared spectroscopy-derived lipid core burden index predicts adverse cardiovascular outcome in patients with coronary artery disease during long-term follow-up," *European Heart Journal,* 2017.

[222] R. Waksman, R. Torguson, M.-A. Spad, H. Garcia-Garcia, J. Ware, R. Wang, S. Madden, P. Shah, and J. Muller, "The Lipid-Rich Plaque Study of vulnerable plaques and vulnerable patients: Study design and rationale," *Am Heart J,* vol. 192, pp. 98-104, 2017.

[223] M. Naghavi, R. John, S. Naguib, M. S. Siadaty, R. Grasu, K. C. Kurian, W. B. van Winkle, B. Soller, S. Litovsky, M. Madjid, J. T. Willerson, and W. Casscells, "pH Heterogeneity of human and rabbit atherosclerotic plaques; a new insight into detection of vulnerable plaque," *Atherosclerosis,* vol. 164, pp. 27-35, 2002.

[224] T. Khan, B. Soller, M. Naghavi, and W. Casscells, "Tissue pH determination for the detection of metabolically active, inflamed vulnerable plaques using near-infrared spectroscopy: an in-vitro feasibility study," *Cardiology,* vol. 103, pp. 10-6, 2005.

[225] W. Bo, J. L. Su, A. B. Karpiouk, K. V. Sokolov, R. W. Smalling, and S. Y. Emelianov, "Intravascular Photoacoustic Imaging," *Selected Topics in Quantum Electronics, IEEE Journal of,* vol. 16, pp. 588-599, 2010.

[226] K. Jansen, G. van Soest, and A. F. van der Steen, "Intravascular photoacoustic imaging: a new tool for vulnerable plaque identification," *Ultrasound Med Biol,* vol. 40, pp. 1037-48, 2014.

[227] R. Bouchard, O. Sahin, and S. Emelianov, "Ultrasound-Guided Photoacoustic Imaging: Current State and Future Development," *IEEE Trans Ultrason Ferroelectr Freq Control,* vol. 61, pp. 450-466, 2014.

[228] P. Wang, J. R. Rajian, and J. X. Cheng, "Spectroscopic Imaging of Deep Tissue through Photoacoustic Detection of Molecular Vibration," *Journal of Physical Chemistry Letters,* vol. 4, pp. 2177-2185, 2013.

[229] J. Hui, R. Li, E. H. Phillips, C. J. Goergen, M. Sturek, and J.-X. Cheng, "Bond-selective photoacoustic imaging by converting molecular vibration into acoustic waves," *Photoacoustics,* vol. 4, pp. 11-21, 2016.

[230] S. Sethuraman, S. R. Aglyamov, J. H. Amirian, R. W. Smalling, and S. Y. Emelianov, "Intravascular photoacoustic imaging using an IVUS imaging catheter," *IEEE Trans Ultrason Ferroelectr Freq Control,* vol. 54, pp. 978-986, 2007.

[231] W. Bo, A. Karpiouk, and S. Emelianov, "Design of catheter for combined intravascular photoacoustic and ultrasound imaging," in *Ultrasonics Symposium, 2008. IUS 2008. IEEE*, 2008, pp. 1150-1153.

[232] K. Jansen, G. Springeling, C. Lancee, R. Beurskens, F. Mastik, A. F. W. van der Steen, and G. van Soest, "An intravascular photoacoustic imaging catheter," in *Ultrasonics Symposium (IUS), 2010 IEEE*, 2010, pp. 378-381.

[233] A. B. Karpiouk, B. Wang, and S. Y. Emelianov, "Development of a catheter for combined intravascular ultrasound and photoacoustic imaging," *Rev Sci Instrum,* vol. 81, p. 014901, 2010.

[234] W. Wei, X. Li, Q. Zhou, K. K. Shung, and Z. Chen, "Integrated ultrasound and photoacoustic probe for co-registered intravascular imaging," *J Biomed Opt,* vol. 16, pp. 106001-106001-6, 2011.

[235] D. VanderLaan, A. Karpiouk, D. Yeager, and S. Emelianov, "System and Integrated Catheter for Real-Time Intravascular Ultrasound and Photoacoustic Imaging," *2014 IEEE International Ultrasonics Symposium,* pp. 1591-1594, 2014.

[236] S. Sethuraman, J. H. Amirian, S. H. Litovsky, R. W. Smalling, and S. Y. Emelianov, "Ex vivo Characterization of Atherosclerosis using Intravascular Photoacoustic Imaging," *Optics Express,* vol. 15, pp. 16657-16666, 2007.

[237] S. Sethuraman, J. H. Amirian, S. H. Litovsky, R. W. Smalling, and S. Y. Emelianov, "Spectroscopic intravascular photoacoustic imaging to differentiate atherosclerotic plaques," *Optics Express,* vol. 16, pp. 3362-3367, 2008.

[238] T. J. Allen and P. C. Beard, "Photoacoustic characterisation of vascular tissue at NIR wavelengths," in *Photons Plus Ultrasound: Imaging and Sensing 2009*, San Jose, CA, 2009, pp. 71770A-71770A-9.

[239] W. Bo, J. Su, J. Amirian, S. H. Litovsky, R. Smalling, and S. Emelianov, "On the possibility to detect lipid in atherosclerotic plaques using intravascular photoacoustic imaging," in *Engineering in Medicine and Biology Society, 2009. EMBC 2009. Annual International Conference of the IEEE*, 2009, pp. 4767-4770.

[240] K. Jansen, A. F. van der Steen, H. M. van Beusekom, J. W. Oosterhuis, and G. van Soest, "Intravascular photoacoustic imaging of human coronary atherosclerosis," *Opt Lett,* vol. 36, pp. 597-9, 2011.

[241] K. Jansen, M. Wu, A. F. W. van der Steen, and G. van Soest, "Lipid detection in atherosclerotic human coronaries by spectroscopic intravascular photoacoustic imaging," *Optics Express,* vol. 21, pp. 21472-21484, 2013.

[242] K. Jansen, M. Wu, A. F. W. van der Steen, and G. van Soest, "Photoacoustic imaging of human coronary atherosclerosis in two spectral bands," *Photoacoustics,* vol. 2, pp. 12-20, 2014.

[243] B. Wang, J. L. Su, J. Amirian, S. H. Litovsky, R. Smalling, and S. Emelianov, "Detection of lipid in atherosclerotic vessels using ultrasound-guided spectroscopic intravascular photoacoustic imaging," *Optics Express,* vol. 18, pp. 4889-4897, 2010.

[244] B. Wang, A. Karpiouk, D. Yeager, J. Amirian, S. Litovsky, R. Smalling, and S. Emelianov, "Intravascular photoacoustic imaging of lipid in atherosclerotic plaques in the presence of luminal blood," *Opt Lett,* vol. 37, pp. 1244-6, 2012.

[245] B. Wang, A. Karpiouk, D. Yeager, J. Amirian, S. Litovsky, R. Smalling, and S. Emelianov, "In vivo Intravascular Ultrasound-guided Photoacoustic Imaging of Lipid in Plaques Using an Animal Model of Atherosclerosis," *Ultrasound Med Biol,* vol. 38, pp. 2098-2103, 2012.

[246] A. B. Karpiouk, B. Wang, J. Amirian, R. W. Smalling, and S. Y. Emelianov, "Feasibility of in vivo intravascular photoacoustic imaging using integrated ultrasound and photoacoustic imaging catheter," *J Biomed Opt,* vol. 17, pp. 0960081-0960086, 2012.

[247] P. Wang, P. Wang, H. W. Wang, and J. X. Cheng, "Mapping lipid and collagen by multispectral photoacoustic imaging of chemical bond vibration," *J Biomed Opt,* vol. 17, pp. 96010-1, 2012.

[248] P. Wang, H. W. Wang, M. Sturek, and J. X. Cheng, "Bond-selective imaging of deep tissue through the optical window between 1600 and 1850 nm," *Journal of Biophotonics,* vol. 5, pp. 25-32, 2012.

[249] A. Rosenthal, F. A. Jaffer, and V. Ntziachristos, "Intravascular multispectral optoacoustic tomography of atherosclerosis: prospects and challenges," *Imaging Med,* vol. 4, pp. 299-310, 2012.

[250] P. Wang, T. Ma, M. N. Slipchenko, S. Liang, J. Hui, K. K. Shung, S. Roy, M. Sturek, Q. Zhou, Z. Chen, and J. X. Cheng, "High-speed Intravascular Photoacoustic Imaging of Lipid-laden Atherosclerotic Plaque Enabled by a 2-kHz Barium Nitrite Raman Laser," *Sci Rep,* vol. 4, p. 6889, 2014.

[251] J. Zhang, S. Yang, X. Ji, Q. Zhou, and D. Xing, "Characterization of lipid-rich aortic plaques by intravascular photoacoustic tomography: ex vivo and in vivo validation in a rabbit atherosclerosis model with histologic correlation," *J Am Coll Cardiol,* vol. 64, pp. 385-90, 2014.

[252] P. Schoenhagen and D. G. Vince, "Intravascular photoacoustic tomography of coronary atherosclerosis: riding the waves of light and sound," *J Am Coll Cardiol,* vol. 64, pp. 391-3, 2014.

[253] M. Wu, G. Springeling, M. Lovrak, F. Mastik, S. Iskander-Rizk, T. Wang, H. M. van Beusekom, A. F. van der Steen, and G. Van Soest, "Real-time volumetric lipid imaging in vivo by intravascular photoacoustics at 20 frames per second," *Biomed Opt Express,* vol. 8, pp. 943-953, 2017.

[254] J. Hui, Y. Cao, Y. Zhang, A. Kole, P. Wang, G. Yu, G. Eakins, M. Sturek, W. Chen, and J. X. Cheng, "Real-time intravascular photoacoustic-ultrasound imaging of lipid-laden plaque in human coronary artery at 16 frames per second," *Sci Rep,* vol. 7, p. 1417, 2017.

[255] Y. Cao, J. Hui, A. Kole, P. Wang, Q. Yu, W. Chen, M. Sturek, and J.-X. Cheng, "High-sensitivity intravascular photoacoustic imaging of lipid–laden plaque with a collinear catheter design," *Sci Rep,* vol. 6, p. 25236, 2016.

[256] M. Wu, "Detecting Cardiac Infarction Risk Reliably Using Fast Laser Pulses," *Optik & Photonik,* vol. 12, pp. 26-29, 2017.

[257] M. Wu, A. van der Steen, E. Regar, and G. van Soest, *Emerging Technology Update Intravascular Photoacoustic Imaging of Vulnerable Atherosclerotic Plaque* vol. 11, 2016.

[258] V. Daeichin, M. Wu, N. De Jong, A. F. van der Steen, and G. van Soest, "Frequency Analysis of the Photoacoustic Signal Generated by Coronary Atherosclerotic Plaque," *Ultrasound Med Biol,* vol. 42, pp. 2017-25, 2016.

[259] P. Duewell, H. Kono, K. J. Rayner, C. M. Sirois, G. Vladimer, F. G. Bauernfeind, G. S. Abela, L. Franchi, G. Nunez, M. Schnurr, T. Espevik, E. Lien, K. A. Fitzgerald, K. L. Rock, K. J. Moore, S. D. Wright, V. Hornung, and E. Latz, "NLRP3 inflammasomes are required for atherogenesis and activated by cholesterol crystals," *Nature,* vol. 464, pp. 1357-61, 2010.

[260] K. Jansen, A. F. van der Steen, M. Wu, H. M. van Beusekom, G. Springeling, X. Li, Q. Zhou, K. K. Shung, D. P. de Kleijn, and G. van Soest, "Spectroscopic intravascular photoacoustic imaging of lipids in atherosclerosis," *J Biomed Opt,* vol. 19, p. 026006, 2014.

[261] Y. Cao, A. Kole, L. Lan, P. Wang, J. Hui, M. Sturek, and J.-X. Cheng, "Spectral analysis assisted photoacoustic imaging for lipid composition differentiation," *Photoacoustics,* vol. 7, pp. 12-19, 2017.

[262] B. Wang, E. Yantsen, K. Sokolov, and S. Emelianov, "High sensitivity intravascular photoacoustic imaging of macrophages," in *Photons Plus Ultrasound: Imaging and Sensing 2009*, San Jose, CA, 2009, pp. 71770V-71770V-6.

[263] B. Wang, E. Yantsen, T. Larson, A. B. Karpiouk, S. Sethuraman, J. L. Su, K. Sokolov, and S. Y. Emelianov, "Plasmonic Intravascular Photoacoustic Imaging for Detection of Macrophages in Atherosclerotic Plaques," *Nano Letters,* vol. 9, pp. 2212-2217, 2009.

[264] D. E. Yeager, A. B. Karpiouk, B. Wang, J. H. Amirian, K. V. Sokolov, R. W. Smalling, and S. Y. Emelianov, "Intravascular photoacoustic imaging of exogenously labeled atherosclerotic plaque through luminal blood," 2012, p. 8.

[265] D. Razansky, N. J. Harlaar, J. L. Hillebrands, A. Taruttis, E. Herzog, C. J. Zeebregts, G. M. van Dam, and V. Ntziachristos, "Multispectral Optoacoustic Tomography of Matrix Metalloproteinase Activity in Vulnerable Human Carotid Plaques," *Mol Imaging Biol,* vol. 14, pp. 277-285, 2012.

[266] H. W. Wang, N. Chai, P. Wang, S. Hu, W. Dou, D. Umulis, L. V. Wang, M. Sturek, R. Lucht, and J. X. Cheng, "Label-free bond-selective imaging by listening to vibrationally excited molecules," *Physical Review Letters,* vol. 106, p. 238106, 2011.

[267] M. Wu, K. Jansen, A. F. W. van der Steen, and G. van Soest, "Specific imaging of atherosclerotic plaque lipids with two-wavelength intravascular photoacoustics," *Biomed Opt Express,* vol. 6, pp. 3276-3286, 2015.

[268] S. N. Verhagen and F. L. Visseren, "Perivascular adipose tissue as a cause of atherosclerosis," *Atherosclerosis,* vol. 214, pp. 3-10, 2011.

[269] H. Y. Lee, J. P. Despres, and K. K. Koh, "Perivascular adipose tissue in the pathogenesis of cardiovascular disease," *Atherosclerosis,* vol. 230, pp. 177-84, 2013.

[270] S. E. Nissen, "Coronary angiography and intravascular ultrasound," *Am J Cardiol,* vol. 87, pp. 15A-20A, 2001.

[271] A. F. Low, G. J. Tearney, B. E. Bouma, and I.-K. Jang, "Technology Insight: optical coherence tomography - current status and future development," *Nat Clin Pract Cardiovasc Med,* vol. 3, pp. 154-162, 2006.

[272] K. Patel, J. Tarkin, P. W. Serruys, E. Tenekecioglu, N. Foin, Y. J. Zhang, T. Crake, J. Moon, A. Mathur, and C. V. Bourantas, "Invasive or non-invasive imaging for detecting high-risk coronary lesions?," *Expert Rev Cardiovasc Ther,* vol. 15, pp. 165-179, 2017.

[273] C. V. Bourantas, H. M. Garcia-Garcia, K. K. Naka, A. Sakellarios, L. Athanasiou, D. I. Fotiadis, L. K. Michalis, and P. W. Serruys, "Hybrid Intravascular Imaging Current Applications and Prospective Potential in the Study of Coronary Atherosclerosis," *J Am Coll Cardiol,* vol. 61, pp. 1369-1378, 2013.

[274] A. M. Fard, P. Vacas-Jacques, E. Hamidi, H. Wang, R. W. Carruth, J. A. Gardecki, and G. J. Tearney, "Optical coherence tomography - near infrared spectroscopy system and catheter for intravascular imaging," *Optics Express,* vol. 21, pp. 30849-30858, 2013.

[275] C. V. Bourantas, H. M. Garcia-Garcia, R. Torii, Y. J. Zhang, M. Westwood, T. Crake, and P. W. Serruys, "Vulnerable plaque detection: an unrealistic quest or a feasible objective with a clinical value?," *Heart,* vol. 102, pp. 581-9, 2016.

[276] C. Stefanadis, C. K. Antoniou, D. Tsiachris, and P. Pietri, "Coronary Atherosclerotic Vulnerable Plaque: Current Perspectives," *J Am Heart Assoc,* vol. 6, 2017.

[277] M. Kamalesh, A. Balmuri, and A. Boddu, "Clinical utility of self-expanding stents in coronary artery disease," *Research Reports in Clinical Cardiology,* p. 117, 2015.

[278] J. F. Granada, K. Milewski, M. P. Uribe, M. Moncada, A. Fernandez, G. Blanco, G. L. Kaluza, J. J. Wykrzykowska, P. W. Serruys, G. W. Stone, and J. A. Delgado, "First clinical evaluation of a luminal self-expanding shield in patients with intermediate coronary lesions," *EuroIntervention,* vol. 7, pp. 780-8, 2011.

[279] J. J. Wykrzykowska, R. Diletti, J. L. Gutierrez-Chico, R. J. van Geuns, W. J. van der Giessen, S. Ramcharitar, H. E. Duckers, C. Schultz, P. de Feyter, M. van der Ent, E. Regar, P. de Jaegere, H. M. Garcia-Garcia, R. Pawar, N. Gonzalo, J. Ligthart, J. de Schepper, N. van den Berg, K. Milewski, J. F. Granada, and P. W. Serruys, "Plaque sealing and passivation with a mechanical self-expanding low outward force nitinol vShield device for the treatment of IVUS and OCT-derived thin cap fibroatheromas (TCFAs) in native coronary arteries: report of the pilot study vShield Evaluated at Cardiac hospital in Rotterdam for Investigation and Treatment of TCFA (SECRITT)," *EuroIntervention,* vol. 8, pp. 945-54, 2012.

[280] M. Zimarino, F. Prati, R. Marano, F. Angeramo, I. Pescetelli, L. Gatto, V. Marco, I. Bruno, and R. De Caterina, "The value of imaging in subclinical coronary artery disease," *Vasc Pharmacol,* 2016.

[281] H. M. Garcia-Garcia, I. K. Jang, P. W. Serruys, J. C. Kovacic, J. Narula, and Z. A. Fayad, "Imaging plaques to predict and better manage patients with acute coronary events," *Circ Res,* vol. 114, pp. 1904-17, 2014.

[282] C. M. Campos, H. M. Garcia-Garcia, T. Muramatsu, P. de Araujo Gonçalves, Y. Onuma, D. Dudek, L. Thuesen, M. W. I. Webster, P. Kitslaar, S. Veldhof, J. H. C. Reiber, K. Nieman, J. A. Ormiston, and P. W. Serruys, "Impact of the Everolimus-eluting Bioresorbable Scaffold in Coronary Atherosclerosis," *Revista Española de Cardiología (English Edition),* vol. 69, pp. 109-116, 2016.

[283] C. Di Mario and P. R. Moreno, "Invasive coronary imaging: any role in primary and secondary prevention?," *European Heart Journal,* 2016.

[284] A. Arbab-Zadeh and V. Fuster, "Reply: Vulnerable Plaque: Absence of Evidence or Evidence of Absence," *J Am Coll Cardiol,* vol. 66, pp. 758-759, 2015.

[285] M. S. Albaghdadi and E. D. Muse, "Vulnerable Plaque: Absence of Evidence or Evidence of Absence," *J Am Coll Cardiol,* vol. 66, pp. 757-758, 2015.

[286] A. Arbab-Zadeh and V. Fuster, "The Myth of the "Vulnerable Plaque": Transitioning From a Focus on Individual Lesions to Atherosclerotic Disease Burden for Coronary Artery Disease Risk Assessment," *J Am Coll Cardiol,* vol. 65, pp. 846-855, 2015.

[287] P. Libby and G. Pasterkamp, "Requiem for the 'vulnerable plaque'," *European Heart Journal,* vol. 36, pp. 2984-7, 2015.

[288] G. S. Mintz, "Predicting the Vulnerable Patient Using Intravascular Imaging," *J Am Coll Cardiol,* vol. 69, pp. 2514-2516, 2017.

[289] E. S. Brilakis, S. T. Sum, S. P. Madden, and J. E. Muller, "Intravascular Imaging of Lipid Core Plaque by NearInfrared Spectroscopy," in *Intravascular Imaging: Current Applications and Research Developments: Current Applications and Research Developments*, V. D. Tsakanikas, Ed., ed: IGI Global, 2011, pp. 240-259.

[290] W. M. Suh, A. H. Seto, R. J. Margey, I. Cruz-Gonzalez, and I. K. Jang, "Intravascular detection of the vulnerable plaque," *Circ Cardiovasc Imaging,* vol. 4, pp. 169-78, 2011.

[291] N. Gonzalo, P. W. Serruys, P. Barlis, J. Ligthart, H. M. Garcia-Garcia, and E. Regar, "Multi-modality intra-coronary plaque characterization: a pilot study," *International Journal of Cardiology,* vol. 138, pp. 32-9, 2010.

[292] J. L. Su, S. J. Grainger, C. A. Greiner, S. P. Madden, S. T. Sum, J. E. Muller, and R. D. Madder, "Detection and structural characterization of lipid-core plaques with intravascular NIRS-IVUS imaging," *Interventional Cardiology,* vol. 7, 2015.

[293] L. Lee, M. Alloosh, R. Saxena, W. Van Alstine, B. A. Watkins, J. E. Klaunig, M. Sturek, and N. Chalasani, "Nutritional model of steatohepatitis and metabolic syndrome in the Ossabaw miniature swine," *Hepatology,* vol. 50, pp. 56-67, 2009.

[294] Z. P. Neeb, J. M. Edwards, M. Alloosh, X. Long, E. A. Mokelke, and M. Sturek, "Metabolic syndrome and coronary artery disease in Ossabaw compared with Yucatan swine," *Comp Med,* vol. 60, pp. 300-15, 2010.

[295] R. P. Kreutz, M. Alloosh, K. Mansour, Z. Neeb, Y. Kreutz, D. A. Flockhart, and M. Sturek, "Morbid obesity and metabolic syndrome in Ossabaw miniature swine are associated with increased platelet reactivity," *Diabetes Metab Syndr Obes,* vol. 4, pp. 99-105, 2011.

[296] M. C. Dyson, M. Alloosh, J. P. Vuchetich, E. A. Mokelke, and M. Sturek, "Components of metabolic syndrome and coronary artery disease in female Ossabaw swine fed excess atherogenic diet," *Comp Med,* vol. 56, pp. 35-45, 2006.

[297] J. Hui, Q. Yu, T. Ma, P. Wang, Y. Cao, R. S. Bruning, Y. Qu, Z. Chen, Q. Zhou, M. Sturek, J.-X. Cheng, and W. Chen, "High-speed intravascular photoacoustic imaging at 1.7 um with a KTP-based OPO," *Biomed Opt Express,* vol. 6, pp. 4557-4566, 2015.

[298] *American National Standard for Safe Use of Lasers* vol. ANSI Z136.1: Laser Institute of America, 2014.

[299] N. R. Council, *Guide for the Care and Use of Laboratory Animals: Eighth Edition*. Washington, DC: National Academies Press, 2011.

[300] P. R. Moreno, "Intimomedial Interface Damage and Adventitial Inflammation Is Increased Beneath Disrupted Atherosclerosis in the Aorta: Implications for Plaque Vulnerability," *Circulation,* vol. 105, pp. 2504-2511, 2002.

[301] S. Watkins, "Cryosectioning," in *Current Protocols in Molecular Biology*, ed: John Wiley & Sons, Inc., 2001.

[302] J. L. Dixon, J. D. Stoops, J. L. Parker, M. H. Laughlin, G. A. Weisman, and M. Sturek, "Dyslipidemia and vascular dysfunction in diabetic pigs fed an atherogenic diet," *Arterioscler Thromb Vasc Biol,* vol. 19, pp. 2981-92, 1999.

[303] J. J. Chiu and S. Chien, "Effects of disturbed flow on vascular endothelium: pathophysiological basis and clinical perspectives," *Physiol Rev,* vol. 91, pp. 327-87, 2011.

[304] C. K. Zarins, D. P. Giddens, B. K. Bharadvaj, V. S. Sottiurai, R. F. Mabon, and S. Glagov, "Carotid bifurcation atherosclerosis. Quantitative correlation of plaque localization with flow velocity profiles and wall shear stress," *Circ Res,* vol. 53, pp. 502-14, 1983.

[305] D. N. Ku, D. P. Giddens, C. K. Zarins, and S. Glagov, "Pulsatile flow and atherosclerosis in the human carotid bifurcation. Positive correlation between plaque location and low oscillating shear stress," *Arteriosclerosis,* vol. 5, pp. 293-302, 1985.

[306] M. Shah and M. B. Sikkel, "Coronary artery disease and age: beyond atherosclerosis," *J Physiol,* vol. 591, pp. 5807-8, 2013.

[307] J. E. Muller, G. S. Abela, R. W. Nesto, and G. H. Tofler, "Triggers, acute risk factors and vulnerable plaques: The lexicon of a new frontier," *J Am Coll Cardiol,* vol. 23, pp. 809-813, 1994.

[308] S. S. Kanwar, G. W. Stone, M. Singh, R. Virmani, J. Olin, T. Akasaka, and J. Narula, "Acute coronary syndromes without coronary plaque rupture," *Nat Rev Cardiol,* vol. advance online publication, 2016.

[309] M. J. Chapman, S. Blankenberg, and U. Landmesser, "The year in cardiology 2015: prevention," *European Heart Journal,* vol. 37, pp. 510-9, 2016.

[310] Y. T. Lee, V. Laxton, H. Y. Lin, Y. W. F. Chan, S. Fitzgerald-Smith, T. L. O. To, B. P. Yan, T. Liu, and G. Tse, "Animal models of atherosclerosis," *Biomed Rep,* vol. 6, pp. 259-266, 2017.

[311] B. Emini Veseli, P. Perrotta, G. R. A. De Meyer, L. Roth, C. Van der Donckt, W. Martinet, and G. R. Y. De Meyer, "Animal models of atherosclerosis," *Eur J Pharmacol,* vol. 816, pp. 3-13, 2017.

[312] J. Shim, R. H. Al-Mashhadi, C. B. Sorensen, and J. F. Bentzon, "Large animal models of atherosclerosis--new tools for persistent problems in cardiovascular medicine," *J Pathol,* vol. 238, pp. 257-66, 2016.

[313] J. F. Bentzon and E. Falk, "Atherosclerotic lesions in mouse and man: is it the same disease?," *Curr Opin Lipidol,* vol. 21, pp. 434-40, 2010.

[314] J. L. Fleg, G. W. Stone, Z. A. Fayad, J. F. Granada, T. S. Hatsukami, F. D. Kolodgie, J. Ohayon, R. Pettigrew, M. S. Sabatine, G. J. Tearney, S. Waxman, M. J. Domanski, P. R. Srinivas, and J. Narula, "Detection of high-risk atherosclerotic plaque: report of the NHLBI Working Group on current status and future directions," *JACC Cardiovasc Imaging,* vol. 5, pp. 941-55, 2012.

[315] J. F. Granada, G. L. Kaluza, R. L. Wilensky, B. C. Biedermann, R. S. Schwartz, and E. Falk, "Porcine models of coronary atherosclerosis and vulnerable plaque for imaging and interventional research," *EuroIntervention,* vol. 5, pp. 140-8, 2009.

[316] Y. Cao, A. Kole, J. Hui, Y. Zhang, J. Mai, M. Alloosh, M. Sturek, and J.-X. Cheng, "Fast assessment of lipid content in arteries in vivo by intravascular photoacoustic tomography," *Sci Rep,* vol. 8, p. 2400, 2018.

[317] H. Tamaru, K. Fujii, M. Fukunaga, T. Imanaka, K. Miki, T. Horimatsu, M. Nishimura, T. Saita, A. Sumiyoshi, M. Shibuya, Y. Naito, and T. Masuyama, "Impact of spotty calcification on long-term prediction of future revascularization: a prospective three-vessel intravascular ultrasound study," *Heart Vessels,* vol. 31, pp. 881-9, 2016.

[318] Y. Kataoka, K. Wolski, K. Uno, R. Puri, E. M. Tuzcu, S. E. Nissen, and S. J. Nicholls, "Spotty calcification as a marker of accelerated progression of coronary atherosclerosis: insights from serial intravascular ultrasound," *J Am Coll Cardiol,* vol. 59, pp. 1592-7, 2012.

[319] S. Ehara, Y. Kobayashi, M. Yoshiyama, K. Shimada, Y. Shimada, D. Fukuda, Y. Nakamura, H. Yamashita, H. Yamagishi, K. Takeuchi, T. Naruko, K. Haze, A. E. Becker, J. Yoshikawa, and M. Ueda, "Spotty calcification typifies the culprit plaque in patients with acute myocardial infarction: an intravascular ultrasound study," *Circulation,* vol. 110, pp. 3424-9, 2004.

[320] R. Puri, S. J. Nicholls, M. Shao, Y. Kataoka, K. Uno, S. R. Kapadia, E. M. Tuzcu, and S. E. Nissen, "Impact of Statins on Serial Coronary Calcification During Atheroma Progression and Regression," *J Am Coll Cardiol,* vol. 65, pp. 1273-82, 2015.

[321] S. E. Nissen and P. Yock, "Intravascular Ultrasound," *Circulation,* vol. 103, pp. 604-616, 2001.

[322] Y. Vengrenyuk, S. Carlier, S. Xanthos, L. Cardoso, P. Ganatos, R. Virmani, S. Einav, L. Gilchrist, and S. Weinbaum, "A hypothesis for vulnerable plaque rupture due to stress-induced debonding around cellular microcalcifications in thin fibrous caps," *Proc Natl Acad Sci U S A,* vol. 103, pp. 14678-83, 2006.

[323] F. D. Kolodgie, J. Narula, A. P. Burke, N. Haider, A. Farb, Y. Hui-Liang, J. Smialek, and R. Virmani, "Localization of apoptotic macrophages at the site of plaque rupture in sudden coronary death," *Am J Pathol,* vol. 157, pp. 1259-68, 2000.

[324] F. D. Kolodgie, H. K. Gold, A. P. Burke, D. R. Fowler, H. S. Kruth, D. K. Weber, A. Farb, L. J. Guerrero, M. Hayase, R. Kutys, J. Narula, A. V. Finn, and R. Virmani, "Intraplaque hemorrhage and progression of coronary atheroma," *N Engl J Med,* vol. 349, pp. 2316-25, 2003.

[325] R. Virmani, F. D. Kolodgie, A. P. Burke, A. V. Finn, H. K. Gold, T. N. Tulenko, S. P. Wrenn, and J. Narula, "Atherosclerotic plaque progression and vulnerability to rupture: angiogenesis as a source of intraplaque hemorrhage," *Arterioscler Thromb Vasc Biol,* vol. 25, pp. 2054-61, 2005.

[326] R. J. Siegel, K. Swan, G. Edwalds, and M. C. Fishbein, "Limitations of postmortem assessment of human coronary artery size and luminal narrowing: differential effects of tissue fixation and processing on vessels with different degrees of atherosclerosis," *J Am Coll Cardiol,* vol. 5, pp. 342-6, 1985.

[327] G. S. Mintz and G. Guagliumi, "Intravascular imaging in coronary artery disease," *The Lancet,* vol. 390, pp. 793-809, 2017.

[328] M. L. McKenney-Drake, S. D. Rodenbeck, M. K. Owen, K. A. Schultz, M. Alloosh, J. D. Tune, and M. Sturek, "Biphasic alterations in coronary smooth muscle Ca(2+) regulation in a repeat cross-sectional study of coronary artery disease severity in metabolic syndrome," *Atherosclerosis,* vol. 249, pp. 1-9, 2016.

[329] M. L. McKenney-Drake, S. D. Rodenbeck, R. S. Bruning, A. Kole, K. W. Yancey, M. Alloosh, H. S. Sacks, and M. Sturek, "Epicardial Adipose Tissue Removal Potentiates Outward Remodeling and Arrests Coronary Atherogenesis," *Ann Thorac Surg,* vol. 103, pp. 1622-1630, 2017.

[330] M. L. McKenney, K. A. Schultz, J. H. Boyd, J. P. Byrd, M. Alloosh, S. D. Teague, A. A. Arce-Esquivel, J. N. Fain, M. H. Laughlin, H. S. Sacks, and M. Sturek, "Epicardial adipose excision slows the progression of porcine coronary atherosclerosis," *J Cardiothorac Surg,* vol. 9, p. 2, 2014.

[331] A. F. Hedayat, K. H. Park, T. G. Kwon, J. R. Woollard, K. Jiang, D. F. Carlson, A. Lerman, and L. O. Lerman, "Peripheral vascular atherosclerosis in a novel PCSK9 gain-of-function mutant Ossabaw miniature pig model," *Transl Res,* 2017.

[332] G. W. Stone, A. Maehara, and G. S. Mintz, "The Reality of Vulnerable Plaque Detection," *JACC Cardiovasc Imaging,* vol. 4, pp. 902-904, 2011.

[333] E. J. Benjamin, S. S. Virani, C. W. Callaway, A. R. Chang, S. Cheng, S. E. Chiuve, M. Cushman, F. N. Delling, R. Deo, S. D. de Ferranti, J. F. Ferguson, M. Fornage, C. Gillespie, C. R. Isasi, M. C. Jiménez, L. C. Jordan, S. E. Judd, D. Lackland, J. H. Lichtman, L. Lisabeth, S. Liu, C. T. Longenecker, P. L. Lutsey, D. B. Matchar, K. Matsushita, M. E. Mussolino, K. Nasir, M. O'Flaherty, L. P. Palaniappan, D. K. Pandey, M. J. Reeves, M. D. Ritchey, C. J. Rodriguez, G. A. Roth, W. D. Rosamond, U. K. A. Sampson, G. M. Satou, S. H. Shah, N. L. Spartano, D. L. Tirschwell, C. W. Tsao, J. H. Voeks, J. Z. Willey, J. T. Wilkins, J. H. Wu, H. M. Alger, S. S. Wong, and P. Muntner, "Heart Disease and Stroke Statistics—2018 Update: A Report From the American Heart Association," *Circulation,* 2018.

VITA

Ayeeshik Kole was born in New Brunswick, NJ and grew up in Columbia, MD. In 2012, he graduated from Vanderbilt University with a Bachelor of Engineering in Biomedical Engineering with Honors and second major in Communication of Science and Technology. At Vanderbilt, he was the recipient of the Paul Harrawood Honors Undergraduate Engineering Scholarship. During his undergraduate studies, he worked under the supervision of Dr. John P. Wikswo at the Vanderbilt Institute of Integrative Biosystems Research and Education where he researched the integration of microfluidic nanophysiometers with high-resolution mass spectrometry for complex systems biology measurements. After undergraduate training, he matriculated directly into the Medical Scientist Training Program at Indiana University School of Medicine, where he completed the first two years of the medical curriculum from 2012 to 2014. From 2014 to 2018, Ayeeshik pursued his doctorate degree at the Purdue University Weldon School of Biomedical Engineering under the direction of Dr. Michael Sturek and Dr. Ji-Xin Cheng. During this time, he was awarded the IUPUI Graduate Student Imaging Research Fellowship and Hugh W. and Edna M. Donnan Fellowship. His research has been highly collaborative effort that has resulted in numerous oral and poster presentations, publications, and awards. Outside of research, Ayeeshik has served in several leadership roles including co-president of the Combined Degree Student Council, vice presidents of the Technology in Medicine Student Interest Group and Medical Missions Student Interest Group, and education and research chair of the Interventional Radiology Student Interest Group. After completing his Ph.D., he will return to Indiana University School of Medicine to complete his medical degree.

PUBLICATIONS

1. **A. Kole***, Y. Cao*, J. Hui, I. A. Bolad, M. Alloosh, J.-X. Cheng, and M. Sturek, "Comparative quantification of lipid core plaques by intravascular photoacoustic imaging and near-infrared spectroscopy," (Under review).

2. J. Badin*, **A. Kole***, B. Stivers, V. Progar, A. Pareddy, M. Alloosh, and M. Sturek, "Alloxan-induced Diabetes exacerbates coronary atherosclerosis and calcification in Ossabaw miniature swine with metabolic syndrome," *J Trans Med* (In revision).

3. Y. Cao, **A. Kole**, J. Hui, Y. Zhang, J. Mai, M. Alloosh, M. Sturek, and J.-X. Cheng, "Fast assessment of lipid content in vivo by intravascular photoacoustic tomography," *Sci Rep*, vol. 8, p. 2400, 2018.

4. J. Hui*, Y. Cao*, Y. Zhang*, **A. Kole***, P. Wang, G. Yu, G. Eakins, M. Sturek, W. Chen, and J.-X. Cheng, "Real-time intravascular photoacoustic-ultrasound imaging of lipid-laden plaque in human coronary artery at 16 frames per second," *Sci Rep*, vol. 7, p. 1417, 2017.

5. M. L. McKenney-Drake, S. D. Rodenbeck, R. S. Bruning, **A. Kole**, K. W. Yancey, M. Alloosh, H.S. Sacks, and M. Sturek, "Epicardial Adipose Tissue Removal Potentiates Outward Remodeling and Arrests Coronary Atherogenesis," *Ann Thorac Surg*, vol. 103, pp. 1622-1630, 2017.

6. Y. Cao, **A. Kole**, L. Lan, P. Wang, J. Hui, M. Sturek, and J.-X. Cheng, "Spectral analysis assisted photoacoustic imaging for lipid composition differentiation," *Photoacoustics*, vol. 7, pp. 12-19, 2017.

7. Y. Cao, J. Hui, **A. Kole**, P. Wang, Q. Yu, W. Chen, M. Sturek, and J.-X. Cheng, "High-sensitivity intravascular photoacoustic imaging of lipid–laden plaque with a collinear catheter design," S*ci Rep*, vol. 6, p. 25236, 2016.

*Equal contributing author.